



Norwegian University
of Life Sciences

Master's Thesis 2022 30 ECTS
Faculty of Science and Technology

Evaluating the friction velocity of flat-roofed buildings in relation to snow erosion using numerical simulations

Hakan Ole Ensrud Abediy
Structural Engineering and Architecture

Acknowledgements

This thesis marks the end of my three years as a student at NMBU.

I want to thank my supervisor, Thomas K. Thiis, for his continuous guidance and feedback during the work of this master thesis. His passion and extensive knowledge of different fields were inspiring. I would also like to thank Iver Frimannslund for helping me with my CFD questions.

Finally, I would like to thank my friends in computer lab TF1-105 for the exciting discussions.

Ås,
May,
= 2022
Hakan
Abe-
diy

Summary

Snow loads are often the most significant loads for large flat roof buildings in the Nordics. The relevant building code for snow loads for this area, EN-1991-1-3, conservatively oversimplifies the effect of wind on snow loads. Additionally, EN-1991-1-3 does not contain a direct method to calculate the design snow load for flat buildings exceeding 50 meters. The oversimplifications are intended to make engineers' snow load calculations easy to perform. They also result in increased construction costs due to their conservative approach.

This study examines the friction velocities u_* on the roof using 3D single-phase CFD simulations completed in ANSYS CFX. Outliers are labeled by use of the Modified Z-method and then removed. Then the roofs' median friction velocity is calculated based on the filtered dataset. Further analysis of the friction velocities is performed in Python.

This thesis examines two instances. In both cases, a power-law wind profile with $\alpha = 0.18$ and $\alpha = 0.28$, and the wind directions simulated are $\theta = 0^\circ, 22.5^\circ, 45^\circ$. Case 1 is a 50x50 m square roof without a parapet and heights of 10,20 and 30 m. Case 2 is a square 50x50 m roof with a parapet at 10,20, and 30 m height. The parapet extends to a height of 0.5 meters and a width of 0.2 meters. Between the two cases, the difference in median friction velocities was negligible. The median friction velocity increases with height and varies significantly depending on the direction of the wind. The expressions for normalized friction velocity were calculated based on the CFD simulations.

The expressions obtained for the normalized friction velocity can be implemented in a future snow model to predict the roof's design snow load more accurately.

Table of Contents

Acknowledgements	i
Summary	iii
Table of Contents	v
List of Figures	x
List of Tables	xi
1 Introduction	1
1.1 Opening	1
1.2 Research problem	1
1.3 Research significance	2
1.4 Limitations	2
1.5 Structural outline	2
2 State of the art	5
3 Theory	7
3.1 Snow loads as described in EN-1991-1-3	7
3.1.1 Exposure coefficient, C_e	9
3.2 Snow transport	10
3.2.1 Aerodynamic shade	11
3.3 Mass transport rate	12
3.4 Air	13
3.5 Wind	13
3.6 Atmospheric boundary layer	14
3.7 Power law wind profile	15
3.8 Friction velocity	16
3.9 Threshold friction velocity	17
3.10 Roughness length	18
3.11 Fluid Mechanics Introduction	19
3.12 Boundary layer	21
3.12.1 Turbulent boundary layer	21

3.13	Flow around a building	22
3.14	CFD	24
3.14.1	Single and mutiphase simulations	24
3.14.2	Steady state and transient simulations	25
3.14.3	Turbulence modelling	25
	RANS	26
	LES	27
	DNS	27
3.14.4	ANSYS CFX	27
	Inflation layers	28
	Face sizing	28
3.14.5	Convergence	28
3.14.6	Boundary conditions	29
	Inlet	29
	Outlet	29
	Walls	29
	Symmetry	30
3.14.7	Mesh	30
	Mesh quality	31
3.14.8	Wall functions	32
3.14.9	Y^+	34
3.14.10	Similarity solutions	34
3.14.11	Errors sources in CFD simulations	35
	Numerical errors	35
	Modelling errors	36
	User errors	36
	Application uncertainty	36
	Software errors	36
	Outliers	37
4	Methods	39
4.1	Grid independence study	39
4.2	3D simulations	41
4.2.1	Building geometries	41
4.2.2	Wind model	42
4.2.3	Boundary conditions	43
4.2.4	Flat roof simulations without a parapet	45
4.2.5	Flat roof simulations with a parapet	45
4.2.6	Filtering (Modified Z-method)	47

4.2.7	Scaling parameters	48
5	Results	49
5.1	2D Grid independency study	49
5.1.1	Mesh details	49
5.2	3D simulations	49
5.2.1	Simulations with terrain roughness $\alpha = 0.18$	53
5.2.2	Simulations with terrain roughness $\alpha = 0.28$	55
5.2.3	3D simulation verification	59
5.2.4	Outliers	64
6	Discussion	65
6.1	Mesh	65
6.1.1	Grid independence study	65
6.1.2	Convergence in 3D simulations	68
6.2	Friction velocity	69
6.2.1	Friction velocity Streamlines	69
6.2.2	Friction velocity Contour plots	70
6.2.3	Snow erosion	72
6.2.4	Effect of parameter selection	72
6.3	Consequences of simplifications	74
6.4	Validity of the master thesis	75
6.5	Modified Z-method	77
6.6	Limitations	77
7	Conclusions	79
	References	81
	Appendix A	85

List of Figures

2.1	Photo of Irwin probes distributed in the three central lines ferreira2019	6
3.1	Table 5.2: Snow load shape coefficient (<i>NS-EN 1991-1-3. Eurocode 1: Actions on structures - Part 1-3: General actions - Snow loads</i> 2018)	8
3.2	Snow load shape coefficients for obstructions(<i>NS-EN 1991-1-3. Eurocode 1: Actions on structures - Part 1-3: General actions - Snow loads</i> 2018)	9
3.3	Exposure coefficient values different topography from table NA.5.1 in <i>NS-EN 1991-1-3. Eurocode 1: Actions on structures - Part 1-3: General actions - Snow loads</i> (2018)	10
3.4	The linear relationship between friction velocity and mean saltation length on semi-hard snow (Sato et al., 2004)	13
3.5	Wind profiles in a stable, neutral and unstable atmosphere, y-axis is logarithmic (Kaimal and Finnigan, 1994)	15
3.6	A plot of the difference between the power and logarithmic wind profiles between 0-100 meters over the surface Holmes (2015, p. 61)	16
3.7	u_* distribution on a flat roof obtained using both 2D CFD simulations and wind tunnel experiments (Qiang et al., 2021)	17
3.8	Force diagram for forces acting on snow particles with a single cohesive bond (Schmidt, 1980, p. 457)	18
3.9	The different terrain categories and parameters used in <i>NS-EN 1991-1-4. Eurocode 1: Actions on structures - Part 1-4: General actions - Wind actions</i> (2009)	19
3.10	Flow pattern around building from wind direction 0° (Oke et al., 2017)	23
3.11	Flow pattern around building from wind direction 45° (Oke et al., 2017)	23
3.12	Sand equivalent grain roughness K_s is used to model rough walls (Hetsroni et al., 2011)	30
3.13	Vectors used to calculate orthogonality for a cell surrounded by neighbouring cells <i>Ansys Meshing User's Guide</i> (2021, p. 142)	32
3.14	Law of the wall Tennekes and Lumley (1972, p. 160)	33
4.1	Building geometries for the 3D simulations	41

4.2	Domain size used in the CFD simulations. Origin is in the middle of the building in the XY-plane. Drawings are not to scale. Domain is sized accordingly to Tominaga et al. (2011).	44
5.1	Grid independence study	50
5.2	The chosen mesh's (Blue plot) mesh dependency	50
5.3	Section plane view of the mesh close to the roof in the XZ-plane. The face sizing is shown on the (blue) building.	51
5.4	Skewness quality of each cell close to the roof. The larger cells in the background are face sizing cells.	51
5.5	Orthogonal quality of each cell close to the roof. The larger cells in the background are face sizing cells.	52
5.6	Close view of aspect ratio in each cell close to the roof. The larger cells in the background are face sizing cells.	52
5.7	u_* as a function of roof height H where $\alpha = 0.18$. "P" - Parapet, and "NP" - No parapet. Some values lie behind other values and show as one. Fitted with the line in Table 5.1	54
5.8	u_* normalized by the roof wind velocity U_H at each roof height where $\alpha = 0.18$. "P" - Parapet, and "NP" - No parapet. Some values lie behind other values and show as one. Fitted with the line in Table 5.1	54
5.9	u_* as a function of roof height H where $\alpha = 0.28$. "P" - Parapet, and "NP" - No parapet. Some values lie behind other values and show as one.	55
5.10	u_* normalized by the roof wind velocity U_H at each roof height where $\alpha = 0.28$. "P" - Parapet, and "NP" - No parapet. Some values lie behind other values and show as one.	56
5.11	Value range for the contours plot	56
5.12	Difference in U_*/U_H between 1:100 and full scale simulation for the 10 meter high building without a parapet. NP: 45° 1:1 lies behind NP: 22° 1:100 NP: 45°	60
5.13	Reynolds dependency verification of U_*/U_H for different wind directions for the 10 meter high building without a parapet	61
5.14	U_*/U_H dependency on K_s	62
5.15	U_*/U_H dependency on inlet turbulence intensity	63
A.1	$\frac{u_*}{u_{10} \times \log(H)}$ versus α without a parapet for different building height and wind directions.	85

List of Tables

3.1	34
4.1	The meshes involved in the grid independence study. " y^+ " denotes the range of y^+ values measured on a straight line in the middle of the roof in the wind direction direction.	40
4.2	Study of the chosen mesh's (case 1) domain size dependency. The domain size is given in the building height H. x_D denotes domain dimension x. . .	41
4.3	3D CFD simulation properties	45
4.4	All simulation cases for flat roofs, $\alpha = 0.18$ without a parapet with different building heights and wind directions. "NP" - No parapet	46
4.5	All simulation cases for flat roofs, $\alpha = 0.28$ without a parapet with different building heights and wind directions. "NP" - No parapet	46
4.6	All simulation cases for flat roofs with parapet, $\alpha = 0.18$ with a parapet with different building heights and wind directions. "P" - parapet.	46
4.7	All simulation cases for flat roofs with parapet, $\alpha = 0.28$ with a parapet with different building heights and wind directions."P" - parapet.	47
5.1	Least squares linear fit of the different simulation cases for $\alpha = 0.18$ and 0.28 as a function of H. The cases with or without parapet are bundled together.	53
5.2	Fitted filtered median u_*/U_H values for the three wind directions studied displayed as dashed lines in Figures 5.8 and 5.10.	53
5.3	Surface streamlines on the roofs for $\theta = 0^\circ$ and $\alpha = 0.28$. Wind moves from left to right on each plot. No parapet("NP") cases on the left column and parapet("P") cases on the right column.	57
5.4	Contour plots of friction velocities on the roofs for $\alpha = 0.28$. Wind moves from left to right on each plot. No parapet("NP") cases on the left column and parapet("P") cases on the right column. The values are scaled according to Figure 5.11.	58

1. Introduction

1.1 Opening

Snow loads are often the most significant variable load used when designing buildings in Nordic areas. The method of calculating snow loads in the current European snow load standard EN-1991-1-3:2018 is based on simple models. Its goal is to provide a convenient approximative calculation method containing the same physical principles as the complex real-life situation. This results in conservative design snow loads, which increases the total building project cost. This chapter will begin by discussing the background and context of the master's thesis, followed by the research problem, question, the significance, and limitations of this thesis.

The wind has a highly erratic and dynamic behavior which makes it difficult to quantify. In EN-1991-1-3, the exposure coefficient is a single value based on simple meteorological data. Areas of a roof prone to snow erosion can be quantified by analyzing the shear stresses from the wind which act on the snowbed (or any granular material). These shear stresses can be expressed as friction velocities. If the friction velocity exceeds a snow-type dependent threshold value, snow erosion will occur. Otherwise, if the friction velocity does not exceed the threshold value, then accumulation will occur. The friction velocity can then potentially calculate the transport rate of snow eroded from the roof.

This master thesis will use 3D single-phase RANS CFD simulations to analyze friction velocities on flat roofs with or without a parapet with wind from different directions.

1.2 Research problem

The research goal is to quantify the normalized friction velocity of a flat roof with and without a parapet from different wind directions by using RANS CFD simulations.

1.3 Research significance

The friction velocity equations obtained can in future work be used to quantify the potential snow erosion of different flat roofs at various heights, which can then be incorporated into an improved snow model to provide more accurate snow load predictions than the current model while still streamlining the calculation process for the engineers.

1.4 Limitations

Any solution to a complex and erratic problem like airflow has many limitations. The CFD simulations contain the following limitations:

The flow is assumed isothermal (constant temperature), and any heat transfer is outside the scope of this thesis.

No snow has been modeled. Single-phase simulations neglect any energy transfer between the wind and snow.

The computational power available and the number of simulations completed have limited the mesh resolution.

All terrains are assumed to be infinitely flat planes with different terrain roughness.

The atmosphere is assumed neutrally stratified.

The buildings are assumed to be isolated from interfering infrastructure.

The effect of different parapet dimensions on the solution was not checked. Only straight edge parapets were studied, not the effect of other edge shapes.

The incidence angles of the wind are not considered in this thesis.

Wind independently blows from one wind direction at a time.

1.5 Structural outline

The outline is presented to give the readers a better understanding of the structure and how the chapters relate.

Chapter 2 gives an overview of the current research relating to snow erosion.

Chapter 3 will explain the necessary key concepts of the master thesis. Furthermore, it will be used to explain the results gathered.

Chapter 4 will explain how and on what basis the 3D CFD simulations were completed. A 2D grid independency study was first completed to analyze the accuracy of the mesh.

Chapter 5 will show the results of the 3D simulations and the grid independency study and display any verifications investigated.

Chapter 6 will discuss the findings, verification of the solutions, and limitations.

Chapter 7 will summarize the findings and mention areas for future work.

2. State of the art

An extensive range of previous similar studies has been conducted. The goal of this chapter will be to show how this master thesis contributes something new to the topic by examining what has been previously studied.

Snow drifting is historically studied through field observations, wind tunnel experiments, and, more recently, CFD simulations. CFD simulations are cheap to perform, have many sample points, and can simulate full-scale geometries. However, their accuracy depends on the CFD user, computational cost available, and turbulence model used. Wind tunnel experiments are expensive to perform, highly accepted, and have high turbulence resolution, but they use few sample points and often use downscaling of the geometry. Field experiments use real-life conditions in contrast to the previous study methods, but it is not as easy to control the parameters. The downscaling might bring problems with achieving complete similarity. In terms of CFD simulations, the majority of research has focused on snow drifting around buildings (Uematsu et al., 1991) Tominaga et al. (2011). A significant subset of these CFD simulations focused exclusively on snow drifting on roofs. Zhou et al. (2018) conducted a single-phase LES simulation to study friction velocity on a flat roof. However, most of these studies used two-phase RANS simulations in two dimensions. A two-phase simulation simulates both the air and the snow concurrently. Zhou et al. (2016) performed a two-phase quasi-steady CFD simulation to simulate snow distribution on the roof and used friction velocity to calculate the transport rate. Only one wind direction can be simulated when a two-dimensional simulation is used. Additionally, a small number of studies have been conducted on 3D CFD simulations of wind from various directions on flat roofs. However, in reality, the direction of the wind is constantly changing. A variety of roof shapes have been studied, including flat, gable, and stepped roofs. Owen (1964) and Kind (1976) modeled snow drift loads on roofs and developed a snow drift rate equation that is dependent on friction velocity and snow properties. O'Rourke et al. (2005) incorporated a reduction factor of the drift rate depending on the roof's span.

The following studies are the most relevant points to this master thesis; Tabler (1994) observed that the friction velocity on the ground is $u_*/U_{10} = 0.04$, where U_{10} is the

mean wind speed at the height of 10 meters. This is the height at which most weather stations perform wind measurements. A relationship between the mean wind speed and friction velocity is needed to easily calculate the snow drift rate based on the friction velocity u_* . Qiang et al. (2019) conducted cryogenic wind tunnel tests on a 1:25 scale model of a building and determined that $u_*/V_H = 0.06$, where V_H is the mean wind speed at the roof height. Following that, Qiang et al., 2021 conducted two-dimensional CFD simulations of flat roofs with $L = 2H$, $L = 8H$, and $L = 18H$. He concluded that the friction velocity on the roof was uniform except near the edges based on these simulations. Furthermore, u_*/V_H between 0.048 and 0.055. This study used a power-law wind profile with $\alpha = 0.12$, corresponding to Chinese terrain category A. Sea terrain with a roughness height of $z_0 = 0.01$ m is classified as terrain category A (Ge and Jin, 2004). Ferreira et al. (2019) measured the skin-friction coefficient C_f of a 1:25 scale building by wind tunnel experiments, and conducted RANS simulations. The measurements of the shear stress were conducted by the Irwin probes shown in Figure 2.1. Irwin probes are an example of fewer data points available in a wind tunnel, which gives high discrepancies at the roof's edges compared to the CFD simulations. However, no studies have quantified the normalized friction velocity on different height flat roofs with or without parapets from different wind directions.

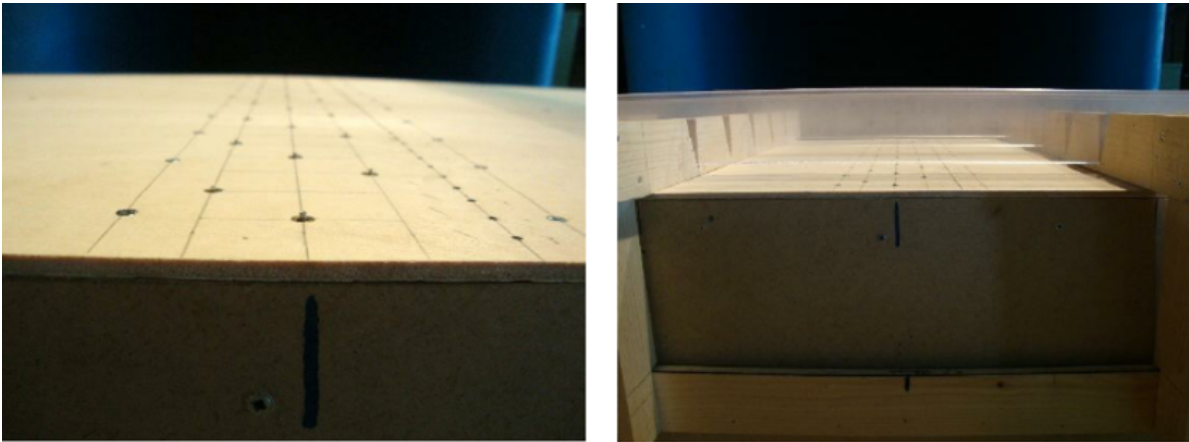


Figure 2.1: Photo of Irwin probes distributed in the three central lines ferreira2019

3. Theory

To facilitate comprehension of the research presented in this master's thesis, a few pertinent key topics will be discussed. The following chapter discusses snow loads, snow transport, wind modeling, theoretical fluid mechanics, and Computational Fluid Dynamics (CFD). The theory presented here will serve as a basis for understanding the simulations and analysis performed in this thesis.

3.1 Snow loads as described in EN-1991-1-3

The Eurocodes are ten European standards describing how structural design should be conducted inside the EU. EN-1991: Actions on structures is one of these standards where EN-1991-1-3 specifically describes snow loads. As described in (Gulvanessian et al., 2002), different climatic situations produce distinct snow conditions. The conditions are non-exceptional falls and drifts and exceptional falls and drifts, giving four conditions combinations. In the Norwegian Annex NA.2, "In Norway, snow loads are not treated either as exceptional or as accident loads"(*NS-EN 1991-1-3. Eurocode 1: Actions on structures - Part 1-3: General actions - Snow loads 2018*). Both drifted and undrifted snow loads on the roof should be accounted for when calculating the snow load. An undrifted snow load means that the snow is uniformly distributed, only affected by the shape of the roof, and no redistribution of snow has happened. A drifted snow load means that the snow has been redistributed on the roof by the wind.

Section 5 of *NS-EN 1991-1-3. Eurocode 1: Actions on structures - Part 1-3: General actions - Snow loads (2018)* describes that snow can be redistributed on a roof in many patterns. The factors affecting the distribution of this pattern can be roof shape, its thermal properties, the roughness of its surface, the amount of heat generated under the roof, the proximity of nearby buildings, the surrounding terrain, the local meteorological climate, in particular its windiness, temperature variations, and the likelihood of precipitation as in Section 5.1(2) (*NS-EN 1991-1-3. Eurocode 1: Actions on structures - Part 1-3: General actions - Snow loads 2018*).

$$s = \mu_i C_e C_t s_k \quad (3.1)$$

where μ_i is the snow load shape coefficient, C_e (further explained in Chapter 3.1.1) is the exposure coefficient, C_t is the thermal coefficient, and s_k is the characteristic snow load on the ground.

For a flat roof the pitch angle $\alpha = 0^\circ$ and as only the shape coefficient μ_1 is used for monopitch roofs then $\mu_1(0) = 0.8$ from Figure 3.1. Buildings with obstructions like parapets should use $\mu_1(0) > 0.8$ (*NS-EN 1991-1-3. Eurocode 1: Actions on structures - Part 1-3: General actions - Snow loads 2018*). This is because less snow is assumed to be removed by wind from roofs with obstacles.

Angle of pitch of roof α	$0^\circ \leq \alpha \leq 30^\circ$	$30^\circ < \alpha < 60^\circ$	$\alpha \geq 60^\circ$
μ_1	0,8	$0,8(60 - \alpha)/30$	0,0
μ_2	$0,8 + 0,8 \alpha/30$	1,6	--

Figure 3.1: Table 5.2: Snow load shape coefficient (*NS-EN 1991-1-3. Eurocode 1: Actions on structures - Part 1-3: General actions - Snow loads 2018*)

Buildings with obstructions like parapets should use $\mu_1(0) > 0.8$ (*NS-EN 1991-1-3. Eurocode 1: Actions on structures - Part 1-3: General actions - Snow loads 2018*). This is because less snow is assumed to be removed from roofs with obstacles by the wind. Chapter 6.2 describes the drifting of snow due to obstacles like parapets accumulating snow. The shape load coefficients are $\mu_1 = 0.8$ and $\mu_2 = \gamma h / s_k$ where $0.8 < \mu_2 < 2.0$. γ is the snow density, h is the height of the obstacle, and l_s is the length of the snowdrift.

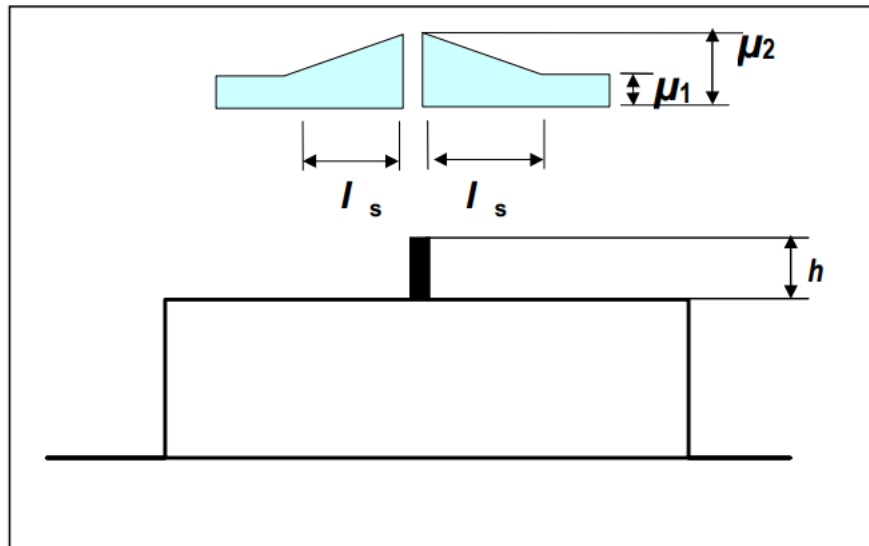


Figure 3.2: Snow load shape coefficients for obstructions (*NS-EN 1991-1-3. Eurocode 1: Actions on structures - Part 1-3: General actions - Snow loads 2018*)

3.1.1 Exposure coefficient, C_e

The exposure coefficient, C_e , is a coefficient that reflects the effect of snow being removed by the wind on a roof in a specific geographical location, regardless of the roof shape. It can also be described as the balanced load on a flat cold roof divided by the snow ground load. (*ISO 4355 Bases for design on structures - determination of snow loads on roofs 2013*)

Values for C_e are described in Table 5.1/NA.5.1 of *NS-EN 1991-1-3. Eurocode 1: Actions on structures - Part 1-3: General actions - Snow loads (2018)*, it is compartmentalized based on the building's topography and degree of wind exposure. The values for C_e in the Norwegian national annex, NS-EN 1991-1-3:2003+NA:2018, are:

Tabell NA.5.1 – Verdier for C_e for forskjellig topografi

Topografi	C_e
Særlig sterkt vindutsatt ^a	0,8 ^d
Normal ^b	1,0
Skjermet ^c	1,2

^a Særlig vindutsatt topografi: flate, frie områder der alle sidene er eksponert, og der terrenget, høye trær eller byggverk ikke gir noen eller liten beskyttelse mot været.

^b Normal topografi: områder der vinden i liten grad fjerner snø fra byggverk pga. terrenget, andre byggverk eller trær.

^c Skjermet topografi: områder der det aktuelle byggverket er betydelig lavere enn terrenget omkring, eller er omgitt av høye trær og/eller høyere byggverk.

^d Ved bruk av denne verdien forutsettes at normaltemperaturen for perioden januar-februar er lavere enn 0 °C samtidig som normalt minst 10 dager i samme periode har minst én forekomst av 10 minutters middelvind over 8 m/s, samt at takets lengste sidekant ikke overskrider 50 meter.

Figure 3.3: Exposure coefficient values different topography from table NA.5.1 in *NS-EN 1991-1-3. Eurocode 1: Actions on structures - Part 1-3: General actions - Snow loads* (2018)

Based on this brief description, engineers must decide which C_e to choose for a specific building location. In Figure 3.3, $C_e = 0.8$ for windswept topography. This value is only applicable for buildings with the longest side edge of fewer than 50 meters, as defined in table NA.5.1. NS-EN-1991:2003 contains a table of the same values, but it does not impose any restrictions on $C_e = 0.8$ concerning building dimensions. Additionally, "Normal" translates as normal, and "skjermet" as sheltered. For instance, $C_e = 0.8$ indicates that 20 % of the snow erodes from the roof.

C_e decreases with decreasing winter temperatures and increasing wind speeds. (Meløysund et al., 2007). Meløysund et al. (2007) studied meteorological data from 389 weather stations and concluded that the values for C_e are simplified and did not represent the effect wind exposure has on roof snow loads in Norway. This is because C_e is based on simple snow models which struggle to account for the large climate variations in Norway.

3.2 Snow transport

Snow movement occurs because the wind exerts shear stress on the snow cover (D. and D., 2004). Tabler (2003, p. 25) defines snow transport as, "Snow transport is the mass of snow transported by the wind over a specified time and width across the wind". The blowing snow particles relevant to snow transport are concentrated within 5 meters height of the snowbed. Furthermore, the three types of snow transport are suspension/turbulent diffusion, saltation, and creep. The mode initiated depends on the grain weight to wind force. Too large snow particles will creep along the surface and create snow waves circa 1 cm up. Medium-sized particles will jump along the surface, and a typical jump is about 25 cm in the longitudinal direction. Fine particles can be lifted several meters and up to 100 meters. Firstly creep must occur before saltation

can take place before suspension occurs. (Tabler, 2003)

At elevations greater than one kilometer, the wind is governed by pressure distributions known as geostrophic winds. These winds are not resulting in snow drifting at low-rise structures. Meanwhile, snow drifting is a phenomenon determined by the characteristics of the wind close to the ground. The surface topography determines the characteristics of the wind close to the ground. D. and D. (2004)

The amount of shear stress exerted by the wind is proportional to the mean wind speed. Shear stress is greatest at the earth's surface and decreases with height until it reaches zero in the geostrophic wind zone above the boundary layer. (D. and D., 2004). Tabler (2003) observes that the mean wind speed at 10m height necessary for settled snow to erode is highly variable. The wind speed at which the snow begins to move depends on the snow characteristics and air density. Fluffy snow starts eroding at 5.5 m/s, snow hardened by sun and wind starts eroding at 23 m/s. Generally, snow will erode when the mean wind speed exceeds 6.7 m/s. The shear stress necessary for snow to start eroding relates to the threshold friction velocity, which is explained further in Chapter 3.9. The amount of snow erosion depends on the mean wind velocity, which depends on terrain, roughness length of the nearby area, and any obstacles on the roof. An example of an obstacle on the roof is a parapet. The possible effect of a parapet on the flow field is explained in Chapter 3.13.

Furthermore, locations with more prolonged cold winters will have more snow erosion as there are more occasions for it to occur. The more extended time snow erosion can occur, the more snow will be removed from the roof.

Snow will be deposited uniformly on the roof if no wind is present during the deposition phase. (Zhou et al., 2016) Also, the amount of snow eroded depends on the area of the roof, is seen in Equation 3.3. The equation reflects the concept that more snow is eroded from a large roof than from a small one.

Saltating snow differs significantly from saltation of other materials in that the snowbed is not a layer of rounded particles but is a cohesive matrix of bonded crystals that are metamorphosed by the impact of saltating particles (Pomeroy and Gray, 1990).

3.2.1 Aerodynamic shade

Snow is typically cleared off a roof more quickly than from the ground due to the roof's exposure to the wind. Less snow load is regarded on most roofs compared to on the ground. This is the case except in areas of aerodynamic shade. (Qiang et al., 2021). Snow is redistributed when snow erodes from an exposed area and accumulates in a sheltered area. The formation of snowdrifts is a result of aerodynamic shading from

obstacles or terrain when the shear stress on snow particles is reduced below a threshold value u_{*t} . (Thiis and Ferreira, 2015)

Potac et al. (2020) studied snow capture walls and calculated the necessary capture wall height necessary to fully contain the windward snowdrift, and avoid a leeward snowdrift forming. The snow capture wall height necessary is proportional to the ground snow load and the upwind fetch, and inverse proportional to the snow density. Snow density is a function of air temperature, wind exposure and time. The topic of aerodynamic shading is briefly explored in *NS-EN 1991-1-3. Eurocode 1: Actions on structures - Part 1-3: General actions - Snow loads* (2018) as explained in Chapter 3.2.1.

3.3 Mass transport rate

The mass transport rate is used to determine the amount of snow that has eroded from the roof. As a result, the roof's design snow load can be calculated more precisely. Calculating the mass transport rate requires quantifying the friction velocity and the snow properties on the roof.

Several drift rate equations have been developed. Owen (1964) and Kind (1976) expressed the median drift rate for a granular material for a two-dimensional equilibrium saltation flow Q as:

$$Q = \left(\frac{\rho \tilde{u}_*^3}{g}\right) \left(0.25 + \frac{w_f}{3\tilde{u}_*^3}\right) \left(1 - \frac{u_{*t}^2}{\tilde{u}_*^2}\right) \quad (3.2)$$

where g is the gravitational acceleration [m/s], \tilde{u}_* is the median friction velocity [m/s], w_f is the terminal falling velocity of the snow particles [m/s], u_{*t} is the threshold friction velocity

According to O'Rourke et al. (2005), by considering the influence of transport distance on the snow drift rate Q the drift rate is reduced by $\sqrt{L/210}$. The reduced drift rate can be expressed by:

$$Q_{red.} = (\sqrt{L/210})Q \quad (3.3)$$

where L is the length of the roof.

Liu et al. (2019) observed that erosion mainly occurs at the rear and both sides of a flat roof. The middle region of the roof does not significantly contribute to snow erosion. The drift rate is positively correlating with mean wind speed and the roof's length.

Sato et al. (2004) formulated that the mean saltation length of the particles is proportional to the friction velocity as seen in Figure 3.4.

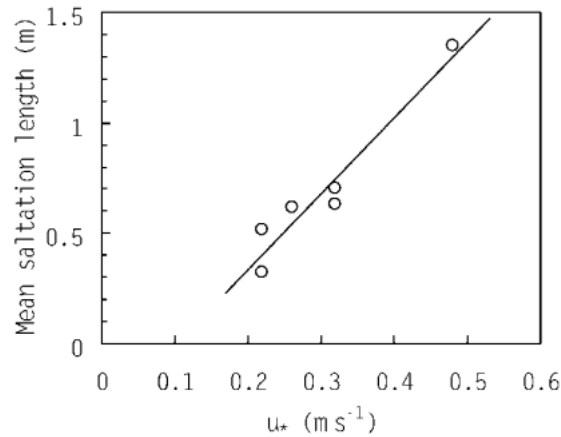


Figure 3.4: The linear relationship between friction velocity and mean saltation length on semi-hard snow (Sato et al., 2004)

3.4 Air

Air is a fluid, and at velocities less than 0.3 Ma, it is considered incompressible (Hibbeler, 2020, p. 31.). Incompressible flow is flows "(...)"which the pressure variations do not produce any significant density variations" (Tritton, 1984). Density is then only a function of temperature, and therefore an isothermal (constant temperature) flow will have constant density. (Tritton, 1984). The bulk modulus is a measure of a fluid's resistance to compression. Because gases have a low density and a low modulus, they are more compressible than liquids. (Hibbeler, 2020)

3.5 Wind

Wind is the movement of air relative to the earth and is primarily caused by pressure differences in the atmosphere caused by the sun's heating of various earth surfaces. Wind is also caused by the earth's rotation, which is referred to as the Coriolis force (Holmes, 2015). However, wind close to the ground, less than 25 meters above the ground, is primarily determined by the surface topography (D. and D., 2004). At weather stations, the wind is typically measured at ten meters above the ground. A wind profile can be used to model this low-altitude wind.

3.6 Atmospheric boundary layer

The wind is erratic, almost random in behavior, and can be complex to model. Changing weather conditions, terrain geometry, surface friction, and earth's rotation complicate wind modeling. The simplest of boundary layers are over an infinite flat surface. Here the wind can be assumed to be horizontally homogenous. "Only ocean surfaces come close to the idealized infinite surface". (Kaimal and Finnigan, 1994). Surfaces that are flat plains with short uniform vegetation are locally horizontally homogenous. A uniform snow layer is an example of this. The wind flow can also be simplified as stationary because the flow properties are not dependent on time, and therefore, the time derivatives disappear. (Kaimal and Finnigan, 1994)

The flux of momentum is given by

$$\tau = K_m \rho \frac{\partial \bar{u}}{\partial z} \quad (3.4)$$

where K_m is the turbulent exchange coefficient for momentum, \bar{u} is the mean streamwise wind component, and ρ is the density. τ is a vector and has the dimensions of stress. The scalar τ_0 , which is the wind stress on the ground, can be written as

$$\tau_0 = \rho u_*^2 \quad (3.5)$$

u_*^2 is the friction velocity. Using u_* wind profiles in neutrally stratified atmospheres can be expressed. (Kaimal and Finnigan, 1994). K_m can be written as:

$$K_m = k u_* z \quad (3.6)$$

By inserting expressions for τ from (3.5) and K_m from (3.6) into (3.4) gives

$$\frac{\partial \bar{u}}{\partial z} = \frac{u_*}{kz}$$

Integrating this gives:

$$\bar{u}(z) = \frac{u_*}{k} \ln\left(\frac{z}{z_0}\right) \quad (3.7)$$

Equation (3.7), the logarithmic wind profile, is used in the Eurocodes. z is the height from the ground. z_0 is roughness length. k is a dimensionless constant called the

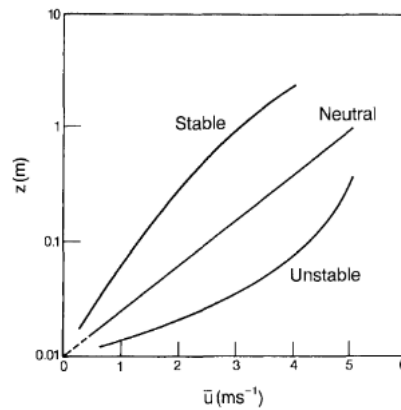


Figure 3.5: Wind profiles in a stable, neutral and unstable atmosphere, y-axis is logarithmic (Kaimal and Finnigan, 1994)

Karman constant, with values ranging from 0.35 to 0.43. "The logarithmic wind profile is strictly valid only for the neutral atmosphere"(Kaimal and Finnigan, 1994). The wind profile will no longer be logarithmic as the atmosphere becomes increasingly more stable. Nevertheless, the wind profile underneath a height of 10 meters can always be regarded as logarithmic. (Kaimal and Finnigan, 1994)

The thickness of the boundary layer and the velocity profile depends on surface roughness D . and D . (2004, p 339)

Lo et al. (2016) studied the effect interfering buildings have on wind forces on a building downstream. He concluded that some building locations experienced an increased skin drag coefficient C_f while C_f was reduced in other locations.

The logarithmic wind profile is the most accurate mathematical expression for strong winds in the atmosphere's first 100-200 meters. The problem with the logarithmic law is that it cannot be evaluated for the logarithm of negative values, and it is more challenging to integrate. Therefore wind engineers often prefer to use the power law. (Holmes, 2015)

3.7 Power law wind profile

A power law profile can also express the time-averaged, neutrally stratified velocity boundary layer over an infinite flat surface. The power law wind profile has no theoretical basis, unlike the logarithmic law, but is easily integrated over height, making it easier to use. The two wind profile laws are the same between 0-20 meters and nearly identical between 20-100 meters over the surface, as seen in figure 3.6. (Holmes, 2015)

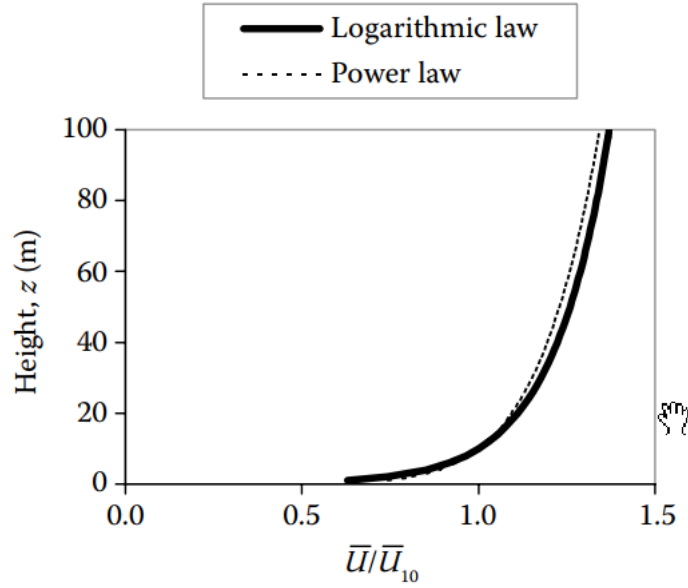


Figure 3.6: A plot of the difference between the power and logarithmic wind profiles between 0-100 meters over the surface Holmes (2015, p. 61)

The mean wind speed at height z is then given by:

$$\bar{u}(z) = \bar{U}_{10} \left(\frac{z}{10} \right)^\alpha \quad (3.8)$$

Where \bar{U}_{10} is the mean wind speed at $z=10$ m, and α is an empirically derived constant.

α is dependent on the surface roughness and height range. α has the following relationship with roughness length z_0 :

$$\alpha = \frac{1}{\ln(z_{ref}/z_0)} \quad (3.9)$$

Where z_{ref} is a reference height at which the power and logarithmic laws coincide, and z_0 is the surface roughness (Holmes, 2015).

3.8 Friction velocity

Friction/shear velocity u_* formulates the shear stresses in the units [m/s]. Numerous studies have been conducted to deduce the relationship between the mass transport rate Q of granular materials (such as sand or snow) and shear stress τ (Iversen, 1981). The shear stresses on the roof are the key flow parameter used to study snow erosion (Liu et al., 2019). Qiang et al. (2021) states that on a flat, open surface, friction velocity is assumed to be equally distributed. However, flow separation will affect friction

velocity on a roof, as seen in Figure 3.7. Bagnold (1974) observed through wind tunnel experiments that a granular particle will not move unless $u_* > u_{*t}$ locally where u_{*t} is the impact threshold. The snow is susceptible to accumulate where $u_* < u_{*t}$. Furthermore, the friction velocity is also proportional to the mean wind speed (Bagnold, 1974). u_* is given by:

$$u_* = \sqrt{\frac{\tau_w}{\rho}} \quad (3.10)$$

where τ_w is the local shear stress on the wall, and ρ is the air density.

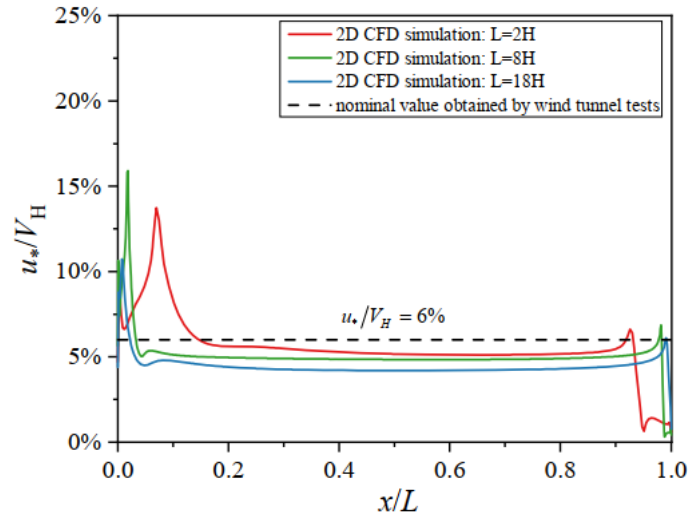


Figure 3.7: u_* distribution on a flat roof obtained using both 2D CFD simulations and wind tunnel experiments (Qiang et al., 2021)

Liu et al. (2019) observes that with the same wind conditions with an increasing building L/H ratio, the average friction velocity decrease, and the mass transport rate increases. Furthermore, they also observed that when the wind velocity increases, the friction velocity increases, and then the mass transport rate.

$\tau_w = \tau_{lam}(z = 0) = \mu \frac{\partial u}{\partial z}$ when the flow is steady and laminar (Bagnold, 1974). When the flow is turbulent an additional turbulent shear stress τ_{turb} contributes. Then $\tau_w = \tau_{lam} + \tau_{turb}$.

3.9 Threshold friction velocity

Threshold friction velocity u_{*t} describes the erodibility of a granular material (like snow). Threshold friction velocity is a function of the critical average shear stress $\bar{\tau}_c$

Snow type and snow properties strongly influence the threshold friction velocity. Nev-

ertheless, the exact values for this influence must often be guessed and are not well understood (JDoorschot et al., 2004). JDoorschot et al. (2004) did field experiments in the Swiss alps and investigated correlations between threshold friction velocity and the snow properties. The strongest correlation was 0.76 with the snow property grain size. The snow grain size is highly variable, and it has a diameter between 0.1 and 0.5 mm. Fresh snow has a smaller diameter beneath 0.5 mm, and it will grow if the snow starts to melt. Schmidt (1980) on the other hand observed that cohesion is more correlating to threshold friction velocity than grain size.

Clifton et al. (2006) measured 15 snow covers and concluded that u_{*t} was more influenced by snow density and grain size than air temperature and humidity. Furthermore Clifton et al. (2006) concluded based on measurements of 15 snow covers that u_{*t} varied from 0.27 - 0.69 m/s. D. and D. (2004) concluded that the threshold value varies from 0.07-0.25 m/s for fresh snow, and 0.22 - 0.40 m/s for aged snow.

As seen in figure 3.8, the forces acting on a snow particle when acted on by the wind are the weight of the particle W , the cohesive bond between the snow grains F_b and lift L_c .

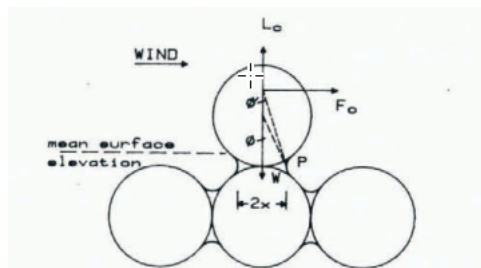


Figure 3.8: Force diagram for forces acting on snow particles with a single cohesive bond (Schmidt, 1980, p. 457)

3.10 Roughness length

"The roughness of a particular surface area is determined by the size and distribution of the roughness elements it contains" Troen et al. (1989, p 56). Examples of roughness elements are infrastructure and vegetation. The locations most exposed to wind are situated in areas with very few or no buildings (Meløysund et al., 2007). The roughness of a terrain can be expressed through the roughness length z_0 . In *NS-EN 1991-1-4. Eurocode 1: Actions on structures - Part 1-4: General actions - Wind actions* (2009), the terrain is categorized based on the size of the roughness length. Figure ?? depicts the terrain categories used in EN-1991-1-4 in ascending order from small to large roughness length.

When doing wind load calculations in *NS-EN 1991-1-4. Eurocode 1: Actions on struc-*

Terrain category		z_0 m	z_{min} m
0	Sea or coastal area exposed to the open sea	0,003	1
I	Lakes or flat and horizontal area with negligible vegetation and without obstacles	0,01	1
II	Area with low vegetation such as grass and isolated obstacles (trees, buildings) with separations of at least 20 obstacle heights	0,05	2
III	Area with regular cover of vegetation or buildings or with isolated obstacles with separations of maximum 20 obstacle heights (such as villages, suburban terrain, permanent forest)	0,3	5
IV	Area in which at least 15 % of the surface is covered with buildings and their average height exceeds 15 m	1,0	10
NOTE: The terrain categories are illustrated in A.1.			

Figure 3.9: The different terrain categories and parameters used in *NS-EN 1991-1-4. Eurocode 1: Actions on structures - Part 1-4: General actions - Wind actions* (2009)

tures - Part 1-4: General actions - Wind actions (2009) z_0 is assumed to be uniform, but this is rarely the case in real life. As the wind enters an area of higher surface roughness than the previous area, the airflow slows down. When the airflow enters an area of lesser surface roughness, the airflow accelerates Kaimal and Finnigan (1994, p. 112). Height variations (i.e., hills and mountains) in the terrain will also affect the mean wind speed depending on the size and shape of the variation.

3.11 Fluid Mechanics Introduction

Fluid mechanics can be described as "(...) a study of the behavior of a gas or liquid that is either at rest or in motion. " (Hibbeler, 2020). Fluid is an umbrella term for a gas or liquid which deforms without limit when influenced by shearing forces (Spurk and Aksel, 2008).

As the volume of the fluid domain is much greater than the distance between the molecules, the fluid can be modeled as continuous, filling the entire domain. This is a simplification that makes it possible to average the properties of the fluid in the domain instead of analyzing each molecule individually (Hibbeler, 2020). These properties are continuous functions of time and space, and the fluid particles can be modeled as material points. This is called the continuum hypothesis.(Spurk and Aksel, 2008)

The fundamental governing equations for fluid dynamics are the continuity equation and the conservation of momentum and energy equations. (Wendt and Jr, 2009)

The continuity equation describes the conservation of mass mathematically. It says that the net mass flows out of a control volume V through surface S equals the time rate of mass decrease inside the control volume. (Wendt and Jr, 2009) The continuity equation in Eulerian form is written as : (The following derivations are found in Gjevik (2002))

$$\frac{\partial \rho}{\partial t} + \nabla \cdot (\rho \mathbf{u}) = 0 \quad (3.11)$$

Where $\rho = \rho(x, y, z, t)$ is the density of the fluid and $\mathbf{u} = \mathbf{u}(x, y, z, t)$ is the velocity field of the fluid (Tritton, 1984)

In a Newtonian fluid the viscous pressures are linear functions of the strain rate tensor components ϵ_{nm} as seen in $P_{ij} = K_{ijkl}\epsilon_{nm}$. Where the coefficients K_{ijkl} are constant. For a fluid with an isotropic (uniform in all directions) pressure p then P_{ij} can be written as:

$$P_{ij} = -p\delta_{ij} + \kappa \nabla \cdot \mathbf{u} \delta_{ij} + 2\mu(\dot{\epsilon}_{ij} - \frac{\nabla \cdot \mathbf{u}}{3}\delta_{ij}) \quad (3.12)$$

Furthermore for an incompressible fluid $\nabla \cdot \mathbf{u} = 0$ (3.12) simplifies to:

$$P_{ij} = -p\delta_{ij} + 2\mu\dot{\epsilon}_{ij} \quad (3.13)$$

For a laminar shear flow in the XZ - plane with a velocity field $\mathbf{u} = [u(z), 0, 0]$ then

$$P_{xz} = \mu \frac{du}{dz} = 2\mu\dot{\epsilon}_{xz} \quad (3.14)$$

By further inspection, this shear flow is a general expression of the logarithmic wind profile (3.7) also because the wind is often regarded as incompressible, as explained in Chapter (3.4).

The primitive form of the equation of motion for a continuous medium is:

$$a_i = \frac{1}{\rho} \frac{\partial P_{ij}}{\partial x_j} + f_i^v \quad (3.15)$$

Where i is the (x,y or z) direction an arbitrary surface is facing , j is the direction the pressure is directed on surface i , a_i is acceleration of the medium element and f_i^v is the volume force (i.e. gravity) in direction i .

Furthermore by calculating $\frac{\partial P_{ij}}{\partial x_j}$ from (3.12) into (3.15) and assuming an incompressible fluid so $\nabla \cdot \mathbf{u} = 0$ the equation of motion for an incompressible Newtonian fluid is:

$$\frac{D\mathbf{u}}{dt} = -\frac{1}{\rho}\nabla p + \frac{\mu}{\rho}\nabla^2\mathbf{u} + \mathbf{f}^u \quad (3.16)$$

Equation (3.16) is more famously named Navier Stokes equation for incompressible fluids. The Navier Stokes equation is a mathematical representation of the conservation of momentum. The continuity equation and Navier stokes equation are used together to solve viscous fluid motion problems.

3.12 Boundary layer

In theoretical fluid mechanics investigations, the fluid is often idealized as inviscid and incompressible. This drastically simplifies the NS. equations. Some fluids have a small viscosity; this is a good simplification for certain fluids. In such a fluid, only normal stresses exist and not tangential/shear stresses. However, in real life, such an idealization is impossible. In a viscous fluid intermolecular attracting forces exist. This causes the fluid to stick to the surface of a wall which results in shearing stresses on the wall. Resultingly, this gives rise to the no slip condition. The frictional forces counteract the motion of the fluid in a thin layer close to the wall. In this layer, the viscous forces are dominant. Inside the boundary layer, fluid velocity increases from zero at the wall to the freestream velocity at the edge of the layer. Outside this layer, the fluid is inviscid, and inertial forces dominate. This layer is called the boundary layer. (Schlichting, 1979)

3.12.1 Turbulent boundary layer

The turbulence inside a fully turbulent boundary layer is inherently 3D and is random. Even though it is random, it still has coherent structures dependent on time scales and range lengths. Even though these turbulence structures have been studied excessively, knowledge has not influenced engineering practice so much. "Of more practical interests are the mean velocity profiles and the strategies that turbulence models have used for predicting them."McLean (2012, p. 139).

The turbulent flow contains eddies with a wide array of lengths and energies. The most significant difference between laminar and turbulent profiles is the huge velocity gradients close to the wall. The most significant gradient occurs in the viscous sublayer as there the shear stress is almost only viscous with no turbulent shear stress τ_{turb} (Reynolds stress). However, there is still turbulence present in the viscous sublayer.(McLean, 2012)

3.13 Flow around a building

The flow around a building can be regarded as bluff-body flow unless the building is streamlined shaped.

The boundary layer formed in the inlet zone is similar to a flat plate boundary layer with no pressure gradients. The boundary layer will grow thicker as it moves along the plate because of viscous diffusion away from the wall.

However, large pressure gradients exist on the building due to the bluff body geometry. The pressure along a wall can be either:

$$\frac{\partial P}{\partial x} < 0$$

called a favorable pressure gradient, or

$$\frac{\partial P}{\partial x} > 0$$

called an adverse pressure gradient.

It will be "difficult" for the flow to move into an adverse pressure gradient. To move into a favorable pressure gradient will be easier as the pressure gradient drives it. Near a wall, the fluid particles in the boundary layer will be accelerated or deaccelerated based on the pressure gradient $\frac{\partial P}{\partial x}$.

In an adverse pressure gradient, the fluid deaccelerates and loses momentum. The relationship between the pressure gradient and the shear stress can be expressed as:

$$\frac{\partial \tau}{\partial z} = \mu \frac{\partial^2 u}{\partial z^2} = \frac{\partial P}{\partial x} \quad (3.17)$$

The maximum shear stress will be at the inflection point in a boundary layer with pressure gradients. No flow separation will occur in a favorable pressure gradient. The inflection point is at the wall, as seen in Equation 3.17. Furthermore, there is no flow separation in a weak adverse pressure gradient, and the maximum shear stress is away from the wall. If $\frac{\partial P}{\partial x}$ becomes larger there is a critical adverse pressure gradient. Here flow separation will occur, and the wall shear stress is zero at the wall. Lastly, if an excessive pressure gradient occurs, backflow will happen, and the shear stress at the wall is negative. Additionally, separation also occurs here.

In real life, the wind is turbulent, and its direction varies continuously. The airflow creates pressure fluttering on the building surfaces in correspondence with the variations

of the approaching flow. The flow surrounding the building is very dynamic because the air must pass over and around the building. The airflow approaches the building wall surface, and at H_{sep} , a stagnation point will occur. Here the mean wind speed $\bar{U} = 0$, and the positive pressure is at maximum. From here, the wind diverges to all the surface edges. When the flow encounters an edge, it will separate as the pressure increase is too large to overcome. The separated air will be very turbulent and have a significantly lower mean wind speed than the free stream speed. (Oke et al., 2017). Below the separation zone, the air that hits the ground will form into a vortex. Convection will cause this vortex to wrap around the side of the building along the ground, which is called a horseshoe vortex. (Peterka et al., 1985). If $L/H > 1$ then the flow re-attaches to the wall and roof (Oke et al., 2017). The flow field around a building for wind approaching normal to the building face and normal to the corner on a square building is shown in Figure 3.10 and 3.11.

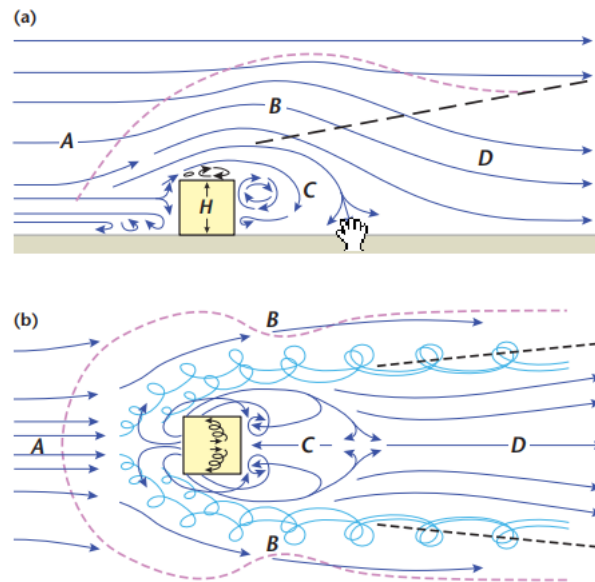


Figure 3.10: Flow pattern around building from wind direction 0° (Oke et al., 2017)

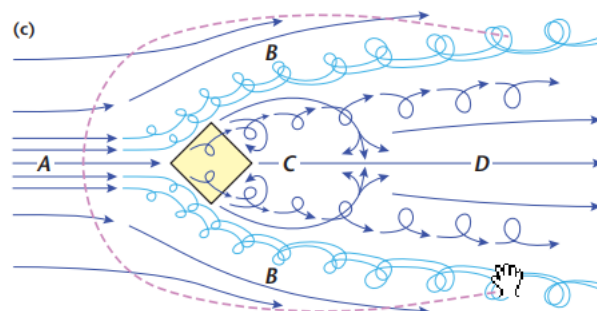


Figure 3.11: Flow pattern around building from wind direction 45° (Oke et al., 2017)

Reattachment depends on the building length-to-width ratio, height to-length ratio, and surface roughness. Roughness determines the turbulence intensity. (Peterka et al., 1985)

When boundary layers are separate, a shear layer is created. The shear layers create waves that turn into vortices and grow downstream. These shear layers are unstable as the inflection point is in the velocity profile and not on the inside or the wall.

Chamfering the edges will reduce the amount of flow separation (Aly and Bresowar, 2016).

3.14 CFD

Computational fluid dynamics (CFD) is a way of analysing systems involving fluid flow through computational numerical simulations. (Versteeg and Malalasekera, 2007) Numerical algorithms solve these systems involving fluid flows. The Navier-Stokes equations can today only be solved analytically for a handful of special cases, and that is why CFD is so valuable. CFD solutions have been in use since the 1950s. Today the use of CFD is so influential that it can be viewed as the third pillar of fluid dynamics together with pure theory and pure experiment (Wendt and Jr, 2009). All CFD codes contain three elements: a pre-processor, a solver, and a post-processor. In the pre-processor, the user defines the computational domain, the grid, and fluid properties and specifies the boundary conditions. The grid/mesh is generated by subdividing the domain into many smaller, non-overlapping sub-domains. Each of these small sub-domains is called a cell or a control volume. (Versteeg and Malalasekera, 2007)

3.14.1 Single and mutiphase simulations

CFD simulations solve the flow field around the building, which allows for the evaluation of snow transport. In past snow transport literature, either a single-phase or two-phase simulation is completed. Most studies implement double-phase simulations. A single-phase simulation only simulates the air. Meanwhile, the double phase simulation additionally simulates the coupling between the air and snow particles which can be used to simulate the movement of the snow particles as a function of time.

A single-phase simulation cannot be used to study the time and space dependency of the snowdrift. It will show which areas are receptive to initial snow transport based on the local friction velocity. The requirements for snow transport are explained further in Chapter 3.2.

Meanwhile, in a two-phase simulation, moment transfer between the wind and snow

particles will be modeled, but this is not the case for a single-phase simulation. The momentum transfer will change the vertical velocity distribution of the airflow (Huang and Zhang, 2008). This effect on the velocity profile is observed in (Kikuchi, 1981) as more pronounced at higher wind speeds. As concluded in (Kikuchi, 1981), the coupling has a significant effect on the particle trajectory of the snow particles.

3.14.2 Steady state and transient simulations

The time depends on the flow can be either steady-state or transient. A steady-state's flow characteristics are constant with respect to time. The solution has reached a steady state after a long amount of time. A steady-state solution is valid if the flow does not vary with time. This requires; a steady flow phenomenon, constant boundary conditions, and constant device behavior. A steady flow is a type of flow where the fluid properties are constant over time. This can be written mathematically as $\frac{\partial O}{\partial t} = 0$ where O is a fluid property and t is time.

Meanwhile, transient solutions are time-dependent and require time intervals when the CFD-solver resolves the flow field. All flow parameters have to be calculated at each time step. Transient solving is used for time-varying flows.

A transient simulation is needed when the result variable varies in time. This is often happening if there is a rotating region, free surface(s) or if the user wants to examine the motion of the flow. Furthermore, varying boundary conditions will also make it necessary to use a transient analysis method.

A transient simulation takes a lot longer to solve than a steady-state simulation. A steady solution can have issues with divergence, even with a good mesh quality. The cause of this can be from the transient nature of the flow, which causes transient effects in the flow like vortex-shedding. The RMS momentum residuals will oscillate with a constant period and not converge.

In addition, a steady-state solution does not account for the effect of the moment transfer that occurs when saltating snow grains contact with the snow bed, resulting in the ejection of additional snow grains into the air. The splash function describes this effect. (Liu et al., 2019)

3.14.3 Turbulence modelling

Infrequently is a flow system in the atmosphere undisturbed, moving over horizontal planes. In a turbulent flow field, velocity and pressure fluctuate erratically in all directions. Navier Stokes equations cannot be solved for a turbulent flow field because they are elliptic, nonlinear, and coupled. This flow regime also has an infinite number

of degrees of freedom, so a complete resolution of the flow requires $Re^{9/4}$ grid cells. A flow over a flat plate is characterized as turbulent if $Re > 5 \times 10^5$ so the flow requires a minimum of $(5 \times 10^5)^{9/4} = 6.6$ trillion cells to satisfy this. (Saad, 2004)

RANS

By employing Reynolds decomposition, the number of degrees of freedom can be minimized. Here, every scalar or velocity can be expressed as the mean plus the standard deviation. This is crucial since turbulence is, by definition, extremely variable. These equations will be exact for a flow in which all vectors and scalars remain constant throughout time, but not for a turbulent flow of the same type. Reynolds Averaged Navier Stokes equations are derived by inserting the Reynolds decomposition into the Navier-Stokes equations (RANS). By solving these equations, time-averaged solutions to the NS equations can be obtained. RANS provide additional turbulent stress unknowns $\tau = \rho \overline{u'_i u'_j}$. u'_i and u'_j are fluctuating velocity components. These unknowns can be solved by the use of turbulence models by relating the unknown to the mean flow variables (U, V, W). (Saad, 2004).

RANS is computationally inexpensive and the most used method in industry applications. It is a good enough representation of the reality inside the wind tunnels. Still, as it disregards the time dimension, it is unclear if the equations adequately model inherently unstable meteorology Franke and Baklanov (2007, p. 13). RANS does not handle flow separation as well as LES and DNS (Breuer et al., 2003).

The turbulent flow will contribute by additional shear stress τ_{turb} . It is given by:

$$\tau_{turb} = -\rho \overline{u'_i u'_j} = \mu_t \left(\frac{\partial U_i}{\partial x_j} + \frac{\partial U_j}{\partial x_i} \right) \quad (3.18)$$

Furthermore, the turbulent kinetic energy due to these fluctuations can be expressed as:

$$TKE = \frac{1}{2} (\overline{u'^2} + \overline{v'^2} + \overline{w'^2}) \quad (3.19)$$

k- ω SST turbulence model A general-purpose turbulence model is not yet available with RANS. A RANS turbulence model has to be selected to provide a satisfactory solution based on the geometry and flow field studied.

SST κ - ω is a two-equation eddy viscosity turbulence model developed by Dr. Florian Menter Versteeg and Malalasekera (2007, p 91). The two partial differential equations are turbulent kinetic energy TKE and turbulent dissipation rate ϵ_k . It is a hybrid model of the κ - ϵ and κ - ω two-equation turbulence models. The κ - ϵ model is independent of the

assumed free stream, but it has the undesired trait of performing poorly in boundary layers with adverse pressure gradients. Meanwhile, the κ - ω is performing well inside the boundary layers but is dependent on the assumed free stream values, and this is highly problematic in external aerodynamics (Versteeg and Malalasekera, 2007). Dependence of the free stream values means that the choice of free stream inlet turbulence can change the solution. SST k - ω uses a blending function, so k - ω is used near the wall, and k - ϵ is used far away from it. SST has the best of both worlds; independence of free stream values and can account for the principal shear stress transport inside adverse pressure gradient boundary layers. Therefore, SST attempts to give a better separation prediction. The model is based on the fact that principal shear stress τ_{ij} is proportional to turbulent kinetic energy TKE. And that a good turbulence model should be sufficiently accurate for the usage area and not have an excessive computation time. (Menter, 1993)

LES

RANS models the behavior of small and large eddies with the same turbulence model through time-averaging. In the real world, the behavior of the large eddies is highly problem-dependent. Meanwhile, the smaller eddies behave independently of the case analyzed. LES uses a more complex time-dependent method to model the large eddies. And a simpler model to represent the small eddies. Meanwhile, the computational cost of LES is substantially compared to two-equation RANS models. LES will most likely be the industry-leading method in the future, but it needs further research. (Versteeg and Malalasekera, 2007)

DNS

DNS solves the continuity and N.S equations for an incompressible flow directly without a turbulence model. It can provide results that are not experimentally measurable. Meanwhile, it needs a mesh of $Re^{9/4}$ grid points. This makes the computational cost extreme; however, the number of grid points can be reduced in many cases (Versteeg and Malalasekera, 2007).

3.14.4 ANSYS CFX

ANSYS CFX 2021 R2 is a commercial, industry-leading general-purpose fluid dynamics software used to solve fluid flow problems. Ansys CFX can either be run through Workbench or the standalone CFX 2021 R2 application. CFX 2021 R2 consists of the pre-processor CFX-Pre, the solver CFX-Solver, and the post-processor CFX-Post.

Inflation layers

Inflation layers are thin prism layers used to resolve the boundary layers forming near walls. The user inputs the number of cells N and the growth rate. The growth rate decides how much higher cell i from the surface is than cell $i-1$. The height of the first layer is selected to achieve a value for y^+ by the formula:

$$y^+ = \frac{\rho u_\tau y_p}{\mu} \quad (3.20)$$

The CFD solver calculates and stores the solution most often at the centroid of the cell. Between the cell centroids, the flow variables (velocity, temperature, and pressure) vary. This variation is approximated linearly by the CFD solver. The flow variables don't necessarily vary linearly between cell centroids. In certain areas, these variations/gradients might be quite large, and in these areas, many small cells are needed to approximate a smooth non-linear function with many piece-wise linear ones. Velocity gradients are large perpendicular to a surface and are much smaller parallel with the wall. This can be seen by $\frac{\partial u}{\partial z} \gg \frac{\partial u}{\partial x}$. (*Understanding impact of y^+ on flow resolution 2020*) (Versteeg and Malalasekera, 2007)

It's often wanted to have the whole boundary layer inside the inflation layers as the inflation layer cells are small. A too-large volume change between neighboring cells in the free stream area and inflation layer will lead to an error in the local velocity gradient at that cell. This will then lead to an error in the local shear stress.

Face sizing

Face sizing is a local mesh control used to create a specified mesh on selected surfaces. It can be used to set the length of the inflation layers.

3.14.5 Convergence

The governing equations that the CFD-solver solves are non-linear equations with the turbulence that creates inherent instability. For a steady-state solution, the solver will iterate using false timesteps, with each timestep improving the solution until convergence is reached. A converged solution is used to indicate that a valid solution is present. Several convergence criteria should be used to verify the solution's accuracy. One of the most practical and well-defined criteria to use is to look at the Root Mean Square/ RMS residuals. The residuals are "measures of the overall conservation of the flow properties" (Versteeg and Malalasekera, 2007, p. 5). In industrial applications, a termination criterion of 0.001 is typically employed which is typically too achieve convergence (Versteeg and Malalasekera, 2007). A termination criterion for the residuals of at least 0.0001

is recommended (Franke and Baklanov, 2007). In *Ansys CFX Reference Guide* (2021, p. 130) non-swirling flows are indicating convergence at 0.001-0.0001. By default, CFX defines the convergence criterion of the residuals is equal to 0.0001. Furthermore, a more thorough convergence check can be completed by investigating the physical reality of the flow in the post-processor, the target solution variables, and the integral balances of mass, momentum, and energy. If the target variables go towards a constant value or oscillate around it and the integral balances move towards zero, the solution can be considered converged. (Franke and Baklanov, 2007)

These choices are dependent on the problem studied, and there are therefore no global guidelines to follow. This is why experience with CFD is vital to be able to define a reasonable solution Versteeg and Malalasekera (2007, p. 5).

3.14.6 Boundary conditions

After the geometry is specified, the boundary flow properties must be defined in the domain. The flow properties described on each face of the domain are called boundary conditions. The user must specify the flow properties correctly and realistically to achieve a good CFD solution.

Inlet

The inlet is the surface where the flow will enter the domain. If the wind is modeled with a wind profile, it will only have an x-component. Turbulent intensity also needs to be specified.

Outlet

The outlet is the surface where the flow will exit the domain. The outlet distance should be larger than the inlet distance. A too-short downstream length causes recirculation flow which can affect the flow around the building (Abu-Zidan et al., 2021). Here a static average outlet pressure needs to be defined and turbulent intensity. In ANSYS CFX, the flow exit surface can be modeled as an "outlet" or "opening". The difference is that an "outlet" does not allow backflow while an "opening" does. (*Ansys CFX-Solver Theory Guide* 2021)

Walls

At a stationary wall, the fluid in contact with the wall will have zero velocity. This is called the no-slip boundary condition. In ANSYS CFX, the user can choose to model the wall as rough or smooth. As all wall surfaces are inherently rough, the smooth wall is an idealized form of a rough wall. For a rough wall, the user has to input a sand grain

roughness K_s [m], which is uniformly distributed along the wall as shown in figure 3.12. K_s and z_0 are related through the following equation, $K_s = z_0 \exp \kappa 8.5$ where κ is the von Karman constant. $K_s = 0$ results in a smooth wall. $K_s > 0$ can significantly change the flow near the wall and will lead to more turbulence production, which can lead to significantly increased shear stress near the wall. Because of the turbulent flow, the viscous sublayer will be more and more destroyed for higher K_s values. For a smooth wall, the viscous sublayer is fully established. A rough wall will have a reduction of u^+ in the viscous sublayer because of an additional negative term $f(h^+)$ in equation 3.21 (*Ansys CFX-Solver Theory Guide 2021*).

$$u^+ = \frac{1}{\kappa} \ln y^+ + B - f(h^+) = \frac{1}{\kappa} \ln y^+ + B - f\left(\frac{K_s u_*}{\nu}\right) \quad (3.21)$$

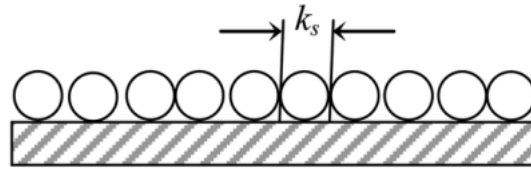


Figure 3.12: Sand equivalent grain roughness K_s is used to model rough walls (Hetsroni et al., 2011)

K_s is defined as $K_s = 29.6z_0$ in Ansys CFX with the added requirement of $K_s \leq y_p$. (Blocken et al., 2007)

Symmetry

A symmetry plane assumes that the gradients perpendicular to the plane are zero (*ERC-OFTAC Best Practice Guidelines - Industrial computational fluid dynamics of single phase flows 2000*, p. 31). This can generally be expressed as $\frac{\partial O}{\partial n} = 0$ where O is a flow property, and n is a vector normal to the symmetry plane.

3.14.7 Mesh

Subdivision of the domain into smaller cells makes it possible to analyze the fluid flow. The cells are shaped as hexahedrons or tetrahedrons. Each cell's nodes store the solution to a flow property (velocity, pressure, temperature, etc) (Versteeg and Malalasekera, 2007). In general, by increasing the number of cells, the solution accuracy will increase, but the calculation time will also increase. An effective mesh is created by having smaller cells where large gradients occur and coarser cells where there are small gradients. The challenge is to create a mesh that is a suitable compromise between computational cost and desired accuracy.

There are many ways of meshing, and the user has to decide on a mesh type based on the geometry complexity, the shape of the domain, and the experience of the user. The main two mesh types are structured grids and unstructured/hybrid grids. CFX meshes based on the kind of method control selected.

Mesh quality

ANSYS CFX has a built-in calculator that calculates all cells' quality based on metrics used in the industry. Skewness, volume transition, and orthogonality are most relevant for inflation layers. Aspect ratios are not a concern in the boundary layer as aspect ratios can be in the order of 10^3 here. But aspect ratios should not be larger than 20-50 far away from the wall *Ansys CFX Reference Guide (2021)*. It is especially crucial to have a sufficient cell quality in the boundary layer for a reliable solution. Furthermore, as mentioned in Chapter ?? the y^+ value suggests how refined the mesh is, but a poorly refined volumetric mesh can be used together with a low y^+ value. The resulting mesh will perform poorly because of the insufficient cell quality. (*Ansys CFX Reference Guide 2021*)

Skewness Skewness is a quality metric that indicates how close to an equiangular or equilateral a cell is. A cell with poor quality will give a poor solution in that cell as the equations being solved assume relatively non-skewed cells. A skewness score for a cell ranges from 1 to 0, where 0 is an equiangular or equilateral cell. A quality mesh has a score below 0.1 in 2D and below 0.4 in 3D (*Ansys Meshing User's Guide 2021*).

"In 3D, most cells should be good or better, but a small percentage will generally be in the fair range, and there are usually even a few poor cells" (*Ansys Meshing User's Guide 2021*). The score "Good" has a value range between 0.25-0.5.

Orthogonality Orthogonal quality is a quality metric that ranges from 0 to 1, where one is the best.

\vec{A}_i is the face normal vector for each face, \vec{f}_i is the vector from the cell centroid to each of the faces, and \vec{c}_i is the vector from the centroid of the cell to the centroid of the neighboring cell. The vectors and their adjacent cells are shown in figure 3.13. The cosines of the angles between \vec{A}_i and \vec{f}_i , and between \vec{A}_i and \vec{c}_i . The smallest of the cosines determines the orthogonality of the cell. The orthogonal quality for a tetrahedral or prism-shaped cell is minimum(orthogonality, 1- skewness) *Ansys Meshing User's Guide (2021)*.

Volume transition RANS The volume transition between the cells in the inflation layers and the surrounding cells must be smooth. The difference in the volume of the inflation cell should be in the range of 1-2. (*Ansys CFX Reference Guide 2021*)

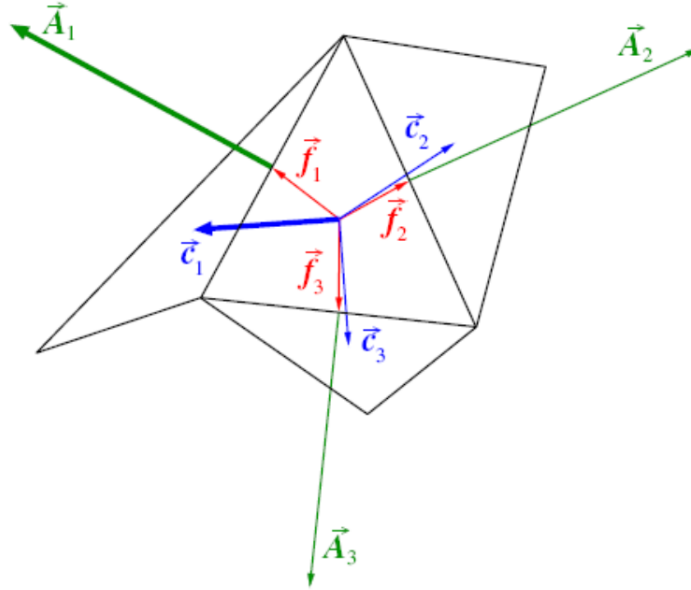


Figure 3.13: Vectors used to calculate orthogonality for a cell surrounded by neighbouring cells *Ansys Meshing User's Guide* (2021, p. 142)

3.14.8 Wall functions

A viscous flow has large gradients close to the wall due to the no-slip condition where $\mathbf{u} = 0$, which forms a boundary layer. A sufficient high grid resolution is needed to accurately resolve the gradients (Bredberg, 2000). These cells have a high aspect ratio which leads to poor cell quality. Furthermore, this can lead to instability and even divergence. The grid cells normal to the wall get increasingly thinner and thinner closer to the wall, leading to a high cell count. Cell count and computational time is proportional to each other. These gradients can be solved by many piece-wise linear functions, one linear function between each cell centroid. Another way of solving the gradients is by replacing the thinner cells with a larger cell containing a non-linear function instead called a wall function. This will make it possible to use larger cells and reduce the total computation time and cost. (Bredberg, 2000).

The solid line in Figure 3.14 is a plot of the observed normalized tangential velocity U/u_* and the normal wall distance y_+ . The velocity profile $U/u_* = f(y_+)$. Wall functions are the empirical functions (dashed lines) used to model the normalized tangential velocities to model the flow behavior close to the wall. The area close to the wall might be separated into three different regions depending on the distance from the wall y_+ as described in Table 3.1 (Tennekes and Lumley, 1972):

As seen in Table 3.1 the y_+ range of 0-5 is well modelled by the wall function $U/u_* = y_+$. Furthermore, the inertial sublayer is well modelled by the wall function $U/u_* = \frac{1}{\kappa} \ln(y_+) + B$. However, in the buffer layer in the y_+ range of 5-30 the wall functions

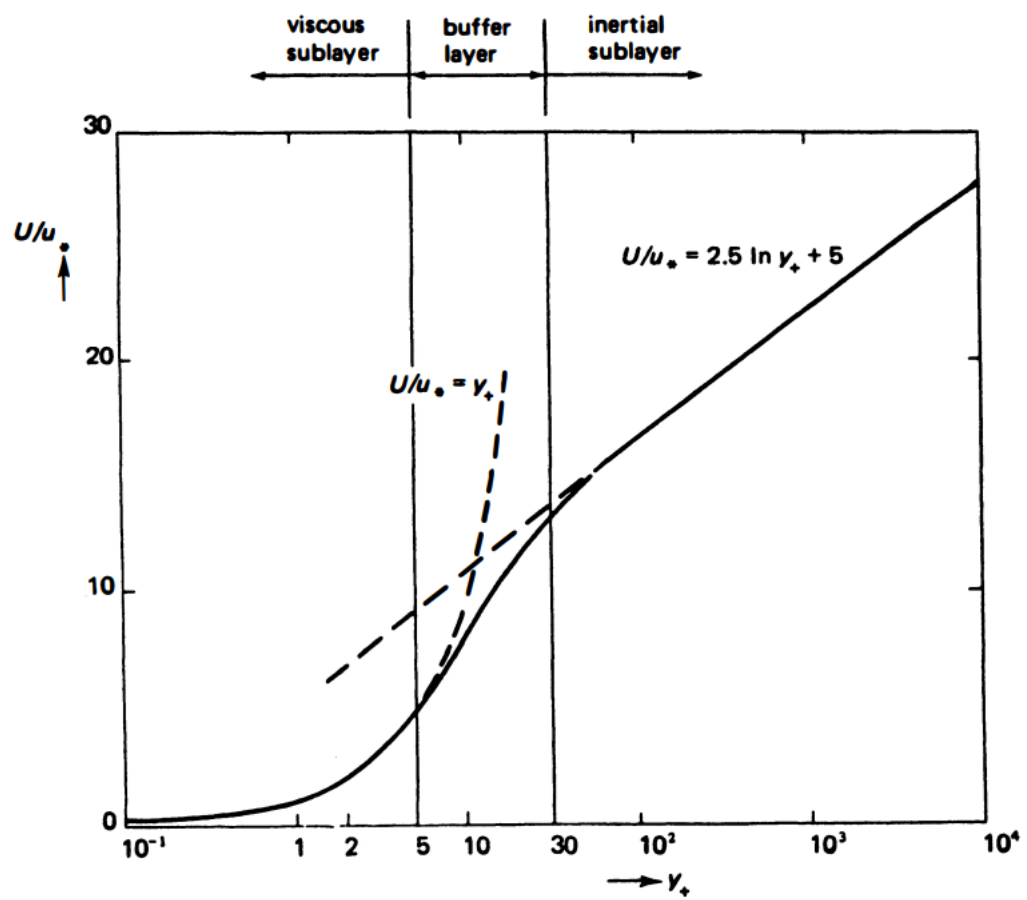


Figure 3.14: Law of the wall Tennekes and Lumley (1972, p. 160)

there are large discrepancies between the wall functions and the observed data. ANSYS CFX mitigates this by implementing an *automatic* wall function which uses a automatic blending function in the buffer layer to approximate U/u_* there. CFX ANSYS will use integration to the wall if y^+ is between 0-5, use a blending function between 6-30 and switch to wall function if $y^+ > 30$.

Table 3.1

Region	y^+ range
Viscous sublayer	$0 < y^+ < 5$
Buffer layer	$5 < y^+ < 30$
Inertial sublayer	$30 < y^+ < 200$

3.14.9 Y^+

The boundary layer thickness δ_{99} varies with flow properties as Re and geometrical properties as the distance from the leading edge. To ensure that the boundary layer profile is adequately scaled, a dimensionless distance y^+ is established. (Versteeg and Malalasekera, 2007)

y^+ is a dimensionless distance from the wall to the first cell centroid. It is used as an indicator of the fineness of the mesh in the CFD world. As observed in Chapter 3.14.8, it's generally recommended to use y^+ between 0-5 or larger than 30 as the blending function might be inaccurate. It is defined as

$$y^+ = \frac{\rho u_* y}{\mu} = \frac{u_* y}{\nu} \quad (3.22)$$

3.14.10 Similarity solutions

In wind tunnel experiments scaling is used as full-scale simulations often are logistically impossible to conduct.

Two solutions of different scales can be regarded as completely similar if some requirements are achieved. These are that the geometric, kinematic, and dynamic similarities are satisfied. Geometric similarity implies that the scaled model has the same shape and all the linear dimensions have the same scale ratio as the full-scale model. Kinematic similarity means that the streamlines are equally shaped between the scaled and full-scale models. Lastly, dynamic similarity implies that the ratios of the forces are similar. This means that all the independent π groups have to be equal whatever the scale used. This is the most difficult requirement to satisfy and often not achievable. However, not all the force ratios are relevant to the problem studied.

Additionally, if a steady-state analysis is completed, the time scale can be disregarded. Also, the similarity between turbulence intensity and turbulence length scale can be relaxed in a steady-state simulation. Therefore, the similarity analysis can be considerably simplified Wang et al., 2013.

The Reynolds number(Re) is one such independent π group. It represents the ratio between inertial and viscous forces. Versteeg and Malalasekera (2007, p. 57). It can be given by:

$$Re = \frac{\rho U_0 L}{\mu} \quad (3.23)$$

where ρ is the density and μ is the dynamic viscosity.

3.14.11 Errors sources in CFD simulations

Any numerical solution will provide errors compared to the analytical solution. Both experimental wind tunnel studies and numerical CFD simulations have to be used to approximate the flow parameters as analytical solutions are not available. The user has to be able to identify and quantify the errors to study the realism of the solution. CFD simulations have a wide range of potential error sources. *Ansys CFX Reference Guide* (2021) categorizes the errors into Numerical errors, modeling errors, user errors, application uncertainties, and software errors.

Error and uncertainty are responsible for the loss of accuracy in a solution. The difference between them is *ERCFTAC Best Practice Guidelines - Industrial computational fluid dynamics of single phase flows* (2000, p. 4):

An error is " a recognizable deficiency in any phase or activity of modeling and simulation that is not due to lack of knowledge.". While uncertainty is " a recognizable deficiency in any phase or activity of modeling and simulation due to lack of knowledge." (*ERCFTAC Best Practice Guidelines - Industrial computational fluid dynamics of single phase flows* 2000)

Numerical errors

"The goal of a numerical solution is to reduce the error below an acceptable limit" *Ansys CFX Reference Guide* (2021, p. 113). Solution error can generally be expressed by:

$$E_s = \frac{f_{exact} - f_{numeric}}{f_{exact}} \quad (3.24)$$

A grid independency study is a method to reduce the numerical errors by increasing the

mesh resolution until the solution is independent of it. Typically, the study begins with a coarse mesh and gradually refines it until the solution no longer changes.

The numerical error is reduced by 50 % when doubling the grid resolution. If the error is acceptable, it is unnecessary to increase the grid resolution as this will increase the computational cost of the simulation. (*Ansys CFX Reference Guide 2021*)

Modelling errors

As mentioned in chapter 3.14.3, RANS equations are a result of averaging the equations. The turbulence model then reintroduces the information lost from the full NS equations. Wrong model implementation can cause errors exceeding 100 %. Some models are only suitable for specific applications, or the CFD solution is sensitive to the turbulence model selected (*Ansys CFX Reference Guide (2021)*). There is no turbulence model which is accurate for all flow types. The solution can vary widely when the user changes the turbulence model while using the same grid (*ERCRAFTAC Best Practice Guidelines - Industrial computational fluid dynamics of single phase flows 2000*).

User errors

Furthermore, user error occurs when the user does not use the available resources adequately. Examples of resources are the CFD software, computing power, and the problem description. Sources of these errors are lack of experience or attention to detail. The most normal user errors are setting up the boundary conditions incorrectly, poor geometry and mesh generation, using non-converged solutions, and oversimplifying the problem. (*Ansys CFX Reference Guide 2021*)

Application uncertainty

Application uncertainties occur because the user has insufficient knowledge of the simulation. Approximations have to be done to minimize the uncertainties. An example of application uncertainties can be a lack of boundary condition information or uncertainty in the experimental data (*Ansys CFX Reference Guide 2021*).

Software errors

Software errors are rare but can occur because of software bugs or documentation errors (*ERCRAFTAC Best Practice Guidelines - Industrial computational fluid dynamics of single phase flows 2000*).

Outliers

Hawkins (1980) defines an outlier as "an observation which deviates so much from other observations as to arouse suspicions that it was generated by a different mechanism". The effect the mechanism has on the dataset depends on the mechanism which creates the outliers. The two groups of mechanisms that create these outliers are; 1) If the dataset arises from a heavy-tailed distribution or 2) if the data comes from two distributions. Where one of the distributions contaminates the other "good" distribution. If mechanism 1) is the reason for the outliers, then the outliers are valid observations despite the appearance. Furthermore, if mechanism 2) is the cause of the outliers and the contaminating distribution is known, removing that distribution will remove the outliers. If the contamination distribution is not known, then robust estimators should be used. After that, the outliers can then be deleted from the dataset (trimming) or set equal to a prefixed value closer to the center of observation (Winsorization). If mechanism 1) is the cause of the outliers, then Winsorization should be used over trimming. On the other hand, if mechanism 2) is the cause, then trimming or assigning them smaller weights should be done (Hawkins, 1980).

4. Methods

The research question addressed in this master thesis is typically resolved using either CFD simulations or wind tunnel measurements. CFD simulations were chosen as the method as wind tunnel experiments were not available. This chapter will explain the grid independence study, the model, analysis method, and verification used in this thesis.

4.1 Grid independence study

A grid independence study was conducted to reduce the numerical error in the simulations, create a cost-efficient mesh and to be able to verify the quality of results. The study was conducted by comparing 2D CFD simulations with wind tunnel measurements from Ferreira et al. (2019). The geometry studied is a rectangular box with $H \times W \times L = 0.3 \text{ m} \times 1.2 \text{ m} \times 0.6 \text{ m}$. In that study, the shear stresses were measured with Irwin probes which are sensors commonly used for this in near-wall regions in wind tunnel studies (Brito et al., 2021).

$$C_f = \frac{\tau_w}{0.5\rho U_0^2} \quad (4.1)$$

From the shear stresses a non-dimensional friction coefficient C_f could be calculated given by equation 4.3. τ_w is the shear stress on the wall, ρ is the air density, and U_0 is the undisturbed wind velocity. An extensive validity study was done in Ferreira et al. (2019), where CFD simulations with numerous turbulence models with different mesh resolutions were tested and compared to the wind tunnel measurements. This master thesis compared the best fitting turbulence model of that study, the $k-\omega$ SST, by examining different mesh resolutions. Also, RNG $k-\epsilon$ was briefly tested. The meshes tested are presented in Table 4.1.

The meshes are hybrid meshes which mainly consist of tetrahedrons, wedges, and prism-shaped inflation layers on the ground and the building faces. The inflation layer height is the same on all surfaces to resolve the gradients close to the walls. The domains' cells are notably rougher furthest away from the building and finer, closer to the walls

Table 4.1: The meshes involved in the grid independence study. " y^+ " denotes the range of y^+ values measured on a straight line in the middle of the roof in the wind direction direction.

Case	Turbulence model	y^+	First inflation layer height [m]	Face sizing [m]	Growth rate , G	Number of layer, N
1	SST	65-25	0.00229	0.015	1.3	16
2	SST	65-15	0.00229	0.010	1.3	16
3	SST	40-14	0.00135	0.025	1.2	12
4	RNG	92-28	0.00270	0.05	1.2	12
5	SST	245-90	0.00857	0.092	1.2	12

to reduce the number of cells. An approximate y^+ can be calculated using flat-plate boundary theory (White, 2015, p. 467). The user must calculate the first layer height y_H , the number of layers N , and the growth ratio G as described below. Firstly, the Reynolds number is calculated from Equation 4.2.

$$Re = \frac{\rho U_0 L}{\mu} \quad (4.2)$$

Re is then inserted into Equation 4.3 to calculate C_f . This equation is an empirical correlation to estimate C_f .

$$C_f = (2 \log(Re) - 6.5)^{-2.3} \quad (4.3)$$

The wall shear stress τ_w is calculated from C_f based on Equation 4.3. Then an approximate u_* is calculated from Equation 3.10. The necessary first layer inflation height y_H is calculated based on the choice of y^+ based on Equation 3.22.

The boundary layer thickness δ_{99} should be thinner than the total inflation layer height y_T to ensure that the boundary layer is completely encapsulated inside the thin inflation layers. For simplicity, this can be set as an equality in Equation 4.5. The user has to decide the value for the two independent values G and N in Equation 4.5. *Ansys CFX Reference Guide (2021)* recommends $G < 1.30$ and to instead increase the number of layers N .

For a turbulent flow like $Re < 5E+5$ then

$$\delta_{99} = \frac{4.91L}{\sqrt{Re_L}} \quad (4.4)$$

,where L is the length of the building roof.

$$\delta_{99} = y_T = y_H \frac{1 - G^N}{1 - G} \quad (4.5)$$

Firstly, a coarse mesh is created by using a high y^+ value, increasing the volume mesh resolution, and decreasing the first layer height until the mesh is approximately independent of the grid resolution.

The domain will always affect the flow, and to reduce computation cost and time, it is preferred to reduce the domain size until the effect on the flow is negligible. The mesh from case 1 is selected. The domain sizes for the various size categories are shown in Table 4.2. The large domain has the dimensions $38H \times 20H \times 10H = 7600 H^3$, the medium domain $30H \times 15H \times 8H = 3600 H^3$, the small domain: $15H \times 10H \times 7.5H = 1125 H^3$.

Table 4.2: Study of the chosen mesh's (case 1) domain size dependency. The domain size is given in the building height H . x_D denotes domain dimension x .

Case	Size category	Domain size ($H_D \times W_D \times L_D$)	Turbulence model	y^+
1L	Large	$38H \times 20H \times 10H$	SST	65-25
1M	Medium	$30H \times 15H \times 8H$	SST	65-12
1S	Small	$15H \times 10H \times 7.5H$	SST	70-15

4.2 3D simulations

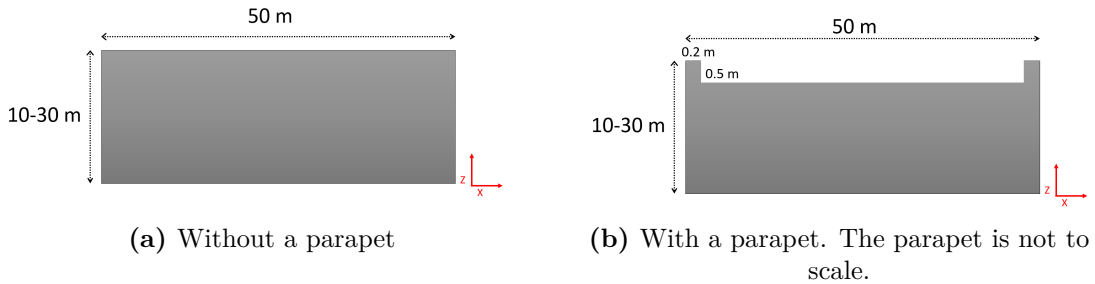


Figure 4.1: Building geometries for the 3D simulations

4.2.1 Building geometries

The buildings examined in this study are flat-roofed buildings with and without parapets with a constant length and width of 50 meters and varying heights of 10, 20, and 30 meters. A flat roof was chosen as this is the base case to study which the calculations of other roof shapes are based on. Assuming a length scale of 1:100 with building dimensions Length(L) \times Width (W) \times Height(H) = 0.5 m \times 0.5 m \times (0.1, 0.2, 0.3) m. The parapet has the dimensions Width(W_p) \times Height (H_p) = 0.02 m \times 0.05 m. The

roofs are horizontally flat, and all edges are sharp, not chamfered. Wind from three different wind directions were studied; $\theta = 0^\circ$, $\theta = 22.5^\circ$ and $\theta = 45^\circ$. Only three wind directions are needed to capture wind from all directions, as all the roof surfaces studied are squares with four symmetry axes. Wind from $\theta = 0^\circ$ is normal to the face edges, and $\theta = 45^\circ$ is normal to the corners of the building. In total, 18 geometries are individually meshed in ANSYS Mesh. The reason for deciding on a building of 50 meters is because C_e is not fixed for such a long building in NS-EN-1991-1-3:NA-2018 (*NS-EN 1991-1-3. Eurocode 1: Actions on structures - Part 1-3: General actions - Snow loads 2018*) table NA.5.1. Buildings with flat roofs have parapets to avoid water dripping on the façade and it makes it safer to stay on the roof. It was, therefore, necessary to simulate both instances. The geometries for a general building with and without a parapet is shown in Figure ?? and ??.

All of the geometries were drawn in Rhino 7 using the *solid* – tools, which outputs a rectangular cuboid. *Boolean difference* were used to make CFX able to differentiate between the solid and fluid domains. Similarly, the parapets are created with *Boolean difference*.

4.2.2 Wind model

The power law wind profile (Eq. 3.7) was used in all the simulations. Wind profiles are often used in these types of studies. The power law was used to avoid issues with the logarithm of zero. The power and logarithm law wind profiles can be regarded as similar in the flow range. This wind profile does not directly contain a z_0 term as the logarithmic law, but α and z_0 have the following relation (Eq. 4.6), as also explained in Chapter 3.7.

$$\alpha = \left[\ln\left(\frac{z_{ref}}{z_0}\right) \right]^{-1} \quad (4.6)$$

where z_{ref} is a height where both the logarithmic and power-law matches.

$z_0 = 0.05\text{m}$ and $z_0 = 0.3\text{m}$ from 3.9 were inserted in to Equation 4.6 to calculate α . Resultingly, $\alpha = 0.18$ corresponds to $z_0 = 0.05\text{m}$, and $\alpha = 0.28$ to $z_0 = 0.3\text{m}$. The power law and logarithmic profile is in this instance nearly identical. The power law wind profile in Equation 3.8 has $U_0 = 11.1 \text{ m/s}$ to ensure a high enough Reynolds number to have a turbulent flow regime.

The turbulent inlet density was set equal to 10 % as most similar studies set it between 5 and 10 percent. *ERCOFTAC Best Practice Guidelines - Industrial computational fluid dynamics of single phase flows* (2000) states that a turbulent intensity up to 30 % can

be used for atmospheric boundary layer flow.

4.2.3 Boundary conditions

The CFD simulations are performed in ANSYS CFX. All the simulation cases use the same numerical method and boundary conditions—the average static pressure on the outlet of 0 Pa. The domain is sized in line with guidelines from the Architectural Institute of Japan Tominaga et al. (2011). The $k-\omega$ SST turbulence model is used with an automatic wall function. The automatic wall function is explored in Chapter 3.14.8.

Firstly, a grid independence study was completed to evaluate the mesh quality, as explained in the previous chapter. Furthermore, after the mesh independence study was completed, the chosen mesh and domain size was used on the 3D CFD simulation. The chosen mesh is 1L from Table 4.2. As the length of the building is different between the 2D geometry and 3D geometries, the first inflation layer height and face sizing had to be modified slightly to get the same y^+ as in section 4.1.

The domain size has the same building height dependence as in the 2D simulations, as seen in Figure 4.2. The following boundary conditions were used in all the 3D simulations as shown in Figure 4.2. Inlet was used on the wind entry surface "Inlet". The boundary condition Opening was used on the "Outlet" surface. For such a long downstream length the choice of either 'Opening' or 'Outlet' should give negligible results difference. Additionally, rough walls were used on the building surfaces and the ground to model snow roughness. The sand grain roughness K_s as mentioned in Chapter 3.14.6 is set to $K_s = 0.5$ mm as in Ferreira et al. (2019). Snow grains have a diameter between 0.1 mm and 0.5 mm. Lastly, the symmetry boundary condition was used on the three unmarked domain surfaces. The parapet is sized accordingly to recommendations from *Riktig utforming av parapetbeslag - SINTEF* (2021) with a width of 0.2m and extending a height of 0.5m over the roof(in full scale). The blockage ratio is between 0.8 - 2 % which is well below the recommendation of 3 % in Tominaga et al. (2011). All the simulation properties are displayed in Chapter 4.3.

The flow is compressible as is it modeled as "Air ideal gas", and density changes with temperature. The density ρ and dynamic viscosity μ is constant, and is respectively equal to 1.306 kg/m^3 and 1.81×10^{-5} Pa s. The flow is isothermal. This is a simplification that can be employed as the flow distance is so long the heat transfer is so rapid that the temperature can be regarded as constant.

A steady-state was run to reduce the computational cost, and what the flow properties values were at a steady-state was of most interesting to achieve the research target.

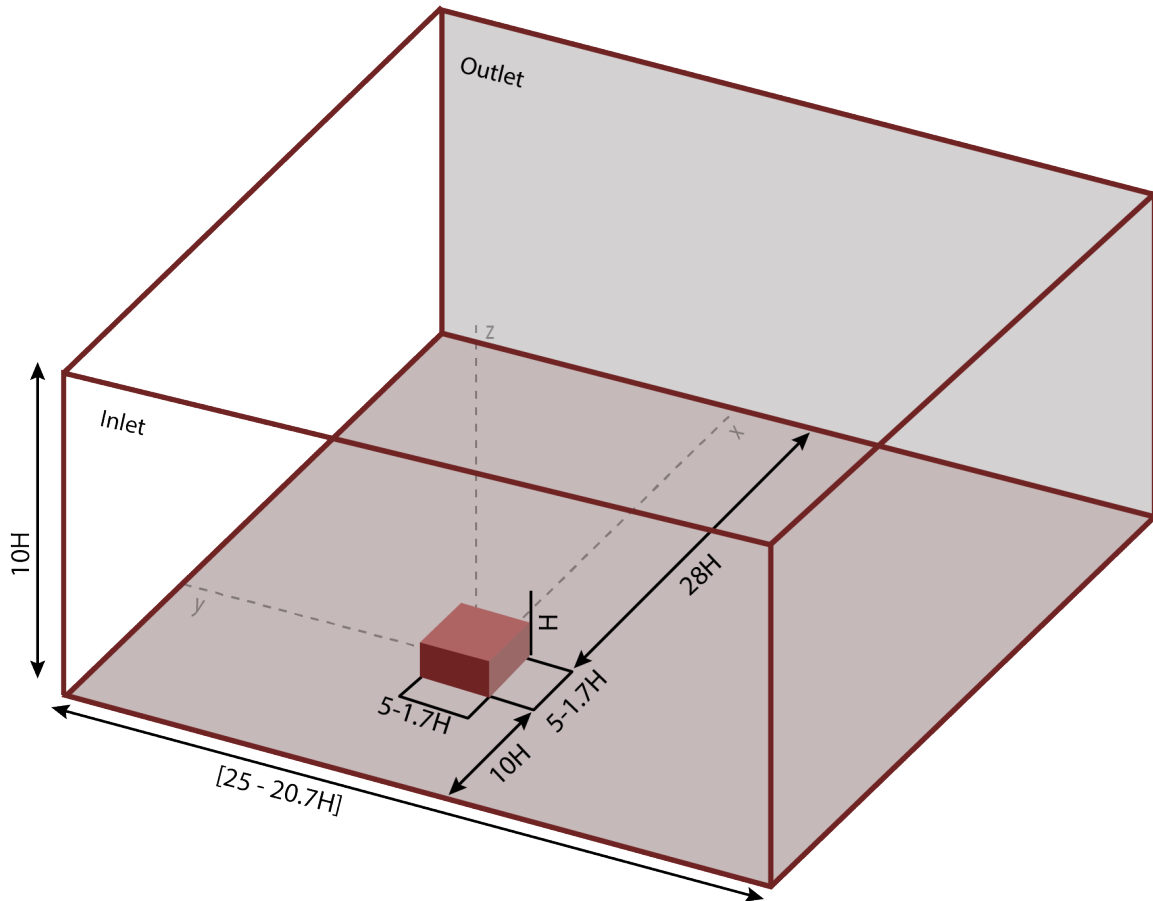


Figure 4.2: Domain size used in the CFD simulations. Origin is in the middle of the building in the XY -plane. Drawings are not to scale. Domain is sized accordingly to Tominaga et al. (2011).

Table 4.3: 3D CFD simulation properties

Building size ($L \times W \times H$)	$0.5 \times 0.5 \times (0.1, 0.2, 0.3)$ m
Parapet size ($W_p \times H_p$)	0.02×0.5 m
Mesh	1L (Table 4.2)
Scale	1:100
Analysis type	Steady-state
Flow type	Isothermal
Wind velocity	$u(z) = \text{Eq. 3.8}, v = w = 0$ m/s
U_{10}	11.1 m/s
α	0.18, 0.28
Air density, ρ_a	1.306 kg/m^3
Dynamic viscosity, μ	1.81×10^{-5} Pa s
Turbulence model	k- ω SST
Inlet turbulence intensity	10 %
K_s	0.5 mm (rough wall)
Blockage ratio	0.8-2 %
Inlet turbulence intensity	10 %
Outlet boundary condition	Opening
Walls	$u, v, w = 0$ (no-slip)
Symmetry	$\frac{\partial u}{\partial n} = \frac{\partial P}{\partial n} = 0$ m/s
Average relative outlet pressure	0 Pa
Reference pressure	1 atm

4.2.4 Flat roof simulations without a parapet

This chapter presents the 18 3D simulation cases run without a parapet. The case naming structure is: [No parapet(NP)]-[Height(H)]x[Width(W)][Length(L)]-[Wind direction(θ)]-[α].

Firstly, nine flat roof simulations cases were run without a parapet with $\alpha = 0.18$ as shown in Figure 4.4. Then nine more cases without a parapet, but with a different terrain roughness of $\alpha = 0.28$ as shown in Figure 4.5.

4.2.5 Flat roof simulations with a parapet

This chapter presents the 18 3D simulation cases run without a parapet. The case naming structure is [parapet(P)]-[Height(H)]x[Width(W)][Length(L)]-[Wind direction(θ)]-[α].

The geometries were designed equal to in Chapter 4.2.4 with the addition of using *Boolean Difference* to create the parapet. Then, more flat roof simulations were conducted on the same buildings with a parapet. The cases were run with $\alpha = 0.18$ as seen in Table 4.6, and with $\alpha = 0.28$ in Table 4.7.

Table 4.4: All simulation cases for flat roofs, $\alpha = 0.18$ without a parapet with different building heights and wind directions. "NP" - No parapet

Case	Height [m]	Wind direction [θ]	α
NP-05x05x01-0°-0.18	10	0	0.18
NP-05x05x02-0°-0.18	20	0	0.18
NP-05x05x03-0°-0.18	30	0	0.18
NP-05x05x01-22.5°-0.18	10	22.5	0.18
NP-05x05x02-22.5°-0.18	20	22.5	0.18
NP-05x05x03-22.5°-0.18	30	22.5	0.18
NP-05x05x01-45°-0.18	10	45	0.18
NP-05x05x02-45°-0.18	20	45	0.18
NP-05x05x03-45°-0.18	30	45	0.18

Table 4.5: All simulation cases for flat roofs, $\alpha = 0.28$ without a parapet with different building heights and wind directions. "NP" - No parapet

Case	Height [m]	Wind direction [θ]	α
NP-05x05x01-0°-0.28	10	0	0.28
NP-05x05x02-0°-0.28	20	0	0.28
NP-05x05x03-0°-0.28	30	0	0.28
NP-05x05x01-22.5°-0.28	10	22.5	0.28
NP-05x05x02-22.5°-0.28	20	22.5	0.28
NP-05x05x03-22.5°-0.28	30	22.5	0.28
NP-05x05x01-45°-0.28	10	45	0.28
NP-05x05x02-45°-0.28	20	45	0.28
NP-05x05x03-45°-0.28	30	45	0.28

Table 4.6: All simulation cases for flat roofs with parapet, $\alpha = 0.18$ with a parapet with different building heights and wind directions. "P" - parapet.

Case	Height [m]	Wind direction [θ]	α
P-05x05x01-0°-0.18	10	0	0.18
P-05x05x02-0°-0.18	20	0	0.18
P-05x05x03-0°-0.18	30	0	0.18
P-05x05x01-22.5°-0.18	10	22.5	0.18
P-05x05x02-22.5°-0.18	20	22.5	0.18
P-05x05x03-22.5°-0.18	30	22.5	0.18
P-05x05x01-45°-0.18	10	45	0.18
P-05x05x02-45°-0.18	20	45	0.18
P-05x05x03-45°-0.18	30	45	0.18

Table 4.7: All simulation cases for flat roofs with parapet, $\alpha = 0.28$ with a parapet with different building heights and wind directions. "P" - parapet.

Case	Height [m]	Wind direction [θ]	α
P-05x05x01-0°-0.28	10	0	0.28
P-05x05x02-0°-0.28	20	0	0.28
P-05x05x03-0°-0.28	30	0	0.28
P-05x05x01-22.5°-0.28	10	22.5	0.28
P-05x05x02-22.5°-0.28	20	22.5	0.28
P-05x05x03-22.5°-0.28	30	22.5	0.28
P-05x05x01-45°-0.28	10	45	0.28
P-05x05x02-45°-0.28	20	45	0.28
P-05x05x03-45°-0.28	30	45	0.28

After the CFD simulations were completed, they were opened in CFD-post and analyzed. The friction velocities u_* in each grid cell of the roof were exported together with the position of the centroid of the cells and the area of cells as a .csv file. The dataset was then further analyzed in Python. The median friction velocity was calculated on each roof. One friction velocity value was calculated for each roof as the objective of this master thesis is to implement the expression for friction velocity into a future more accurate snow model while still streamlining the calculation process for the engineers. This one value was a median to reduce the significance of extreme values on this one value.

4.2.6 Filtering (Modified Z-method)

As in any distribution, there exist outliers that give numerical errors, as described in Chapter 3.14.11. As RANS does not handle flow separation as well as LES and DNS, a filtration method might mitigate some of the numerical error caused by this. The average can be significantly affected by a single outlier. An algorithm should be established to detect and remove outliers without physical meaning. This thesis aims to find one representative value for each roof.

The use of Z-scores is a way to calculate how many standard deviations a statistic is from the average value. But they are highly dependent on sample size. The modified Z-method is a method to label outliers suggested in iglewicz1993. It uses the median instead of average and the mean absolute deviation (MAD) instead of standard deviation (SD). (Iglewicz and Hoaglin, 1997) MAD is calculated in Equation 4.7.

$$MAD = \text{median}_i |u_{*i} - \tilde{u}_*| \quad (4.7)$$

where \tilde{u}_* is the median of u_* , u_{*i} is the friction velocity stored inside each cell.

Furthermore, M_i is calculated from Equation 4.8 as compared with D .

$$M_i = \frac{0.6745(u_{*i} - \tilde{x})}{MAD} \quad (4.8)$$

Observations will be labeled as outliers if $M_i > D$ where $D = 3.5$ as recommended in Iglewicz and Hoaglin (1997). Outliers are deleted from the dataset before calculating the median friction velocity.

4.2.7 Scaling parameters

To achieve a completely similar solution between the 1:100 and full-scale simulations, the 1:100 scale needs to fulfill some requirements (Qiang et al., 2019). This is further explained in Chapter 3.14.10.

Full-scale complimentary simulations were completed at a similar grid resolution as the 1:100 scale simulation. The geometry was scaled to 1:1, and all streamlines were equally shaped. To achieve dynamic similarity while assuming the same kinematic viscosity then the 1:1 simulations was run with $U_{10} = 0.111$ m/s and $K_s = 40$ mm. Then the resulting friction velocities were multiplied by 100.

5. Results

This chapter will show the CFD simulation results obtained from the grid independence study, the critical mesh metrics near the roof, normalized friction velocity in the 3D simulations, and the effect of different parameters on the friction velocity.

5.1 2D Grid independency study

Firstly, the results from the grid independence study will be presented.

The solution of the different meshes from Table 4.1 is shown in Figure 5.1. The largest discrepancies occur at the beginning and end of the roof ($x/H = 0$ and $x/H = 2$) as this is where the recirculation zones are, and here the Irwin probes cannot accurately determine the shear stress. The distribution of the Irwin probes on the roof in ferreira2019 is shown in Figure 2.1. The chosen mesh was SST yplus: 65-25 | BL, as the solution using this mesh is closest to the wind tunnel studies.

Thereafter, a comparison of the accuracy of the solution depending on the domain size is shown in Figure 5.2.

5.1.1 Mesh details

The mesh structure chosen ("SST yplus 65-25 | BL") is shown in 5.3. The wind direction is in the positive x-direction. The inflation layers are the thin cells near the domain walls.

The cells close to the roof are magnified as they are critical for the solutions' convergence and are often the cells of the worst quality. A close up section plane view of skewness, orthogonal quality and aspect ratio is respectively shown in Figure 5.4, 5.5 and 5.6.

5.2 3D simulations

The following section displays the results of the cases mentioned in Tables 4.4, 4.5, 4.6, and 4.7. The main findings are in Tables 5.1,5.2 and 5.4. All the plots u_* presented in

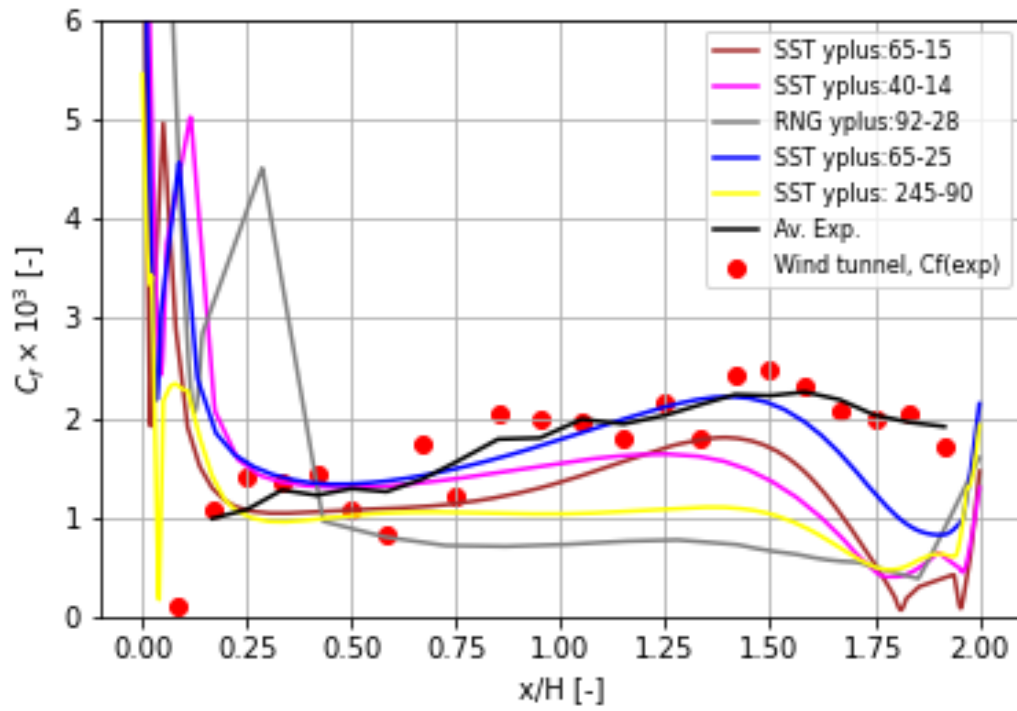
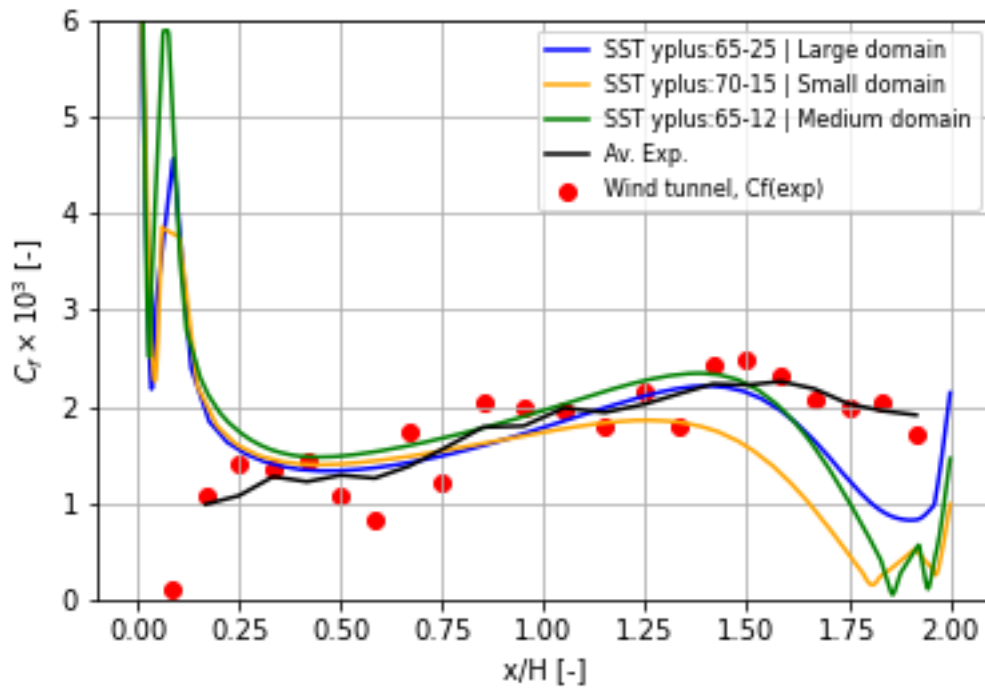


Figure 5.1: Grid independence study

Figure 5.2: The chosen mesh's (Blue plot) mesh dependency



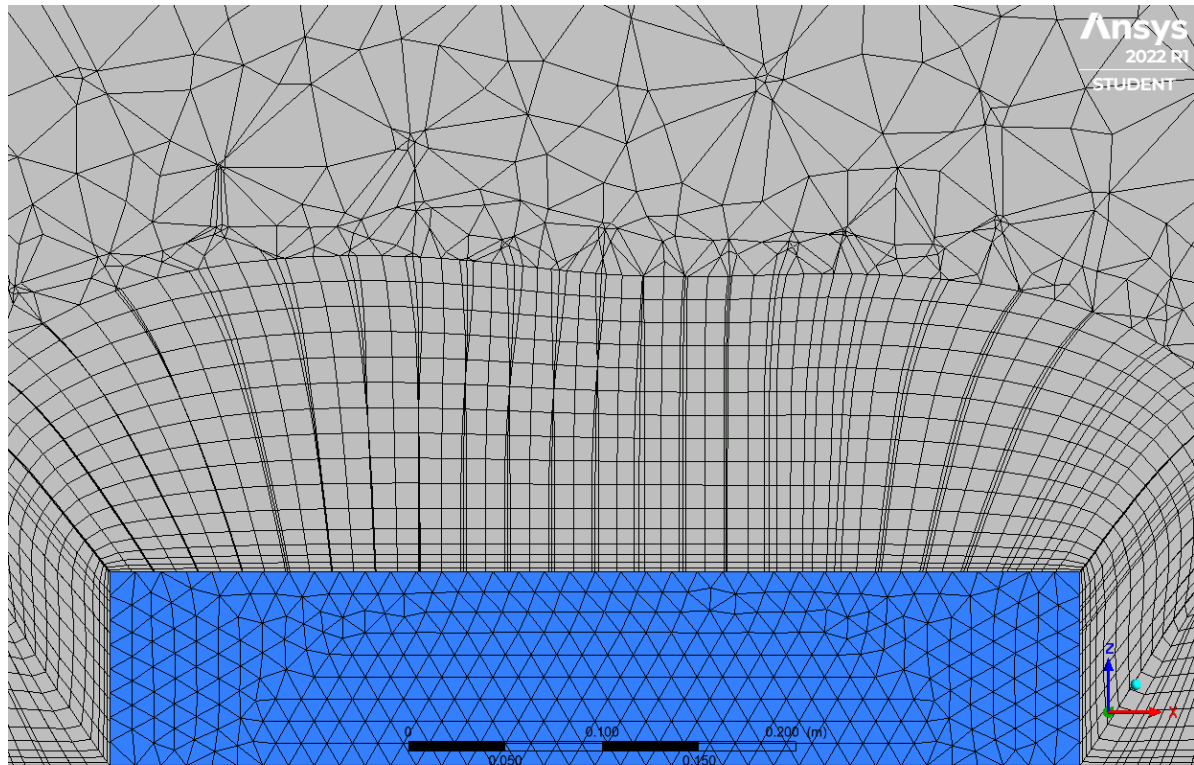


Figure 5.3: Section plane view of the mesh close to the roof in the XZ-plane. The face sizing is shown on the (blue) building.

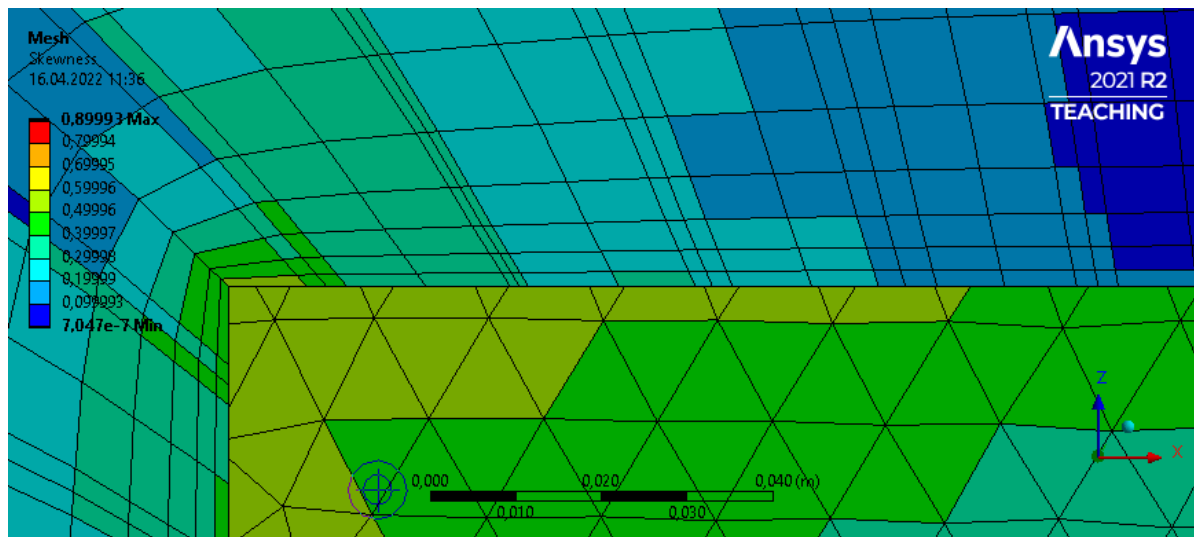


Figure 5.4: Skewness quality of each cell close to the roof. The larger cells in the background are face sizing cells.

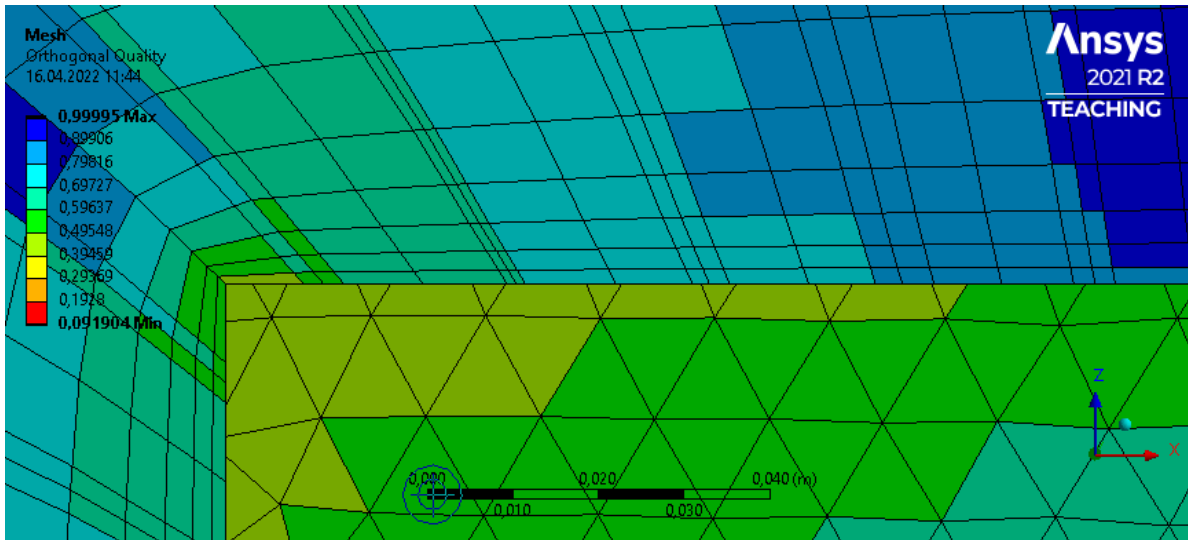


Figure 5.5: Orthogonal quality of each cell close to the roof. The larger cells in the background are face sizing cells.

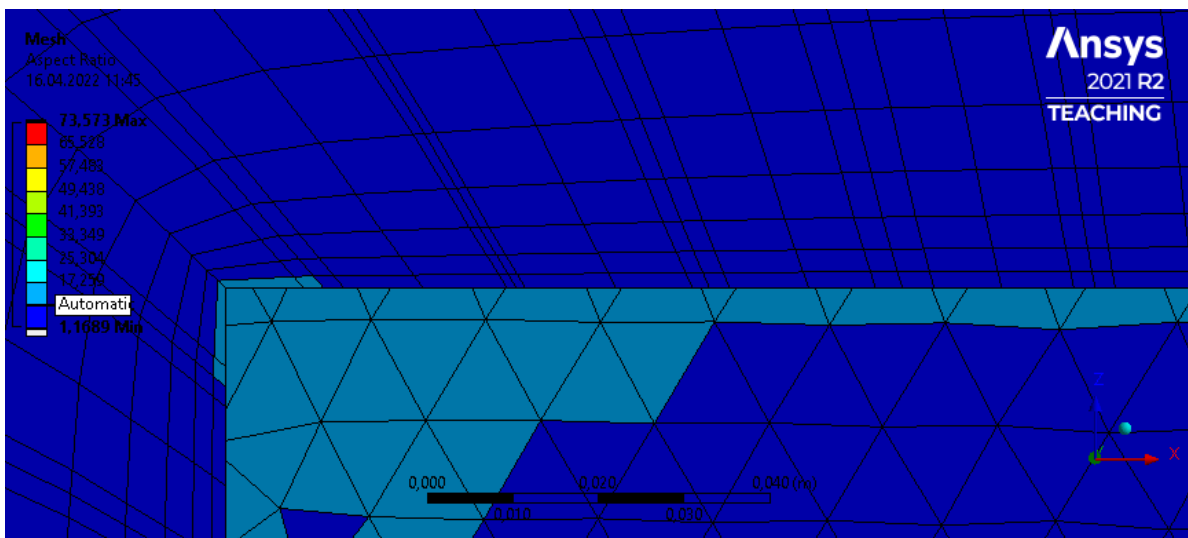


Figure 5.6: Close view of aspect ratio in each cell close to the roof. The larger cells in the background are face sizing cells.

this master thesis are the median filtered friction velocity. The outliers labeled by the modified Z-method are removed from the dataset before the median is calculated.

Table 5.1 contains a plot of the least squares linear fit of u_*/U_{10} obtained from the simulations in Figures 5.8 and 5.10. The roofs with and without parapets are bundled together as the median friction velocity is almost identical. The line allows for calculation of u_*/U_{10} based on the roof height H .

Table 5.1: Least squares linear fit of the different simulation cases for $\alpha = 0.18$ and 0.28 as a function of H . The cases with or without parapet are bundled together.

Case	$u_*(H)/U_{10}$
NP/P-05x05x0H-0- α -0.18	$= 0.024 + 0.00037H$
NP/P-05x05x0H-0- α -0.28	$= 0.026 + 0.00035H$
NP/P-05x05x0H-22- α -0.18	$= 0.051 + 0.00072H$
NP/P-05x05x0H-22- α -0.28	$= 0.049 + 0.00089H$
NP/P-05x05x0H-45- α -0.18	$= 0.055 + 0.00077H$
NP/P-05x05x0H-45- α -0.28	$= 0.050 + 0.0011H$

Table 5.2 contains the fitted filtered median using the modified Z-method.

Table 5.2: Fitted filtered median u_*/U_H values for the three wind directions studied displayed as dashed lines in Figures 5.8 and 5.10.

Wind direction, θ	α	u_*/U_H	α	u_*/U_H
0°	0.18	0.027	0.28	0.028
22°	0.18	0.058	0.28	0.056
45°	0.18	0.062	0.28	0.061

5.2.1 Simulations with terrain roughness $\alpha = 0.18$

The normalized median friction velocities are displayed in Figures 5.7 and 5.8.

Firstly, Figure 5.7 is a plot of the filtered median friction velocity $u_*(H)$ where H is the height of building roof normalized by the mean wind speed at 10 meters height. The plot contains all the 18 cases combined from Table 4.4 and Table 4.6. It shows that the friction velocity increases wind direction angle θ . Wind from 0° gives the minimum u_* values, and wind from 45° gives the maximum values. As the roof has four symmetry axes $\min u_* : (n)90^\circ$, and $\max u : (n+1)45^\circ$ where $n = [0, 1, \dots, 7]$. Furthermore, friction velocity on the building increases with height. The figure shows that the median friction velocity is almost identical for a roof with or without parapet. u_*/U_{10} for each wind direction and building height independent if the roof has a parapet or not is fitted with a linear approximation.

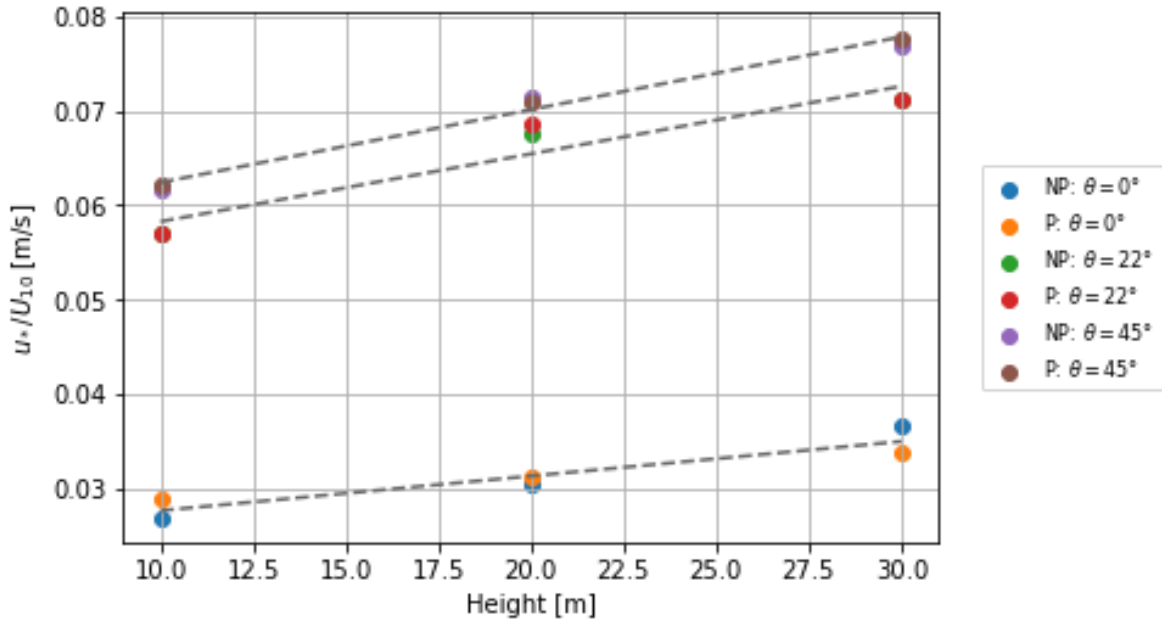


Figure 5.7: u_* as a function of roof height H where $\alpha = 0.18$. "P" - Parapet, and "NP" - No parapet. Some values lie behind other values and show as one. Fitted with the line in Table 5.1

Similarly, Figure 5.8 shows that u_*/U_H varies widely with wind direction θ . u_*/U_H ranges between (0.027 , 0.064) depending on the wind direction.

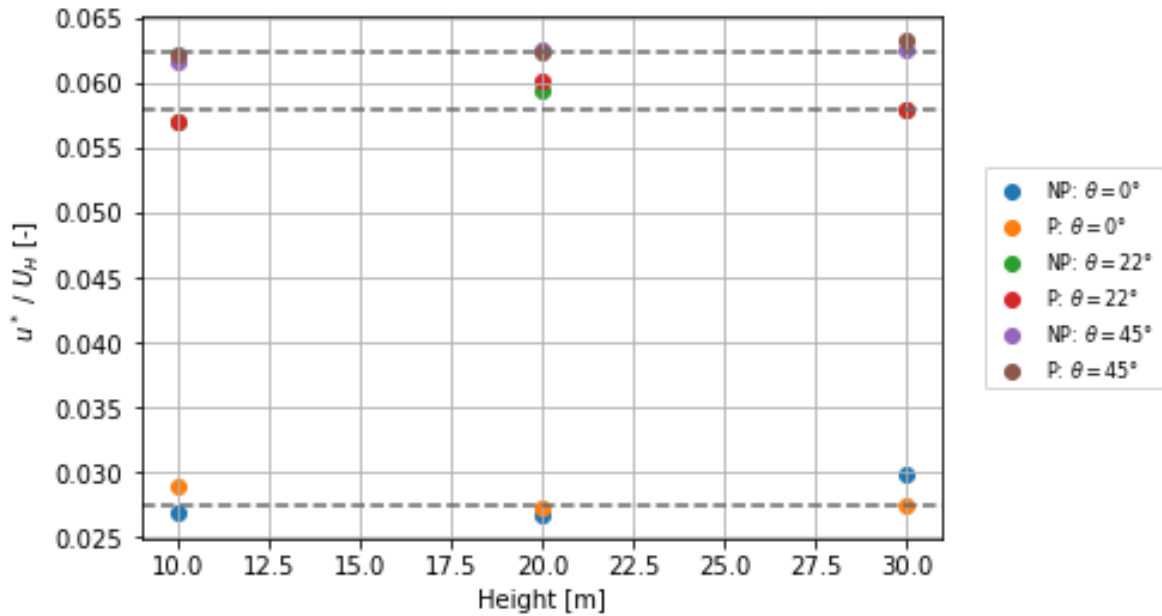


Figure 5.8: u_* normalized by the roof wind velocity U_H at each roof height where $\alpha = 0.18$. "P" - Parapet, and "NP" - No parapet. Some values lie behind other values and show as one. Fitted with the line in Table 5.1

5.2.2 Simulations with terrain roughness $\alpha = 0.28$

Figure 5.9 is the same plot as Figure 5.7 with $\alpha = 0.28$ instead. Each point is a CFD simulation case from Table 4.5 and Table 4.7. The friction velocity increases with building height. Furthermore, as the wind direction angle θ increases then the friction velocity increases. u_*/u_{10} is approximated by a linear function.

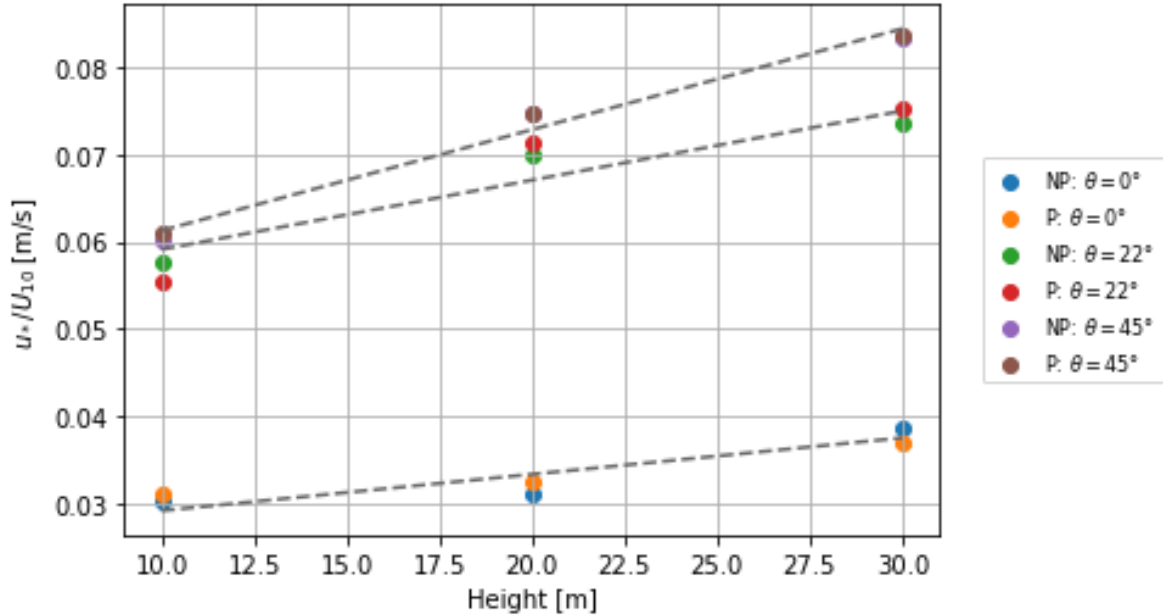


Figure 5.9: u_* as a function of roof height H where $\alpha = 0.28$. "P" - Parapet, and "NP" - No parapet. Some values lie behind other values and show as one.

In Figure 5.10 the friction velocity u_* is normalized by the mean wind speed at the roof height U_H . As mentioned in 3 the research question is to find an expression for u_*/U_H . Figure 5.10 suggests that u_*/U_H varies widely and is in the range (0.028 , 0.062) depending on the wind direction.

Furthermore, the local effects of a parapet or no parapet are displayed by the use of streamlines in Table 5.3. 6500 streamline points are used in all figures. The vortex on the leeward zone of the building is reattaching. The airflow separates from the building surface at the windward wall of the building. The separation vortex is measurable with the displayed scale. In case NP-05x05x01-00° the separation bubble is circa 0.2 m(20 m long), while in Figure P-05x05x01-00° it is circa 0.35 m(35 m long).

Contour plots of the local friction velocities on the roofs are displayed in Table 5.4. All the plots uses the same value range for u_* from 0 m/s to 1.3 m/s and number of contours as seen in Figure 5.11. Also, the same wind profile is used. The dark blue area has a $u_* \approx 0$ m/s, and the dark red area has $u_* = 1.3$ m/s. As seen in Table 5.4, the friction velocity distribution on the different roofs varies widely.

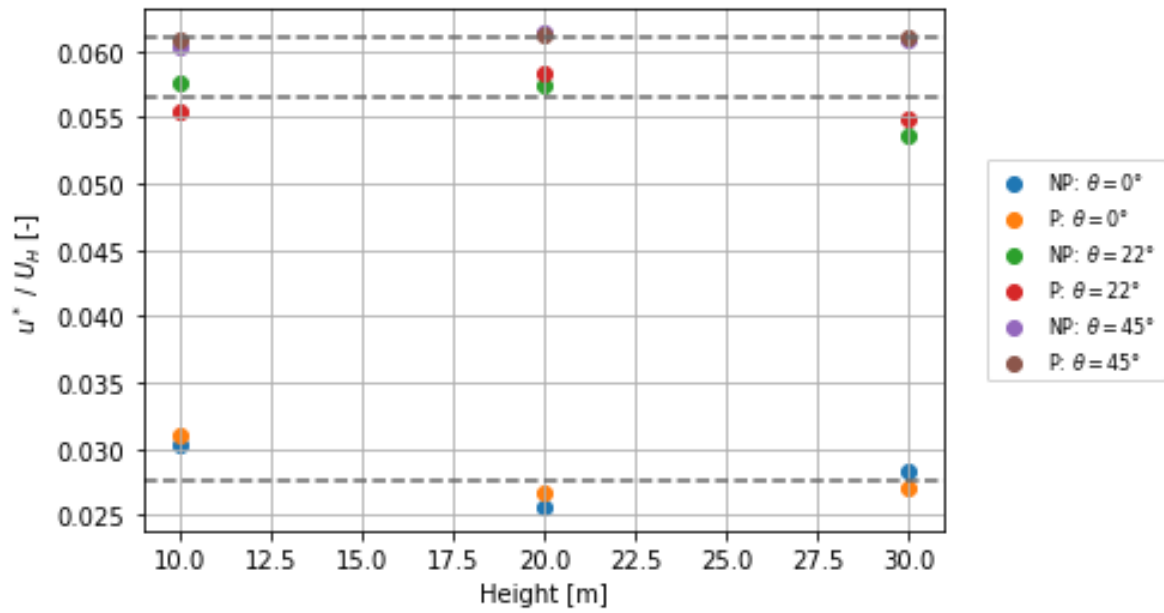


Figure 5.10: u_* normalized by the roof wind velocity U_H at each roof height where $\alpha = 0.28$. "P" - Parapet, and "NP" - No parapet. Some values lie behind other values and show as one.

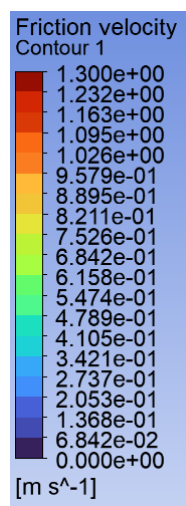


Figure 5.11: Value range for the contours plot

Table 5.3: Surface streamlines on the roofs for $\theta = 0^\circ$ and $\alpha = 0.28$. Wind moves from left to right on each plot. No parapet("NP") cases on the left column and parapet("P") cases on the right column.

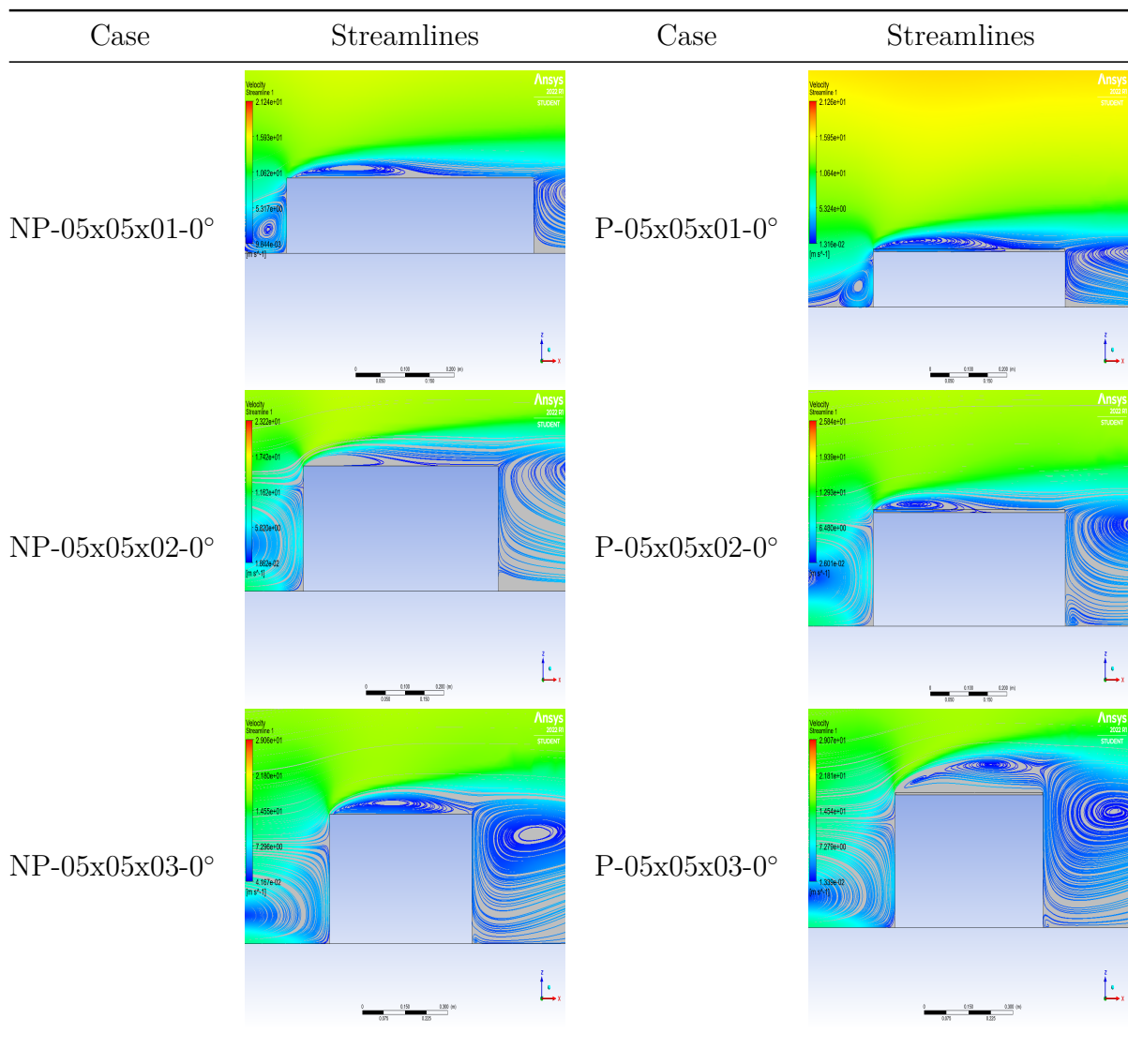
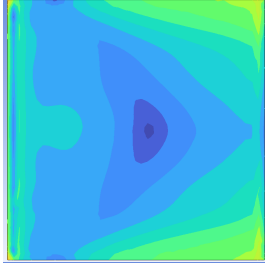
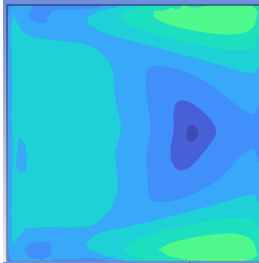
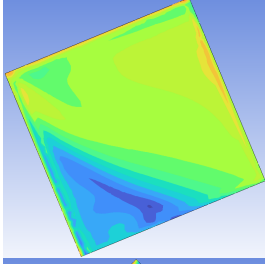
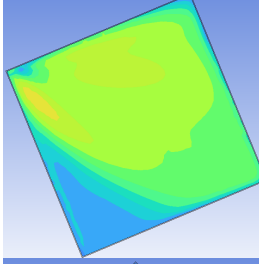
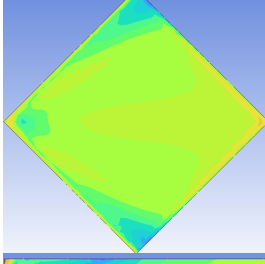
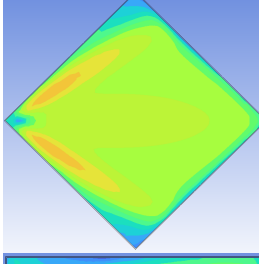
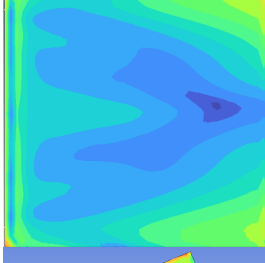
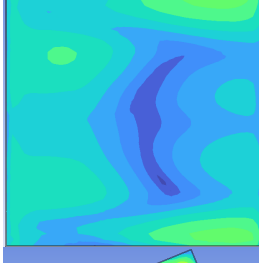
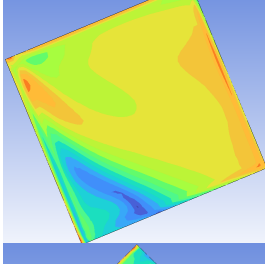
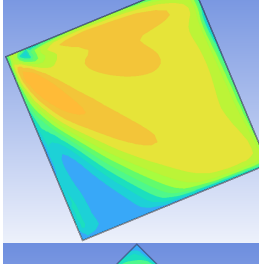
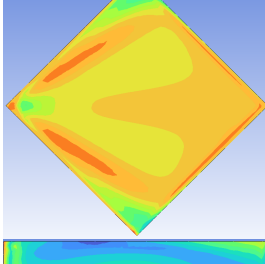
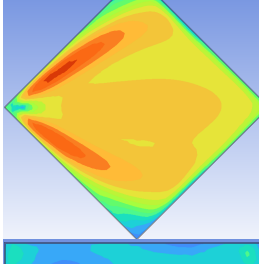
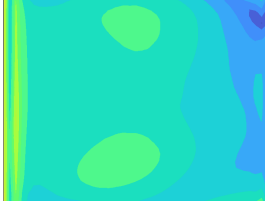
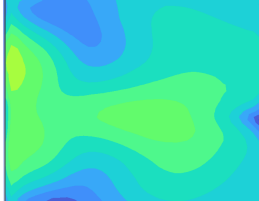
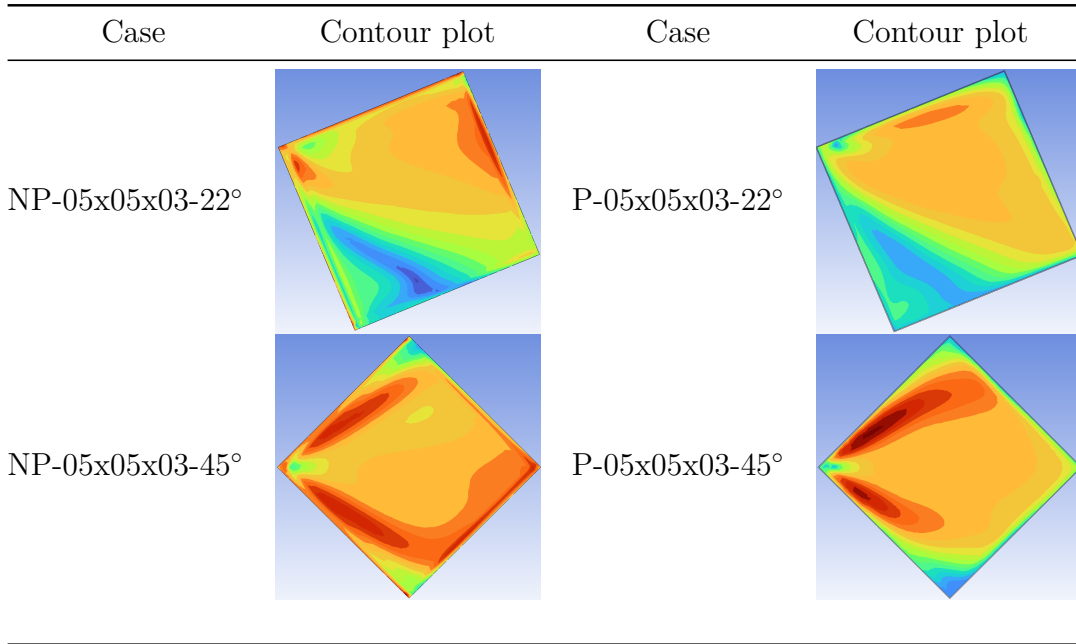


Table 5.4: Contour plots of friction velocities on the roofs for $\alpha = 0.28$. Wind moves from left to right on each plot. No parapet ("NP") cases on the left column and parapet ("P") cases on the right column. The values are scaled according to Figure 5.11.

Case	Contour plot	Case	Contour plot
NP-05x05x01-0°		P-05x05x01-0°	
NP-05x05x01-22°		P-05x05x01-22°	
NP-05x05x01-45°		P-05x05x01-45°	
NP-05x05x02-0°		P-05x05x02-0°	
NP-05x05x02-22°		P-05x05x02-22°	
NP-05x05x02-45°		P-05x05x02-45°	
NP-05x05x03-0°		P-05x05x03-0°	



5.2.3 3D simulation verification

Numerous checks were used to verify the accuracy of the simulations. The following verifications were only conducted with $\alpha = 0.28$, but is valid for $\alpha = 0.18$ too.

Firstly, in Figure 5.12 the 1:100 simulations were compared with the full scale simulations. The two simulation types have complete similarity. The 1:100 scaled simulation had $U_{10} = 11.1$ m/s. Meanwhile, the full scale simulation had $U_{10} = 0.111$ m/s. The difference increases for the non-zero wind directions. The mean difference for all wind directions between u_*/U_H for full scale and 1:100 is 2.4 %.

Secondly, simulations for different wind direction for the building at 10 meters height was run with $U_{10} = 22$ m/s as labeled with as simply "NP" in Figure 5.13 . The simulation was remeshed to obtain the same y^+ value. They were compared with the u_* obtained from the original 3D simulations with $U_{10} = 11.1$ m/s and then multiplied by $(22/11.1)$. The difference is shown in Figure 5.13. Again, the percentage difference increases for non-zero wind directions. The mean percentage difference is 7.2%.

Thirdly, U_*/U_H from different wind direction dependency on K_s for the 10 meter high building without a parapet is shown in Figure 5.14. The percentage difference increases with non-zero wind directions. The mean percentage difference between solutions with $K_s = 0.5\text{mm}$ and $K_s = 0.125\text{mm}$ is 10.8 %.

U_*/U_H from different wind direction dependency on the turbulence intensity for the 10-meter high building without a parapet is shown in 5.15. The mean percentage difference between the two turbulence intensities is 8.1%.

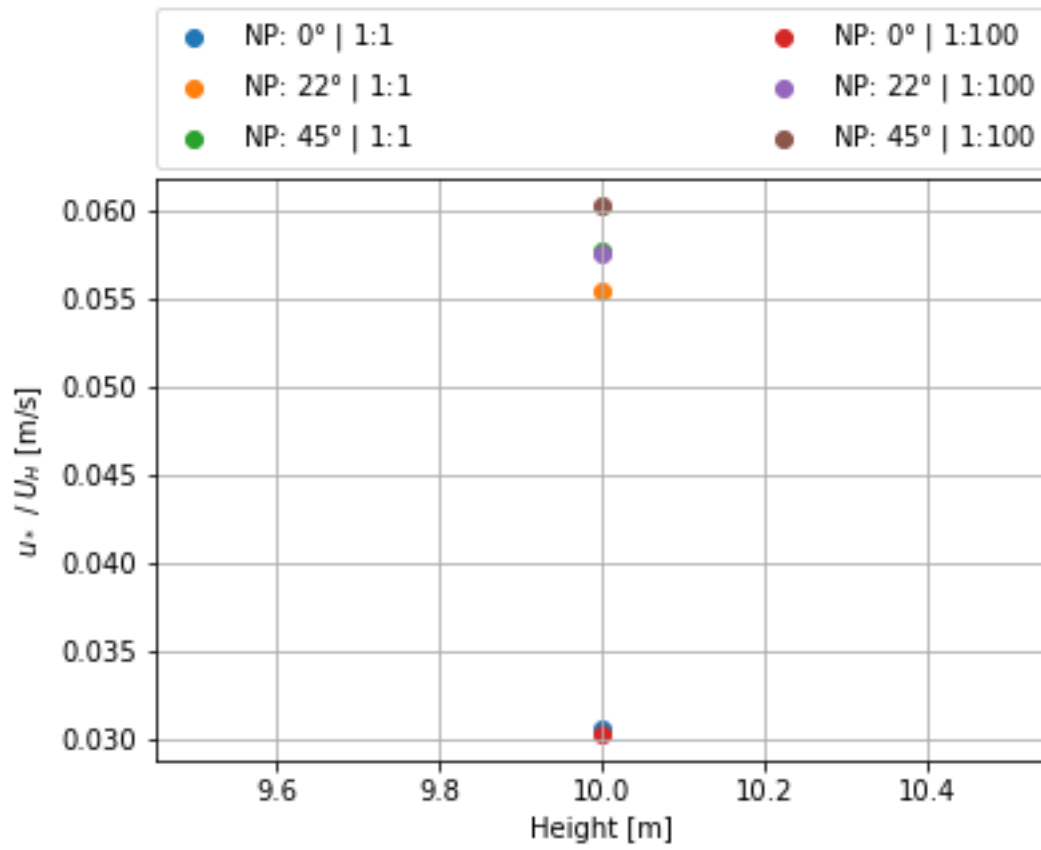


Figure 5.12: Difference in U_* / U_H between 1:100 and full scale simulation for the 10 meter high building without a parapet. NP: 45° | 1:1 lies behind NP: 22° | 1:100 NP: 45°

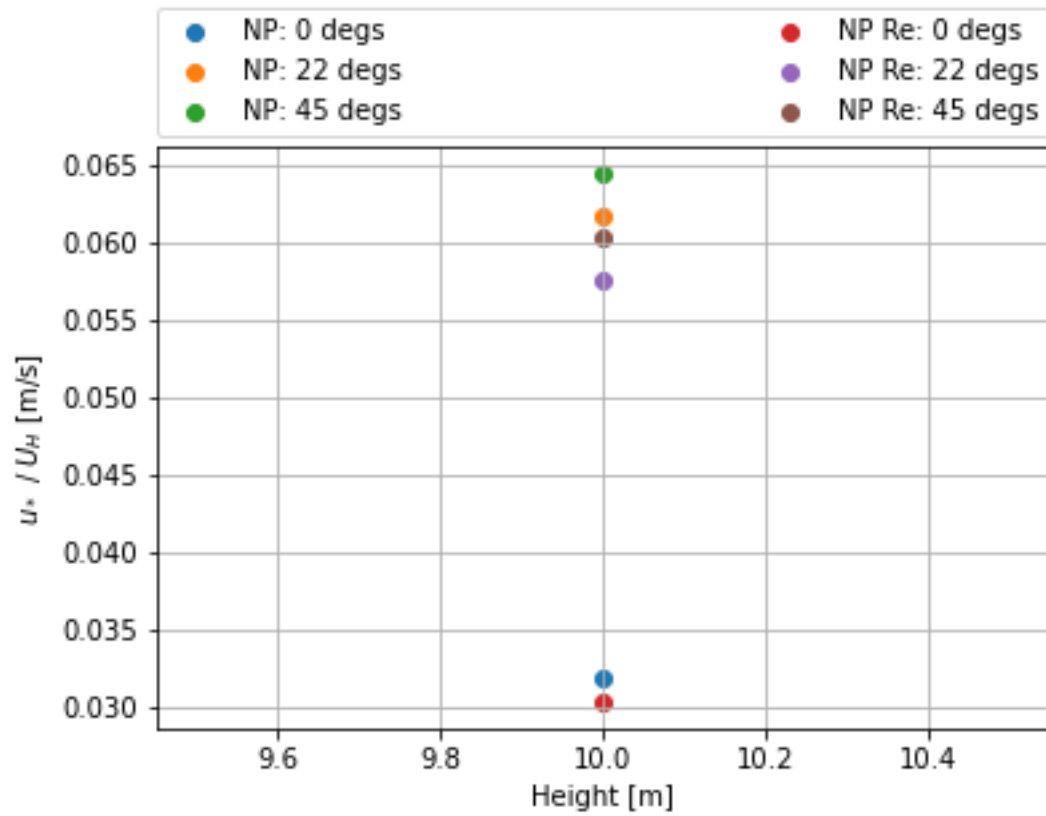


Figure 5.13: Reynolds dependency verification of U_* / U_H for different wind directions for the 10 meter high building without a parapet

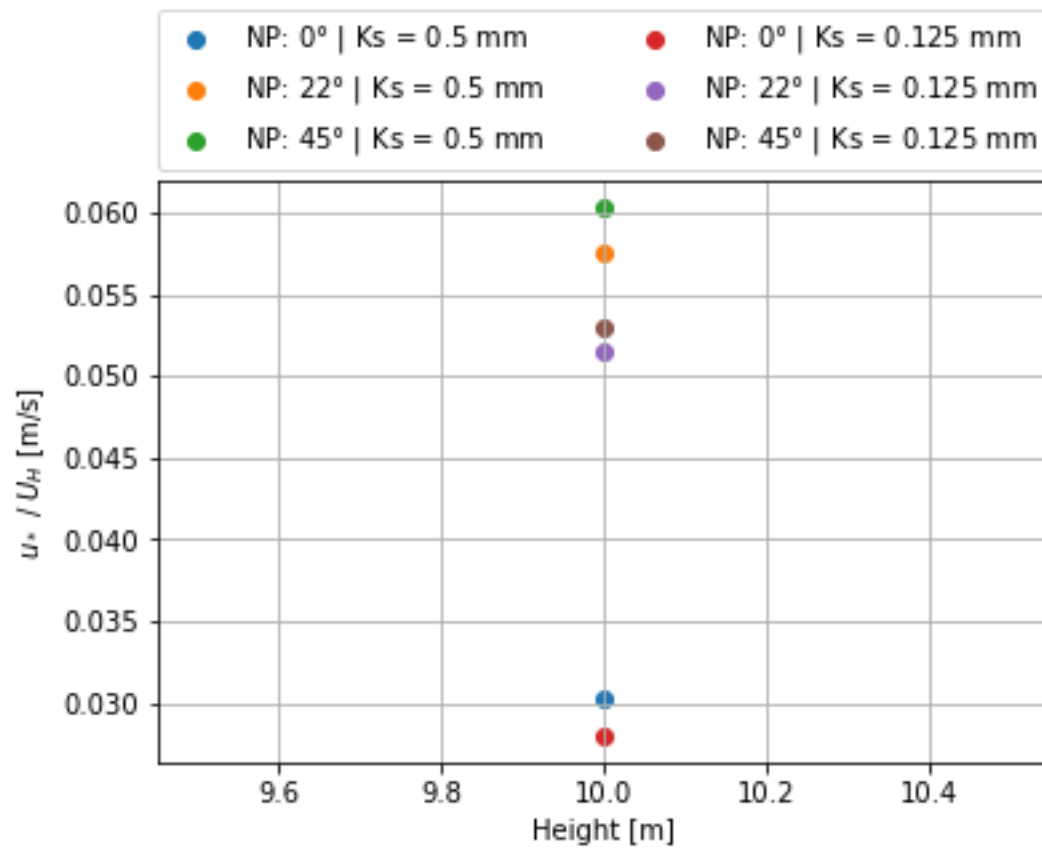


Figure 5.14: U_* / U_H dependency on K_s

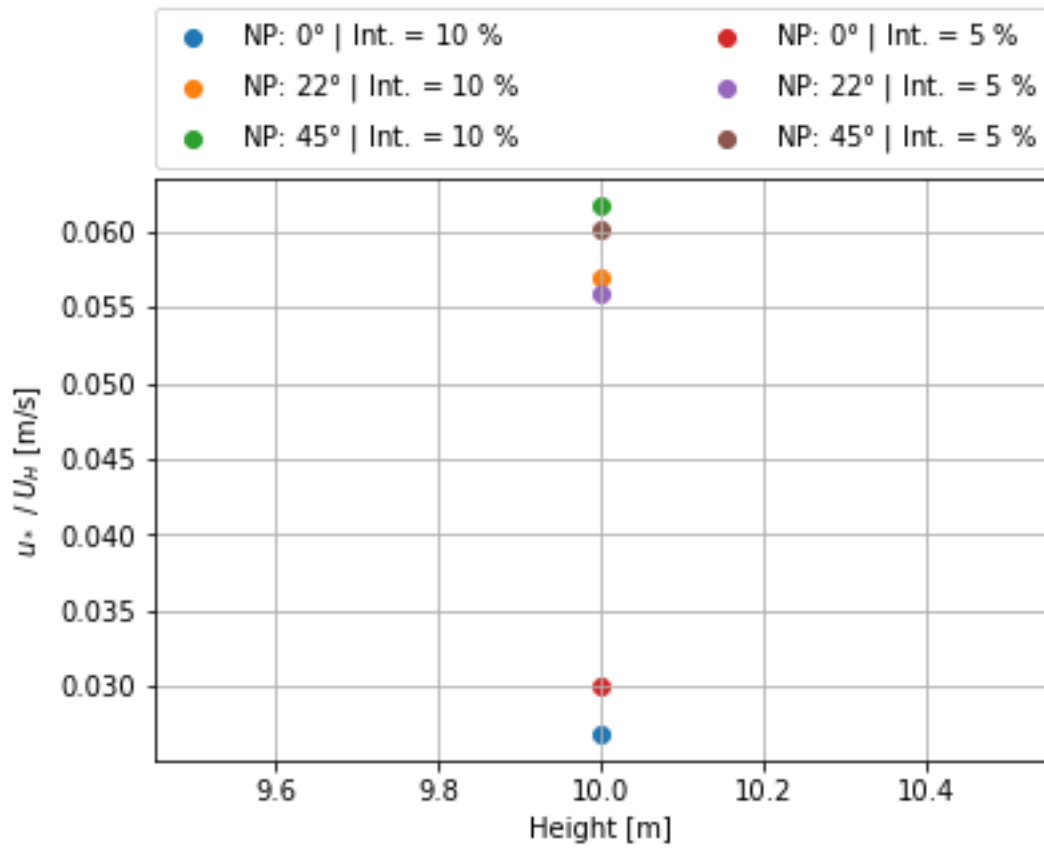


Figure 5.15: U_* / U_H dependency on inlet turbulence intensity

5.2.4 Outliers

As explained in Chapter 4 outliers were removed by the modified Z-method. The modified Z-method removed between 20 % for NP-05x05x02x45° and 0 % for NP-05x05x02x0° of the u_* 's from the dataset. The respective difference between the filtered and original median value was 4.1% and 0%. In general, more data points were removed when $\theta = 0^\circ$.

6. Discussion

To iterate the research question to be answered in this master thesis is to quantify the normalized friction velocity on flat roofs with or without a parapet. The method of study in these investigations were 3D RANS single-phase CFD simulations on different height flat roofs from various wind directions. The main findings are presented in Figures 5.7, 5.8, 5.9 and 5.10, and Tables 5.2 and 5.1.

6.1 Mesh

To verify the mesh used in the 3D simulation solutions, a grid independence study was first conducted. The best-performing mesh which met the requirements was then slightly modified and used with the 3D simulations.

6.1.1 Grid independence study

The grid independence study was a 2D CFD simulation with wind approaching normal to a side wall ($= 0^\circ$) in 1:25 scale based on wind measurements from Ferreira et al. (2019). Based on observations in Figure 5.1 the $k-\omega$ SST turbulence model shows the best approximation to the wind tunnel studies. This result is expected as this turbulence model performs well with advent pressure gradients and separation, which is behavior-bound to flow around a building. The $k-\epsilon$ turbulence model showed not as promising results in Ferreira et al. (2019) as the SST turbulence model because it does not handle advent pressure gradients well. Ntinis et al. (2018) claim that the RNG $k-\epsilon$ turbulence model is the best model to approximate velocity around a flat roof building. The RNG $k-\epsilon$ mesh displayed in Figure 5.1 used the same mesh and element sizing as in the SST yplus 65-25 but showed highly different results. A grid that shows independence characteristics in one turbulence model will not necessarily indicate it in another turbulence model, as mentioned in Chapter 3.14.11. To further investigate the actual accuracy of the RNG $k-\epsilon$ turbulence model, a new grid refinement study has to be completed, but it was decided not to be investigated as the SST yplus 65-25 (case 1L) mesh provided sufficient accuracy. SST yplus 65-25 had a solution which was almost similar to a

solution in Ferreira et al. (2019) using $y^+ = 7$, and the mesh resolution therefore most likely dependent of the solution. A grid independent solution is achieved.

Most of the mesh parameters were set as the default values in CFX. However, the following parameters were changed; The face sizing had the element size of 0.015 m ($L/40$). It was used on the building faces, and the ground to more easily control the cell quality of the inflation layer. As seen in Figure 5.2 there are large discrepancies between the wind tunnel study and CFD simulations for $x/H \in (0.15, 0.25)$ and $x/H \in (1.55, 1.85)$. These are mainly because the Irwin probes shown in Figure 2.1 are not able to measure the shear stress close to the building edges. The smaller the face sizing, the smaller the discrepancies between the wind tunnel study and the CFD simulations. A reduction of face sizing impacts the difference minimally between CFD and wind tunnel experiments at $x/H \in (1.55, 1.85)$. Face sizing smaller than 0.015 m increases the computational time by several hundred percent, and therefore it was not set equal to 0.010 m. The face sizing of 0.010 provided a better solution for the flow separation at the beginning of the roof. The chosen face sizing is a compromise between the time and computational power available.

As mentioned in Chapter 3.14.7, the resolution of the gradients near the walls is essential for a reliable solution. Therefore fine cells of high quality are needed there. The first layer inflation height was calculated by inserting a target $y^+ = 40$ into the equations in Chapter 4.1 to calculate the first inflation layer height. The number of layers N was set to $N = 16$. The maximum growth rate G_{max} in the inflation layers to match the boundary layer thickness was $G_{max} = 1.48$. $G < 1.30$ are recommended from ansysreference, Franke2007 to retain the truncation error. These values are based on the case studied, experience, geometry, and turbulence model and are not universal (Franke and Baklanov, 2007). Therefore the chosen growth rate was reduced to $G = 1.3$ which gave less discrepancies than $G = 1.2$ as seen in Figure 5.1. Both the first inflation layer heights of the ground and building were the same to ensure a smooth transition between ground and building inflation layer cells. Otherwise, the cells were highly skewed, which reduced cell quality in that transition area and affected the adjacent cells' quality.

The small and medium-sized domain solutions are close to the experimental solution at the beginning of the roof. Still, there are more significant discrepancies in the latter part of the roof than the large domain size. Furthermore, the large domain was chosen as only that domain size showed similar results to the CFD simulations and wind tunnel study in Ferreira et al. (2019).

Thereafter, the cell quality of the created mesh needs to be investigated to ensure the mesh is adequately set up to enable a converged solution, as mentioned in Chapter 3.14.7 and 3.14.5. The area closest to the structure's roof is the most important to investigate

as this is where the shear stress is outputted from. Near the building, the mesh metrics will be the worst in the whole domain as the mesh method has to consider the building geometry. Skewness, orthogonality quality, volume transition, and aspect ratio are the relevant cell quality metrics to examine in this instance. Good quality in these metrics will increase the chance of a valid solution because convergence is satisfied.

Firstly, the skewness near the building roof in Figure 5.4 is, as expected, the worst in the cell closest to the windward edge. The value of this cell is equal to 0.5. The skewness scores increasingly better the closer to the middle of the roof and vary between 0.4 - 0.0. The large majority of the cells are well below the recommended skewness range presented in Chapter 3.14.7.

Secondly, the orthogonal quality is recommended to be not higher than 0.1 in all cells, as mentioned in Chapter 3.14.7. As observed in Figure 5.5 similarly to in Figure 5.4 the worst scoring cells lie close to the windward edge of the roof. The worst scoring cell has an orthogonal quality of 0.4, which is satisfactory.

Thirdly, the volume transition between the inflation layer cells and the volumetric cells must be smooth. This smoothing is ensured through appropriate growth rate G choices and the number of layers N to ensure a sufficient last inflation layer thickness. A smooth transition can be performed by choosing a freestream cell size that provides a similar volume adjacent to the last inflation layer volume. By Chapter 3.14.7 the volume transition difference is recommended to be between 1-2. As seen in Figure 5.3, this is achieved. In addition, the cells should become progressively larger as they move away from the building to reduce computational expense during meshing while still achieving the desired volume transition difference.

Lastly, the aspect ratio is the highest in the cell closest to the edge, as seen in Figure 5.6. In Chapter 3.14.7 the aspect ratio can be in the order of 10^3 in the boundary layer and between 20-50 in the freestream area. These recommendations are achieved in this mesh.

The skewness, orthogonality quality, and aspect ratio depend on chosen face sizing, freestream element sizing, and height of the inflation layer in the author's experience. The appropriate face size can be determined by assuming a first layer height and then arranging the free stream mesh based on the observed volume transition difference. Face size naturally influences the aspect ratio of the inflation layer cells. In the author's experience, excessive face sizing degrades orthogonal and skewness cell quality, thereby increasing the possibility of a non-converged solution.

All the solutions provided in Figure 5.1 terminated after meeting the RMS residuals criteria equal to 1E-4. Additionally, the grid independence study and wind tunnel

experiments were consistent, indicating a converged solution is met. Also, all relevant cell metrics are within the recommended range. This is a strong indication that the mesh will provide converged solutions. (Franke and Baklanov, 2007)

6.1.2 Convergence in 3D simulations

As the 3D simulations additionally simulate wind approaching not normal to the wall surfaces, this effect on the convergence of the solution will be discussed in this Chapter. As referred to in Chapter 3.14.5, numerous criteria need to be fulfilled depending on the rigorousness of the user to achieve convergence. In 3D, the flow field around the building is different from 2D simulations (Peterka et al., 1985). Therefore, the convergence criterion needs to be carefully reexamined.

A well-defined minimum residual value to assume convergence is not defined in the literature as observed in Chapter 3.14.5. Therefore, the residuals can only be used as an indicator of convergence. The residuals in all simulation cases fall below the recommended value of $1E-4$ from Franke and Baklanov (2007) except in the eight cases N(P)-05x05x03-22-45° for both $\alpha = 0.18$ $\alpha = 0.28$ from Tables 4.4, 4.6, 4.5 and 4.7 respectively. In these cases the simulation ends after the predefined number of timesteps are completed. The maximum minimum RMS residuals achieved for these cases are $1.6E-4$ for the case P-05x05x03-45° . In Chapter 3.14.5 Versteeg and Malalasekera (2007) states that a termination criteria of 0.001 is widely used in industry applications. The reason for the increased RMS residuals might be because of the wind directions of $\theta = 22^\circ, 45^\circ$ provides an unsteady flow separation which might be a transient effect which complicates the steady-state analysis as seen in Chapter 3.14.2. The mean wind speed is larger at the higher roof heights which might amplify this effect.

Additionally, a study of the streamlines is recommended in Franke and Baklanov (2007) which can be completed by comparing Table 5.3 with Table 5.4. In both figures, there is a separation vortex near the sidewall on the windward side, as seen in 3.10. Additionally, a separation vortex exists on the roof of both figures, which is consistent with the theory. Also, the flow reattaches to the top of the building in both figures. If reattachment occurs depends on the building length-to-width ratio, height-to-length ratio, and upstream roughness, as mentioned in Peterka1985. Oke et al. (2017) states that roof reattachment occurs when $L/H > 1$, which is the case in all simulation cases. The height of the stagnation point lies between $2/3$ and $3/4$ of the building height and depends on the L/H building ratio (Peterka et al., 1985). This point seems to lie at around 0.8 of the building height in both figures due to the high L/H ratio.

Therefore, the behavior of the streamlines conforms to the established theory.

6.2 Friction velocity

The study of u^* is wanted such that value can be implemented in a larger future snow model, so the effect of wind on snow erosion is more accurately modeled. By knowing the snow erosion of a roof, a more accurate design snow load can be calculated. To simplify and assert one u^* value for a whole roof is wanted to continue making the snow load calculations easy to use while still increasing the accuracy of today's models.

As seen in Figure 5.7 and 5.9 u_* on the roof increases when the building height increases as the mean wind speed is larger at higher altitudes. u_* also increases when z_0 increases, then α increases, and the mean wind speed increases. This is consistent with the theory in Chapter 3. According to the figures in Chapter 5 they state that u_* varies widely depending on the wind direction.

Based on the results in Table 5.1 and 5.2 the friction velocity can be calculated if the user has access to meteorological data for U_{10} then Table 5.1 can be used to calculate the friction velocity. If the user has access to U_H values then 5.2 can be used. Wind is mostly only measured at 10 meters height. Based on the results in Table 5.2 fresh snow ($u_{*t} = 0.07m/s$) will start to erode at $u_H = 1.2$ m/s, and aged snow will start to erode at ($u_{*t} = 0.22m/s$) at circa $u_H = 4$ m/s.

Qiang et al. (2021) was uncertain if $u^*/U_H = 0.06$ for $\alpha = 0.12$ was terrain category independent. Table 5.2 show that the range u^*/U_H is almost similar depending on the terrain category. That largest difference is between $u^*/U_H = 0.058$ for $\alpha = 0.18$ and $u^*/U_H = 0.056$ for $\alpha = 0.28$. The percentage difference between the two u^*/U_H values are circa 3 %. The 3% can be regarded as a negligible difference as there is a total inaccuracy in all simulations, and the difference between α 's is much larger. u^*/U_H can based on the results be described as terrain category independent.

As u_* increases with building height, then taller buildings are more susceptible to erosion away from the roof compared to lower buildings. Also, $\theta \neq (0^\circ, 180^\circ)$ increases the friction velocity, and the susceptibility of snow eroding from the roof increases.

6.2.1 Friction velocity | Streamlines

This chapter studies the streamlines in relation to the shear stress on the roof.

As expected in Table 5.3 the length of the separation vortex at the roof with a parapet is significantly longer without a parapet. The lowest friction velocity occurs in the two figures when the flow reattaches to the mean flow again at the rear of the separation vortex, as observed in Liu et al. (2019). Buildings with a parapet will have a low friction area closer to the leeward side than the non-parapet equivalent as the amount of flow

separation is larger for parapets. This is consistent with the theory that a parapet increases separation. A larger parapet will further increase separation, but it was not studied in this master thesis.

6.2.2 Friction velocity | Contour plots

The chapter contains a discussion of the contour plots in Table 5.4. The theory presented in Chapter 3.13 is used the discussion.

Both NP-05x05x01-0° and P-05x05x01-0° have the lowest friction velocity right after the separation vortex stops where the flow reattaches, as observed in the previous chapter. The velocity inside the separation vortex is significantly lower inside it. NP-05x05x01-0° has a shorter spanning separation vortex than P-05x05x01-0°, and this area of low friction velocity will be closer to the windward side. This is consistent with the streamlines in Figures ?? and ??. Furthermore, as seen in NP-05x05x02-0°, the blue area of low friction velocity is further down the roof as the increased mean wind velocity at 20 meters increases separation. In NP-05x05x03-0°, the separation bubble spans the whole roof and interacts with the reattachment in the wake zone, creating a chaotic distribution. Therefore the friction velocity distribution seen in the preceding examples is not similar.

Common to all the simulations from wind direction $\theta = 0^\circ$ is that close to roof edges parallel to the wind direction, the friction velocity is the largest. Here vortices increase in size and TKE, which increases the friction velocity as they move down the leading edge of the roof. Here the chance of snow erosion is the largest. This is consistent with the theory in Chapter 3.2 that most erosion occurs at the end edge and sides of the building.

For $\theta = 22^\circ$ there is a large area with almost zero friction velocity close to one part of the roof. For the taller buildings this forms into a funnel with low shear which is significantly lower than the other sides of the roof. Here the roof is highly susceptible for snowdrifts forming.

Furthermore, common for all simulations from $\theta = 45^\circ$ is that when the approach flow hits the corner edge, the flow separates, creating a pair of strong standing vortices that increase energy and size and result in a substantial friction velocity. Thereafter the eddies dissipate and reduce in strength. One of these strong vortices is larger than the other one. The power of the vortices is larger with parapets than without parapets. These vortices produce two areas that are highly susceptible to snow erosion.

As seen in the table, the friction velocity increases in size with height and when θ increases. The higher friction velocity with increased height is because the mean wind speed increases with height. The reason for the higher friction velocity with increased

θ is because of the increased turbulence, which increases the turbulent shear stress, which increases the shear stress, which increases the friction velocity. The larger friction velocity in these examples increases the susceptibility of snow erosion.

The height of the parapets will hinder some of the eroding snow from being removed away from the roof. As mentioned in Chapter 3.2.1 snow will accumulate in the aerodynamic shade where the friction velocity is not exceeding the threshold value. With the wind from $\theta = 0^\circ$ for $H = 10\text{m}$, a larger low friction area is formed on the windward side of the parapet on the leeward building side than on the non-parapet equivalent. Therefore a parapet will increase the susceptibility of snow accumulating close to the leeward side. Also, the area on the leeward side of the parapet on the windward side of the building experiences a more significant friction velocity than the non-parapet equivalent. With a reduced mean wind speed, this low friction velocity area will increase in size and move closer to the beginning of the roof. Potac et al. (2020) studied snow capture walls which capture snow on the windward side, which reduces. A parapet can be regarded as a snow capture wall. However, the significance of the snow load accumulating on the windward side of the parapet the author has not investigated. As the parapet is only 0.5 meters tall and the upwind fetch length is considerable, it will most likely not lead to a significant snow load being captured.

Additionally, if the wind blows from the other direction ($\theta = 180^\circ$), the friction velocity will increase on that side again, which makes the captured snowdrift susceptible to erosion. Low buildings are more vulnerable to accumulation as the mean wind speed is more considerable. Meanwhile, high buildings are more susceptible to snow erosion. The wind direction is constantly changing in nature, and therefore the snow distribution is continuously changing on the roof.

However, there is a thin area around the building close to edges of the roof next to the parapets where the friction velocity is very low independently of the wind direction. Here snow will accumulate and be trapped. As the height of the parapet increases the size of this aerodynamic shade will increase.

The larger the parapet height, the more flow separation occurs. NP-05x05x01-0° in Table 5.3 has areas on the corner edges where the friction velocity is three times larger than the median friction velocity. The parapets themselves are part of the wall in the boundary conditions. The same extremal values will not be seen. These corner edges will not contribute to snow erosion as no snow will be present there. The parapet and no parapet roofs have an area along with $y = 0$ (middle) with considerably lower values. In the contour plot of the roof with a parapet, this area is further towards the end of the roof compared to the roof without a parapet. This area is also much more prominent for the roof without a parapet. In a separation bubble, the mean speed is significantly

lower than in the surrounding regions.

The friction velocity varies greatly from $\theta = 22.5^\circ$ and $\theta = 45^\circ$, and $\theta = 0^\circ$ as seen in all the plots in Chapter 5. Wind will approach the roof from all directions continuously in reality and the values obtained for $\theta = 22.5^\circ$ and 45° are bundled close to each other. The difference seems to mainly be between $\theta = 0^\circ$ and $\theta \neq 0^\circ$ (and similarly $\theta = 180^\circ$). Therefore the real normalized median friction velocity will be closer to the values obtained for $\theta = 22.5^\circ$ and 45° , than to $\theta = 0^\circ$. u_*/U_H is independent of terrain category. If the engineer only has access to U_{10} then U_H can be approximated if the terrain roughness is known by using a wind profile.

6.2.3 Snow erosion

The design snow load on a roof depends on a wide array of variables as explained in Chapter 3.1. In general, when $u_* > u_{*t}$, the snowbed is susceptible to erosion from wind. There is not only the value of the friction velocity which impacts the total amount of snow eroded from it. The total amount of the snow eroded from a roof depends on the roof area, the duration of the wind when it exceeds $u_* > u_{*t}$, the number of snow days, and winter air temperature. Also, the gusts and bursts can make snow erode even if $u_* < u_{*t}$. If there are few snow days during a season, then the amount of snow erosion will be reduced as there is less snow on the roof, and the snow which is present will be aged (higher u_*t). The amount of snow days increases with lower winter temperatures in a location, as seen in Meløysund et al. (2007). Larger roofs can contain more snow. Longer-lasting wind exceeding the threshold value can transport more snow than short bursts. The total amount of snow eroded from a roof with a parapet is almost similar to a roof with a parapet when observing the median friction velocity. Wind duration cannot be modeled with RANS.

6.2.4 Effect of parameter selection

As in any CFD simulation, boundary conditions have to be selected. They can be a source of application uncertainty, as mentioned in Chapter 3.14.11.

As explained in 3.14.3, there are a wide array of different turbulence models available. RANS was selected as it has been tried and tested in many previous similar studies and is the industry-leading method. It has shown good accuracy for many applications. However, it has demonstrated a significant difference between LES and DNS for some instances. RANS are not able to account for the unsteady effects of wind fluctuations and bursts while LES and DNS is as shown in Brito2020. This is most likely the case since RANS models velocity fluctuations in a more primitive way based on the mean wind speed. However, RANS uses significantly less computational resources than LES

or DNS. 36 CFD simulations were completed, which would increase the computational time drastically with the use of LES or DNS. The goal of this master thesis is to provide a satisfactory solution within the resources available.

As RANS was used, mostly average values were discussed in this thesis. Such turbulent bluff-body flows, characterized by turbulent eddies, will lead to random instances of snow erosion. Local winds bursts can then lead to erosion even if $u_* < u_{*t}$. However, a more complex transient turbulence model like LES or DNS has to be implemented to identify this phenomenon. In nature, friction velocity is time-dependent, and it also depends on how the distribution of the snow changes during erosion. This can be modeled by LES. (Zhou et al., 2018)

Airflow around a bluff body like a cuboid causes transient effects, as mentioned in Chapter 3.14.2. Transient effects complicate the steady-state analysis's ability to conclude a convergent solution. Using a transient analysis method could make it less complicated to achieve convergence.

As the SST turbulence model is independent of the free stream values, the choice of inlet turbulence intensity will not affect the friction velocity results obtained on the roof. The turbulent inlet intensity in the simulations was chosen to be 10% as used in ferreira2019. However, as seen in Figure ?? the normalized friction velocity is relatively unchanged when the inlet turbulence intensity is increased from 5% to 10% for $\theta 0^\circ$. However, for $\theta = 0^\circ$, the normalized friction velocity increases with decreasing turbulent intensity. The choice of turbulent intensity is, therefore, an application uncertainty.

Sand grain equivalent roughness is how ANSYS CFX models roughness on a wall. Furthermore, sand grain equivalent roughness $K_s = D$ where D is the diameter of the snow grains. The diameter of the snow grains varies based on the snow type, from 0.1 - 0.5 mm. As mentioned in Chapter ?? the threshold friction velocity is most strongly correlating to the grain size, and it decreases by increasing grain size. The reason for this is the reduced cohesion between the grains. If K_s increases, then the roughness of the wall z_0 increases. In Figure 5.14 u_* is plotted with $K_s = 0.5\text{mm}$ and $K_s = 0.125\text{mm}$ and compared. Both solution fulfill the requirement of $K_s < y_p$. The choice of K_s is not affecting the solution from wind direction 0° considerably. However, the difference increases between the solutions depending on the choice of K_s as wind direction angle θ increases. Therefore, u_* increases as K_s decreases. On the other hand, CFX's way of implementing wall roughness by a single K_s value assumes that the snowbed will stay uniform during the erosion process, but this is not the case. Therefore the author is unsure if the effect of K_s will be similar to an eroding snowbed.

The turbulence intensity used in similar studies is between five and ten percent. Ten

percent was chosen in this instance as it was used in Ferreira et al. (2019). The flow inside a wind tunnel is less turbulent than the atmospheric boundary layer. The turbulence intensity can be up to 30 percent in boundary layer flow. A turbulence intensity closer to 30 should be chosen in the author's simulations. However, airflow is unpredictable, and the turbulence intensity varies widely. Therefore, is the choice of turbulence intensity an application uncertainty. In Figure 5.15, the mean percentage difference in the friction velocity when simulated with a turbulence intensity of 5 versus 10 percent is circa 8 %.

Different L/H building ratios make minimal difference to the friction velocity normalized by the building height. This is both observed in this thesis and in Qiang et al. (2021) as observed in Figures 5.8, 5.10 and 3.7. A square roof was chosen as it was possible to study most wind directions with only three wind simulations. The width of the building might affect the friction velocity distribution, but it was not studied.

Lastly, the choice of temperature is irrelevant as heat transfer is not modeled in these simulations.

6.3 Consequences of simplifications

In any scientific method which attempts to study a complex natural phenomenon, simplification has to be made to be able to create a model attempting to explain it. There are many variables affecting the solution to varying degrees.

The wind profiles are only valid for an infinite flat surface, with a constant roughness length z_0 and a neutrally stratified atmosphere. As mentioned in Chapter 3.10, the wind is only assumed to have an x-component which is dependent on height and the roughness length. This is a crude oversimplification of complex weather systems. However, close to the ground, the wind profile depends on the terrain's roughness and not the pressure distribution in the air. Additionally, in this master thesis, the building is assumed to be isolated, which often is not the case in real life. In real life, interfering structures and obstacles affect the flow field, which involves the flow variables on top of the roof. Lo et al. (2016) observed that the shear stress on the downstream building was amplified and reduced in different parts of the building.

Atmosphere conditions are regarded as either stable, unstable, or neutral, as mentioned in Chapter 3.6. These conditions will continuously change during the day. Relevant to this thesis is that the wind profile shape and mean wind speed vary based on the conditions. These effects are less significant within 10 meters from the ground. The expression u_*/U_H is independent of the terrain roughness and the gradient of the wind profile. Therefore, the effect of atmosphere stratification is not significant when quantifying u_*/U_H .

The flow is regarded as isothermal and therefore compressible. As $Ma < 0.3$ the flow could be modelled as incompressible and achieve the same results.

Furthermore, the theory behind snow erosion is only occurring if $u_{*t} \leq u_*$ is well studied. Studying snow transport based on single-phase simulations has been previously conducted but is rare compared to double phase simulations. A single-phase simulation is simpler to model and will only provide areas susceptible to snow transport. A single-phase simulation will not model the coupling between the air and snow particles. Therefore as mentioned in Chapter 3.14.1, moment transfer between the air and snow will be neglected. This effect is not significant for low wind speeds. As explained in Chapter 3.2, RANS cannot model moment transfer between snow particles in the air and those in the snow bed, which causes the ejection of snow grains into the air.

6.4 Validity of the master thesis

The relationship friction velocity and the threshold friction velocity has previously been used investigate which areas of a roof is susceptible to erosion and accumulation in Ferreira et al. (2019), Qiang et al. (2019) and Qiang et al. (2021).

A Reynolds dependency check was done to see if the model was valid for larger Reynolds numbers. The mean percentage difference was 7.2 % when comparing with a Reynolds number almost twice as large. The solution is therefore not completely Reynolds independent. The Reynolds number used in the simulations are between 4.2×10^5 to 5.7×10^5 for the 3D simulations at $U_0 = 11.1m/s$. That is similar to the Re in the grid independency study. The Reynolds number where a flow over a rough surface can be characterized as turbulent is well below 10^4 (Lawson, 2001). Therefore the flow around the building is turbulent.

According to Qiang et al. (2021, 2019) $u_*/V_H \approx 0.06$ when $\alpha = 0.12$ m with airflow entering normal to the wall based on the wind tunnel studies and CFD simulations. However, it is not mentioned in the wind tunnel experiments (Qiang et al., 2019) or the CFD simulations (Qiang et al., 2021) if the obtained normalized friction velocity is a mean, median, maximum or minimum value. Therefore, it is difficult to compare the normalized friction velocity expression between this master thesis and those studies. Ntinis et al. (2018) remarks that RANS CFD simulation tends to slightly underestimate velocity and turbulence kinetic energy over a building roof and downstream compared to experimental results. This is supported by the grid independence study and Qiang et al. (2021) where the friction velocity obtained from the CFD simulations is consequently smaller than the friction velocity measured in the wind tunnel experiment. In Qiang2021 the u_* values were gathered from a line constructed in the middle of the

building parallel to the wind direction. This line is drawn in the middle to avoid any edge effects affecting the resulting u_* . Resultingly the sample size is much smaller than those gathered in this thesis. A 2D simulation is an idealization of a 3D simulation. That study was a two-phase simulation; therefore, the solution is expected to be more accurate even though this accuracy increase is not as prominent for lower mean wind speeds.

Downscaling is common in wind tunnel experiments to fit the geometry inside the wind tunnel while still receiving accurate results compared to full scale. Numerous attempts were made to do a full-scale simulation with mean wind speeds that realistically give snow drifting. As mentioned in Chapter 3.2 this is often mean wind speeds exceeding 4.5 m/s. The author could not achieve a converged solution with such large mean wind speeds based on the computational resources available. These simulations were therefore not included in Chapter 5. A full-scale simulation would then have a minimum Reynolds number 41 times larger (with $U_0 = 4.5$ m/s) than the current 1:100 simulations. A 1:100 mesh was selected as the geometry size was similar to the grid independence study. Similarity can be impossible to achieve in a wind tunnel, depending on the case. The 1:100 simulation is a 1:100 geometrically scaled-down in all dimensions. The geometrical similarity is therefore satisfied. Furthermore, the wind profile has the same shape, and the mean wind speed at each point is 1:100 scaled down. The kinematic similarity is then satisfied. Thirdly, the dynamic similarity is more complex to satisfy as all the independent π - groups need to be matched with a full-scale solution. In reality, most independent π -groups are not relevant to the case and do not need to be controlled. This thesis, as it is a single-phase simulation, parameters connected to the snow properties and heat transfer can be neglected. Furthermore, the flow is incompressible, so the Mach number similarity can also be neglected. Therefore only the Reynolds number needs to be matched. If both density and viscosity are the same, the full-scale simulation has to have a mean wind speed at roof height of $U_H = 0.111$ m/s for dynamic similarity to be satisfied. The 1:1 and 1:100 simulations then have a complete similarity. The percentage difference between U_*/V_{10} full-scale simulation and 1:100 scale simulation is circa 2.4 %. However, lawson2001 states that Reynolds numbers does not need to match to achieve complete similarity when the flow is around a building.

Lastly, using a single value for the friction velocity to quantify the friction velocity is simplified. However, it makes the calculations for the engineers more streamlined which is important. As observed in Table 5.4 the friction velocity is clearly not uniform. Saltation is the major transport mode of eroding snow, and in saltation, the snow particles are blown between 0-1 meter vertically. For such a large roof, a large u_* at the beginning will not contribute to saltation away from the roof as the transport length is too large. The snow will then mostly redistribute on the roof. Suspension will occur,

but it contributes less to the total snow eroded. However, large u_* 's at the end of the roof will make it substantially more susceptible to snow erosion as saltation then allows for snow transport away from the roof. Therefore, the distribution of the friction velocities is an important factor that is neglected when representing the whole roof with one friction velocity value. However, as the friction velocity on the roof varies so widely with wind direction and wind is continuously changing direction in real life so the shear stress distribution is not so important to quantify the mass transport from the roof. The local effects of snowdrifts forming close to the parapet will not be captured in a one value friction velocity.

6.5 Modified Z-method

TRANS generally performs worse with modeling flow separation than LES and DNS, and this is a source might for faulty data points in the separated flow. A sharp edge is regarded as an infinite advent pressure gradient, and therefore the separation occurring is extreme. The modified Z-method was used to remove the erroneous datapoints. As the distribution of outliers is challenging to quantify, it will be challenging to deal with them. The Z-method is used as a principle to shed light on the problem with outliers. One of the downsides of such an outlier removal method is that it does not filter based on any physical understanding of the outliers' behavior. However, it will be difficult to integrate physical understanding in the filtration process as the distribution of the outliers are unknown. Therefore the outliers were removed instead of Winsorized.

There exist numerous outline labeling tests and methods, especially for the normal distribution. As mentioned in Chapter 4.2.6, the modified Z-method is a general way of labeling outliers. A similar labeling method can be implemented by the use of box plots. Box plots are often used to visualize the outliers, but it was impractical for so many simulations.

6.6 Limitations

The CFD simulations are limited to a certain extent.

Firstly, a significant number of CFD simulations were completed, and limitations were set on the computational power available. Y^+ in the range of 5-30 is not recommended. Consequently, $y^+ = 40$ was selected after the grid independence study as $y^+ \leq 5$ was not sustainable for the number of simulations. Additionally, that solution was similar to the $y^+ = 7$ presented in Ferreira et al. (2019) which indicates mesh dependency being met. Secondly, experience with CFD before this master thesis was non-existent. The

author's experience was gained with the help of my supervisors, ANSYS literature, CFD forums, and trial and error.

Secondly, the solution was not completely Reynolds independent. It might be completely independent by running the simulations with a larger free stream wind speed which gives a Reynolds number closer to real life conditions. However, computational power was a limited resource.

7. Conclusions

This chapter will conclude the master thesis by summarizing the significant findings concerning the research objectives and research question and their significance and contribution. Finally, it will address the thesis's limitations and suggest areas for further research.

This master thesis aimed to find a relationship between the mean wind speed and friction velocity on a flat roof with or without a parapet. By doing so, the relationship can be implemented into a future more accurate snow model.

The results indicate that the friction velocity on the roof varies substantially depending on the wind direction. In real life the wind direction is continuously changing, and u_* when $\theta = 0^\circ, 180^\circ$ was different to when $\theta = 0^\circ, 180^\circ$. As this wind rarely approaches the building perfectly normal to the wall, it seems that with a continuously changing wind direction, as in nature, u_* will be significantly closer to $\theta = 22.5^\circ, 45^\circ$ than $\theta = 0^\circ$. An expression for the friction velocity u_* normalized by the mean wind speed at the roof's height u_H was quantified to be compare with findings in Qiang et al., 2021. There were some discrepancies between the solutions, but it was unclear how the expression was deduced in Qiang et al. (2019). The expression was found to be between $u_*(\theta = 0^\circ)/U_H = 0.027H$ and $u_*(\theta = 45^\circ)/U_H = 0.062H$ depending on the wind direction θ in Table 5.2. The expression is observed to be independent of the terrain category. However, weather station's normally measure the wind at 10 meters in height, and U_H is often unknown. But if the terrain roughness is known then u_H can be approximated by inserting U_{10} into a wind profile. The results indicate that the friction velocity normalized by the mean wind speed at a 10-meter height U_{10} depends on the wind profile gradient, building height, and wind direction. Furthermore, the wind profile gradient depends on the roughness length z_0 and therefore also α in the power law so $u_* = f(U_{10}, \alpha, H, \theta)$. The equations in Table 5.1 makes it possible to calculate u_* for terrain category 2 and 3 by inserting the building height. The median friction velocity difference between the simulations with or without a parapet was negligible.

Further findings suggest that the choice of sand grain roughness equivalent to K_s has

some effect on u_* . The choice of turbulence intensity also affects the resulting friction velocity. The solutions were not completely Reynolds dependent, with a 7.2 % mean percentage difference compared to a solution with almost twice the Reynolds number. Additionally, a grid independence study was completed to investigate the necessary mesh resolution needed for a satisfactory solution within the limits of computational cost and time available. The chosen mesh was found to be independent of the solution.

Limited research has been completed on investigating friction velocity on a flat roof from varying wind directions with 3D CFD simulations. No similar investigation has been conducted on flat roofs with parapets before. This thesis can be used to shed light on simplifications done in EN-1991-1-3, which in some cases oversimplifies the calculations of the design snow load on the roof.

Future research can be done using LES or DNS instead of RANS to increase the accuracy. Also, conduct two-phase simulations instead of single-phase simulations. Furthermore, develop expressions for normalized friction velocity on other roof shapes. Lastly, to further investigate the impact of parapet size and the effect of other buildings in the vicinity.

References

- Abu-Zidan, Y., Mendis, P., and Gunawardena, T. (Apr. 2021). Optimising the computational domain size in CFD simulations of tall buildings. *Heliyon* 7 (4): e06723. DOI: [10.1016/j.heliyon.2021.e06723](https://doi.org/10.1016/j.heliyon.2021.e06723).
- Aly, A. M. and Bresowar, J. (Mar. 2016). Aerodynamic mitigation of wind-induced uplift forces on low-rise buildings: A comparative study. *Journal of Building Engineering* 5: 267–276. DOI: [10.1016/J.JOBE.2016.01.007](https://doi.org/10.1016/J.JOBE.2016.01.007).
- Ansys CFX Reference Guide* (2021). URL: <http://www.ansys.com>.
- Ansys CFX-Solver Theory Guide* (2021). URL: <http://www.ansys.com>.
- Ansys Meshing User's Guide* (2021). URL: <http://www.ansys.com>.
- Bagnold, R. (Oct. 1974). *The Physics of Blown Sand and Desert Dunes*. Dordrecht, Netherlands: Springer.
- Blocken, B., Stathopoulos, T., and Carmeliet, J. (Jan. 2007). CFD simulation of the atmospheric boundary layer: wall function problems. *Atmospheric Environment* 41 (2): 238–252. DOI: [10.1016/j.atmosenv.2006.08.019](https://doi.org/10.1016/j.atmosenv.2006.08.019).
- Bredberg, J. (2000). *On the Wall Boundary Condition for Turbulence Models*.
- Breuer, M., Jovicic, N., and Mazaev, K. (Feb. 2003). Comparison of DES, RANS and LES for the separated flow around a flat plate at high incidence. *International Journal for Numerical Methods in Fluids* 41 (4): 357–388. DOI: [10.1002/flid.445](https://doi.org/10.1002/flid.445).
- Brito, P. M., Ferreira, A. D., and Sousa, A. C. (Dec. 2021). A CFD study on the Irwin probe flows. *Journal of Wind Engineering and Industrial Aerodynamics* 219: 104808. DOI: [10.1016/J.JWEIA.2021.104808](https://doi.org/10.1016/J.JWEIA.2021.104808).
- Clifton, A., Rüedi, J.-D., and Lehning, M. (Sept. 2006). Snow saltation threshold measurements in a drifting-snow wind tunnel. *Journal of Glaciology* 52 (179): 585–596. DOI: [10.3189/172756506781828430](https://doi.org/10.3189/172756506781828430).
- D., M. G. and D., H. M., eds. (Nov. 2004). *Handbook of snow*. West Caldwell, NJ: Blackburn Press.
- ERCOfTAC Best Practice Guidelines - Industrial computational fluid dynamics of single phase flows* (2000). ERCOfTAC.
- Ferreira, A. D., Thiis, T., Freire, N. A., and Ferreira, A. M. (June 2019). A wind tunnel and numerical study on the surface friction distribution on a flat roof with solar panels. *Environmental Fluid Mechanics* 19 (3): 601–617. DOI: [10.1007/s10652-018-9641-5](https://doi.org/10.1007/s10652-018-9641-5).
- Franke, J. and Baklanov, A. (Mar. 2007). *Best Practice Guideline for the CFD Simulation of Flows in the Urban Environment: COST Action 732 Quality Assurance and Improvement of Microscale Meteorological Models*.
- Ge, Y. and Jin, X. (2004). *Standardization of wind loading for buildings and bridges in China*.

- Gjevik, B. (Nov. 2002). *Viskøse væsker og Elastiske stoffer: Forelesninger i MEK 2200*.
- Gulvanessian, H., Calgaro, J.-A., and Holicky, M. (May 2002). *Designers' guide to EN 1990 Eurocode*. Designer's guides to the Eurocodes. London, England: Thomas Telford.
- Hawkins, D. M. (July 1980). *Identification of Outliers*. en. Chapman & Hall/CRC Monographs on Statistics & Applied Probability. London, England: Chapman and Hall.
- Hetsroni, G., Mosyak, A., Pogrebnyak, E., and Yarín, L. P. (2011). Micro-channels: Reality and myth. *Journal of Fluids Engineering, Transactions of the ASME* 133 (12). DOI: [10.1115/1.4005317](https://doi.org/10.1115/1.4005317).
- Hibbeler, R. (Mar. 2020). *Fluid mechanics in SI units*. 2nd ed. London, England: Pearson Education.
- Holmes, J. (2015). *Wind Loading of Structures, Third Edition*. Taylor & Francis.
- Huang, N. and Zhang, J. (2008). Simulation of snow drift and the effects of snow particles on wind. *Modelling and Simulation in Engineering* 2008. DOI: [10.1155/2008/408075](https://doi.org/10.1155/2008/408075).
- Iglewicz, B. and Hoaglin, D. C. (Dec. 1997). *How to detect and handle outliers: Vol 16*. Milwaukee, WI: ASQC/Quality Press.
- ISO 4355 Bases for design on structures - determination of snow loads on roofs* (2013). International Organization for Standardization.
- Iversen, J. (Sept. 1981). Comparison of wind-tunnel model and full-scale snow fence drifts. *Journal of Wind Engineering and Industrial Aerodynamics* 8 (3): 231–249. DOI: [10.1016/0167-6105\(81\)90023-4](https://doi.org/10.1016/0167-6105(81)90023-4).
- JDoorschot, J. J., Lehning, M., and Vrouwe, A. (Dec. 2004). Field measurements of snow-drift threshold and mass fluxes, and related model simulations. *Boundary-Layer Meteorology* 113 (3): 347–368. DOI: [10.1007/s10546-004-8659-z](https://doi.org/10.1007/s10546-004-8659-z).
- Kaimal, J. C. and Finnigan, J. J. (1994). *Atmospheric Boundary Layer Flows*. Oxford University Press Inc.
- Kikuchi, T. (Nov. 1981). A wind tunnel study of the aerodynamic roughness associated with drifting snow. *Cold Regions Science and Technology* 5 (2): 107–118. DOI: [10.1016/0165-232X\(81\)90045-8](https://doi.org/10.1016/0165-232X(81)90045-8).
- Kind, R. (Jan. 1976). A critical examination of the requirements for model simulation of wind-induced erosion/deposition phenomena such as snow drifting. *Atmospheric Environment (1967)* 10 (3): 219–227. DOI: [10.1016/0004-6981\(76\)90094-9](https://doi.org/10.1016/0004-6981(76)90094-9).
- Lawson, T. (2001). *Building Aerodynamics*. Imperial College Press.
- Liu, Z., Yu, Z., Zhu, F., Chen, X. X., and Zhou, Y. (June 2019). An investigation of snow drifting on flat roofs: Wind tunnel tests and numerical simulations. *Cold Regions Science and Technology* 162: 74–87. DOI: [10.1016/J.COLDREGIONS.2019.03.016](https://doi.org/10.1016/J.COLDREGIONS.2019.03.016).
- Lo, Y. L., Kim, Y. C., and Li, Y. C. (Dec. 2016). Downstream interference effect of high-rise buildings under turbulent boundary layer flow. *Journal of Wind Engineering and Industrial Aerodynamics* 159: 19–35. DOI: [10.1016/J.JWEIA.2016.10.002](https://doi.org/10.1016/J.JWEIA.2016.10.002).
- McLean, D. (Nov. 2012). *Understanding Aerodynamics: Arguing from the Real Physics*. en. Aerospace Series. Nashville, TN: John Wiley & Sons.
- Meløysund, V., Lisø, K. R., Hygen, H. O., Høiseth, K. V., and Leira, B. (Oct. 2007). Effects of wind exposure on roof snow loads. *Building and Environment* 42 (10): 3726–3736. DOI: [10.1016/j.buildenv.2006.09.005](https://doi.org/10.1016/j.buildenv.2006.09.005).
- Menter, F. (July 1993). Zonal Two Equation k-w Turbulence Models For Aerodynamic Flows. In: American Institute of Aeronautics and Astronautics. DOI: [10.2514/6.1993-2906](https://doi.org/10.2514/6.1993-2906).

- NS-EN 1991-1-3. *Eurocode 1: Actions on structures - Part 1-3: General actions - Snow loads* (2018). URL: www.eurokoder.no.
- NS-EN 1991-1-4. *Eurocode 1: Actions on structures - Part 1-4: General actions - Wind actions* (2009). URL: www.standard.no.
- Ntinias, G. K., Shen, X., Wang, Y., and Zhang, G. (Feb. 2018). Evaluation of CFD turbulence models for simulating external airflow around varied building roof with wind tunnel experiment. *Building Simulation* 11 (1): 115–123. DOI: [10.1007/S12273-017-0369-9](https://doi.org/10.1007/S12273-017-0369-9).
- O'Rourke, M., DeGaetano, A., and Tokarczyk, J. D. (Apr. 2005). Analytical Simulation of Snow Drift Loading. *Journal of Structural Engineering* 131 (4): 660–667. DOI: [10.1061/\(ASCE\)0733-9445\(2005\)131:4\(660\)](https://doi.org/10.1061/(ASCE)0733-9445(2005)131:4(660)).
- Oke, T. R., Mills, G. M., Christen, A., and Voogt, J. A. (2017). *Urban Climates*. 1st. Cambridge University Press: 525.
- Owen, P. R. (Oct. 1964). Saltation of uniform grains in air. *Journal of Fluid Mechanics* 20 (2): 225–242. DOI: [10.1017/S0022112064001173](https://doi.org/10.1017/S0022112064001173).
- Peterka, J., Meroney, R., and Kothari, K. (Aug. 1985). Wind flow patterns about buildings. *Journal of Wind Engineering and Industrial Aerodynamics* 21 (1): 21–38. DOI: [10.1016/0167-6105\(85\)90031-5](https://doi.org/10.1016/0167-6105(85)90031-5).
- Pomeroy, J. W. and Gray, D. M. (1990). Saltation of snow. *Water Resources Research* 26 (7): 1583–1594. DOI: [10.1029/WR026I007P01583](https://doi.org/10.1029/WR026I007P01583).
- Potac, J., O'Rourke, M., and Thiis, T. K. (Sept. 2020). Snow Capture Walls. *Journal of Structural Engineering* 146 (9): 06020007. DOI: [10.1061/\(ASCE\)ST.1943-541X.0002763](https://doi.org/10.1061/(ASCE)ST.1943-541X.0002763).
- Qiang, S., Zhou, X., Kosugi, K., and Gu, M. (May 2019). A study of snow drifting on a flat roof during snowfall based on simulations in a cryogenic wind tunnel. *Journal of Wind Engineering and Industrial Aerodynamics* 188: 269–279. DOI: [10.1016/j.jweia.2019.02.022](https://doi.org/10.1016/j.jweia.2019.02.022).
- Qiang, S., Zhou, X., Gu, M., and Kang, L. (Mar. 2021). A novel snow transport model for analytically investigating effects of wind exposure on flat roof snow load due to saltation. *Journal of Wind Engineering and Industrial Aerodynamics* 210. DOI: [10.1016/j.jweia.2020.104505](https://doi.org/10.1016/j.jweia.2020.104505).
- Riktig utforming av parapetbeslag - SINTEF* (2021). URL: <https://www.sintef.no/community/fagblogg/poster/riktig-utforming-av-parapetbeslag/>.
- Sato, T., Kosugi, K., and Sato, A. (Sept. 2004). Development of saltation layer of drifting snow. *Annals of Glaciology* 38: 35–38. DOI: [10.3189/172756404781815211](https://doi.org/10.3189/172756404781815211).
- Schlichting, H. (July 1979). *Boundary Layer Theory*. en. 7th ed. McGraw-Hill series in mechanical engineering. New York, NY: McGraw-Hill.
- Schmidt, R. A. (1980). Threshold Wind-Speeds and Elastic Impact in Snow Transport. *Journal of Glaciology* 26 (94): 453–467. DOI: [10.3189/s0022143000010972](https://doi.org/10.3189/s0022143000010972).
- Spurk, J. H. and Aksel, N. (Jan. 2008). *Fluid Mechanics*. 2nd ed. Berlin, Germany: Springer.
- Saad, T. (2004). *Turbulence Modeling For Beginners*.
- Tabler, R. D. (2003). *Controlling Blowing and Drifting Snow with Snow Fences and Road Design*.
- Tabler, R. D. (1994). *Design guidelines for the control of blowing and drifting snow*. Strategic Highway Research Program, National Research Council: 364.
- Tennekes, H. and Lumley, J. L. (Jan. 1972). *A First Course in Turbulence*. The MIT Press. London, England: MIT Press.

- Thiis, T. and Ferreira, A. D. (2015). Sheltering effect and snow deposition in arrays of vertical pillars. 15: 27–39. DOI: [10.1007/s10652-014-9356-1](https://doi.org/10.1007/s10652-014-9356-1).
- Tominaga, Y., Okaze, T., and Mochida, A. (Apr. 2011). CFD modeling of snowdrift around a building: An overview of models and evaluation of a new approach. *Building and Environment* 46 (4): 899–910. DOI: [10.1016/j.buildenv.2010.10.020](https://doi.org/10.1016/j.buildenv.2010.10.020).
- Tritton, D. (1984). *Physical fluid dynamics*. Van Nostrand Reinhold.
- Troen, I., Petersen, E. L., and Risø, F. (1989). *European wind atlas*. Roskilde, Denmark: Risø National Laboratory.
- Uematsu, T., Nakata, T., Takeuchi, K., Arisawa, Y., and Kaneda, Y. (Nov. 1991). Three-dimensional numerical simulation of snowdrift. *Cold Regions Science and Technology* 20 (1): 65–73. DOI: [10.1016/0165-232X\(91\)90057-N](https://doi.org/10.1016/0165-232X(91)90057-N).
- Understanding impact of $y+$ on flow resolution* (June 4, 2020). URL: https://www.computationalfluidynamics.com.au/y-plus_part3_understanding-impact-of-y-and-number-of-prism-layers-on-flow-resolution/ (visited on 02/03/2022).
- Versteeg, H. K. and Malalasekera, W. (2007). *An Introduction to Computational Fluid Dynamics - The Finite Volume Method*. 2nd Ed. Pearson Prentice Hall.
- Wang, W., Liao, H., Li, M., and Huang, H. (Apr. 2013). Similarity Study on Snowdrift Wind Tunnel Test. *Open Journal of Civil Engineering* 03: 13–17. DOI: [10.4236/ojce.2013.33B003](https://doi.org/10.4236/ojce.2013.33B003).
- Wendt, J. F. and Jr, J. D. A. (2009). *Computational Fluid Dynamics: An Introduction*. 3rd Ed. Springer.
- White, F. M. (Jan. 2015). *Fluid Mechanics*. 8th ed. New York, NY: McGraw-Hill Professional.
- Zhou, X., Kang, L., Gu, M., Qiu, L., and Hu, J. (June 2016). Numerical simulation and wind tunnel test for redistribution of snow on a flat roof. *Journal of Wind Engineering and Industrial Aerodynamics* 153: 92–105. DOI: [10.1016/j.jweia.2016.03.008](https://doi.org/10.1016/j.jweia.2016.03.008).
- Zhou, X., Zu, G., Gu, M., and Hu, J. (July 2018). LES and wind tunnel test on friction velocity on roof surfaces. *Cold Regions Science and Technology* 151: 109–118. DOI: [10.1016/J.COLDREGIONS.2018.03.005](https://doi.org/10.1016/J.COLDREGIONS.2018.03.005).

Appendix A.

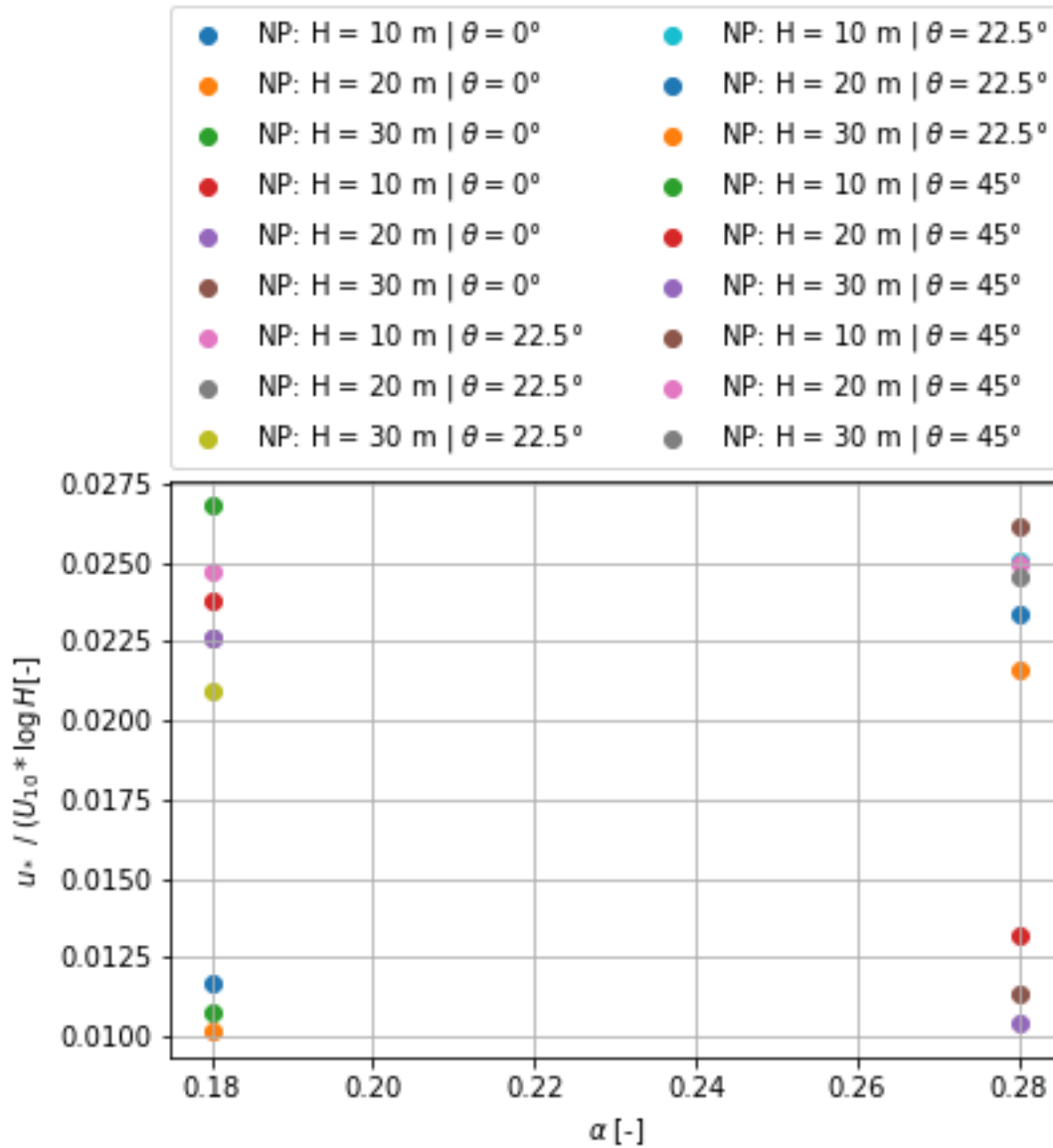


Figure A.1: $\frac{u_*}{u_{10} \times \log(H)}$ versus α without a parapet for different building height and wind directions.

A plot of calculate the friction velocity based on the building height, u_{10} , wind direction and terrain roughness. As seen in the Figure the results vary mostly between $\theta = 0^\circ$ and $\theta 0^\circ$, but also the building height.



Norges miljø- og biovitenskapelige universitet
Noregs miljø- og biovitenskapelige universitet
Norwegian University of Life Sciences

Postboks 5003
NO-1432 Ås
Norway